AD-A253 434

02 JUN 1992

REPORT DOCUMENTATION PAGE

Unclassified
2a. SECURITY CLASSIFICATION AUTHORITY

DTIC SELECTED JUL 27 1992 S B D

2b. DECLASSIFICATION/DOWNGRADING SCHEDULE

4. PERFORMING ORGANIZATION REPORT NUMBER(S)

5. MONITORING ORGANIZATION REPORT NUMBER(S)
AFOSR-TR-

6a. NAME OF PERFORMING ORGANIZATION	6b. OFFICE SYMBOL (If applicable)	7a. NAME OF MONITORING ORGANIZATION
Stevens Institute of Technology		Air Force Office of Scientific Research

6c. ADDRESS (City, State and ZIP Code)	7b. ADDRESS (City, State and ZIP Code)
Department of Physics Hoboken, NJ 07030	Bolling Air Force Base, DC 20332-6448

8a. NAME OF FUNDING/SPONSORING ORGANIZATION	8b. OFFICE SYMBOL (If applicable)	9. PROCUREMENT INSTRUMENT IDENTIFICATION NUMBER
AFOSR	NE	AFOSR - 90-0019

8c. ADDRESS (City, State and ZIP Code)	10. SOURCE OF FUNDING NOS			
	PROGRAM ELEMENT NO.	PROJECT NO.	TASK NO.	WORK UNIT NO.
Bolling Air Force Base, DC 20332-6448	61102F	2301	A7	

11. TITLE (Include Security Classification)
SURFACE PRODUCTION OF IONS

12. PERSONAL AUTHOR(S)
MILOS SEIDL

13a. TYPE OF REPORT	13b. TIME COVERED	14. DATE OF REPORT (Yr., Mo., Day)	15. PAGE COUNT
FINAL TECHNICAL	FROM 10-01-89 TO 04-30-92	1992-05-26	6 + 95

16. SUPPLEMENTARY NOTATION

17.	COSATI CODES		18. SUBJECT TERMS (Continue on reverse if necessary and identify by block number)
FIELD	GROUP	SUB GR	Ion Emission; Ion Sources; Atom, Molecule and Ion Impact

19. ABSTRACT (Continue on reverse if necessary and identify by block number)

Surface production of negative hydrogen ions by electron transfer from solid surfaces to backscattered hydrogen atoms was investigated. The low-energy hydrogen atoms were produced by thermal dissociation or electron impact dissociation of hydrogen gas and by deceleration of a proton beam. A highly stable cesium oxide converter surface, giving the highest observed yield for surface production of H$^-$ ions, was developed. A microwave discharge producing an intense flux of superthermal hydrogen atoms was built and tested. This opens up new approaches to the design of H$^-$ ion sources. Resonant charge transfer in hydrogen atom scattering from surfaces was theoretically studied. Several models of solid state cesium ion guns were developed and used for surface studies.

20. DISTRIBUTION/AVAILABILITY OF ABSTRACT	21. ABSTRACT SECURITY CLASSIFICATION
UNCLASSIFIED/UNLIMITED ☒ SAME AS RPT ☐ DTIC USERS ☐	Unclassified

22a. NAME OF RESPONSIBLE INDIVIDUAL	22b. TELEPHONE NUMBER (Include Area Code)	22c. OFFICE SYMBOL
MILOS SEIDL	(201) 216-5644	NE

DD FORM 1473, 83 APR   EDITION OF 1 JAN 73 IS OBSOLETE

GRANT AFOSR-90-0019

SURFACE PRODUCTION OF IONS

M. SEIDL, PRINCIPAL INVESTIGATOR

FINAL REPORT COVERING THE PERIOD

10-1-89   to   4-30-92

Table of Contents

92-19912

92

1. INTRODUCTION

This is the final report on a two year project entitled "Surface Production of Ions". The work is a continuation of the identically named three year project AFOSR-86-0299 the major contributions of which had been in the area of surface production of negative hydrogen ions and positive cesium ions.

We have discovered that negative hydrogen ions can be produced with high efficiency (> 10%) by backscattering low energy (> 1eV) hydrogen atoms or ions from low work function (1 to 2eV) solid surfaces. The significance of this mechanism for the design of high brightness negative hydrogen sources lies in the fact that low incident energy eliminates sputtering of the converter surface. This makes it possible to use new converter materials. Alkali oxides and alkali earth oxides are particularly attractive because of their low work function and much lower vapor pressure than the vapor pressure of the corresponding metals.

In the area of cesium ion production, our contribution was in the development of cesium ion guns providing ions in the energy range from 20 eV to 5 keV. These guns are based on a novel solid source of cesium ions which was developed previously with the support of the State of New Jersey.

Under the present grant we have continued the search for an "ideal" converter surface which provides efficient surface production of negative hydrogen ions at low energy and is chemically stable in a flux of impinging hydrogen atoms. We have evaluated the performance of several converter surfaces by measuring the yield of negative hydrogen ions produced by backscattering hydrogen atoms from the converter surface. The primary incident hydrogen flux was produced by the following three techniques:
a) Thermal dissociation of hydrogen gas in a tungsten oven (T=0.2 eV),
b) Electron impact dissociation of hydrogen gas in a discharge (T=5eV)
c) Deceleration of a proton beam to low energies (5 to 50eV).

The major contribution of this work has been the demonstration of the feasibility of a new surface source of negative hydrogen ions based on the following concept: superthermal hydrogen atoms, produced in a microwave discharge, are guided on the surface of an external converter, coated with cesium oxide, where they are converted into H$^-$ ions and extracted as a high-brightness beam. It is unfortunate that there is no funding to build such a source.

We have also made progress in the development of cesium ion guns and in application of cesium ion beams. In the course of this work we have published or submitted for publication nine papers listed in Section 7 and attached to this report.

Distribution/	
Availability Codes	
Dist	Avail and/or Special
A-1	

2. STUDIES OF CONVERTER SURFACES

We have studied converter surfaces consisting of thick films of cesium oxides and barium oxides [1,2]. The main diagnostic technique consisted of measuring the yield of negative hydrogen ions produced in backscattering a thermal distribution of hydrogen atoms from the converter surface. The surface electronic structure was studied with photoemission spectroscopy and work function measurements. Information on the chemical composition was obtained by Auger electron spectroscopy, photoelectron spectroscopy and by thermal desorption spectroscopy.

The main result of this work was the **development of a cesium oxide converter with properties approaching the requirements of an "ideal" converter surface.** The main features of the converter are as follows:

a) The converter is produced by in-situ decomposition of cesium carbonate in vacuum or in hydrogen atmosphere and collecting the products of decomposition on a molybdenum substrate.

b) The converter is a mixture of cesium oxide, Cs_2O, and cesium peroxide, $Cs O_2$ deposited in a film typically 1 micron thick on the Mo substrate.2 ,

c) The work function of the converter surface reaches a minimum value of 1.1 eV to 1.4 eV at a temperature of 450 K.

d) The converter has the best H^- yield of any converter surface so far investigated (including cesiated Mo). Scattering of hydrogen atoms with maxwellian distribution of 2670 K (0.23 eV) temperature gives an H^- yield of 1.6 %. This fraction corresponnds to all atoms with incident energy greater than 1.45 eV.

e) The converter is remarkably stable and reproducible. The extracted H^- current remained steady for at least 20 hours of cumulative exposure to atomic hydrogen at a flux of 10^{16} hydrogen atoms/cm^2 sec in the course of 3 days of testing. The converter did not show any deterioration at the end of the three day test run. This stability is presumably due to the stability and low vapor pressure of cesium oxides below 750 K.

3. DISCHARGE SOURCE OF SUPERTHERMAL HYDROGEN ATOMS

In a practically interesting H^- ion source, the cesium oxide converter would have to be exposed typically to a hydrogen flux of 10^{19} hydrogen atoms/cm^2 sec of a temperature larger than 1 eV. Reflection of this atomic flux from the converter surface would produce H^- ions of 1 eV temperature at current density of 0.1 to 1 ampere per cm^2. H^- ions could be extracted from this "external" converter [1] with a high voltage, 10 to 100 kV, so that the brightness of the source could reach 10^4 A/cm^2 str.

In order to demonstrate the feasibility of such an H⁻ source, we have to produce a flux of superthermal hydrogen atoms of sufficient intensity and test the stability of the cesium oxide converter in this flux. Fortunately, dissociation of hydrogen molecules by electron impact produces hydrogen atoms with a minimum energy of 2.3 eV (Franck-Condon process). Consequently one can obtain a flux of fast hydrogen atoms from a hot-electron hydrogen discharge if recombination and cooling by wall collisions is kept small.

We have built a microwave ECR discharge driven by up to 0.5 kW of microwave power at 2.45 GHz [7]. To minimize wall recombination, the discharge is operated in a quartz tube provided with an orifice for effusion of the hydrogen atoms. The converter is located outside the discharge ("external converter" [1]), five centimeters from the orifice. Different converter surfaces have been investigated: pure molybdenum, cesiated molybdenum, and cesium oxide. The flux and energy of the hydrogen atoms was measured by negative suface ionization of the atoms backscattered from the converter. Maximum H⁻ ion current density of 0.5 mA/cm^2 was measured at the cesium oxide coated converter for 420 watts of microwave power. This translates into an H⁻ current density of 200 mA/cm^2 for a converter located on the surface of the quartz tube. The corresponding fast hydrogen atom flux density is about 1 A/cm^2 equivalent. This has been achieved in CW operation in a small plasma (2.5 cm in diameter and 10 cm long) without axial confinement! The measured temperature of the H⁻ ions was in the range of 4 to 5 eV. This work has opened up new concepts for the design of H⁻ ion sources.

4. MEASUREMENTS OF NEGATIVE HYDROGEN ION YIELD

We have completed yield measurements on backscattering of a thermal distribution of hydrogen atoms. The most important contribution of this technique was the development of the cesium oxide converter described in Section 2 and in papers [1,2]. This technique was also used in studies of the barium oxide and cesiated molybdenum converters [1,2].

We have started experiments on backscattering protons and molecular hydrogen ions in the energy range from 2 eV to 50 eV from various converter surfaces [8]. This work is of fundamental importance because yield measurements have never been done in this energy range. These data are also important for the new generation of surface conversion sources.

A new ultra high vacuum chamber was constructed with the partial help of the DURIP Grant AFOSR-89-0195. The chamber is equipped with a home built hydrogen ion beam line, a home built cesium ion gun and an EXTREL quadrupole mass spectrometer purchased with the DURIP funds. The hydrogen ion beam line provides a practically monoenergetic beam of either protons or H_2^+ or H_3^+ ions in the energy range of 2 to 50 eV [8]. This beam is focused onto a converter surface. The scattered negative ions are analyzed with the quadrupole mass spectrometer. The yield of negative ions was measured as function of incident energy for different converter surfaces. An H⁻ yield of 0.15 was measured for 10 eV protons backscattered from a cesiated silicon substrate (to be

4

published). Measurements with othert substrates are in progress.

5. THEORY OF RESONANT CHARGE TRANSFER IN SCATTERING OF HYDROGEN ATOMS FROM A METAL SURFACE

Resonant charge transfer occuring at the reflection of a hydrogen atom from a metal surface has been investigated theoretically with the objective of better understanding production of negative hydrogen ions at low (1 to 10 eV) energies. The approach departs from previous treatments in a few important aspects. No wide band approximation is made; realistic band structures and surface states can be included. No appriori assumption of the separability of the coupling matrix element into a time independent and time dependent part is made. Finally, the coupling matrix elements are explicitly related to the relevant potential of the coupled atom-metal system [6].

6. CESIUM ION BEAMS

We have developed several cesium ion guns [3,9] that had been extensively used in our experimental work with low work function surfaces. The guns are based on a solid state cesium ion source dveloped previously [4].

In the course of the work with cesium oxide surfaces we have found that cesium ion bombardment of a silicon surface in the presence of oxygen gas very significantly enhances the oxidation rate of silicon at room temperature [5]. The enhancement is about ten times larger with cesium than with xenon bombardment due to a catalytic effect of cesium. A couple of follow-up experiments with different gases have indicated that cesium ion beam enhanced chemical vapor deposition could be developed into a new technique for maskless direct write litography. We are looking for a sponsor of this research. The surface analytical chamber in which this work was done is being upgraded with the installation of LEED (Low Energy Electron Diffractometer) and STM (Scanning Tunneling Microscope). Both instruments were acquired with the DURIP Grant funding.

7. LIST OF PAPERS PUBLISHED OR SUBMITTED IN THE REPORTING PERIOD

1. M. Seidl, S.T. Melnychuk, S.W. Lee, and W.E. Carr, Surface production of negative hydrogen ions by reflection of hydrogen atoms from cesium oxide surfaces, Production and neutralization of negative ions and beams, American Institute of Physics Conference Proceedings No. 210, p.30 (edited by Ady Hershcovitch, BNL), New York, NY, 1990.

2. S.T. Melnychuk and M. Seidl, Reflection of hydrogen atoms from alkali and alkaline earth oxide surfaces, J. of Vacuum Sci. Technol. A9, 1650 (1991).

3. A.E. Souzis, W.E. Carr, S.I. Kim, and M. Seidl, Solid state cesium ion guns for suface studies, Rev. Sci. Instrum. **61**, 788 (1990).

4. S.I. Kim and M. Seidl, A new solid state cesium ion source, J. Appl. Phys. **67**, 2704 (1990).

5. A.E. Souzis, H. Huang, W.E. Carr, and M. Seidl, Catalytic oxidation of silicon by cesium ion bombardment, J. Vacuum Sci. Technol. J. Appl. Phys. **69**, 452 (1991).

6. H.L. Cui, Resonant charge transfer in the scattering of hydrogen atoms from a metal surface, J. Vac. Sci. Technol. **A9**, 1823 (1991).

7. B.S. Lee and M. Seidl, Surface production of H⁻ ions by hyperthermal hydrogen atoms, J. Appl. Phys. Lett. (submitted in May 1992).

8. J.D. Isenberg, H.J. Kwon, and M. Seidl, Source of low-energy hydrogen ions for measuring electron transfer in surface scattering experiments, Rev. Sci. Instrum. (submitted in April 1992).

9. S.I. Kim, Y.O. Ahn, and M. Seidl, Solid state cesium ion gun for ion beam sputter deposition, Rev. Sci. Instrum. (sumitted in May 1992).

8. PROFESSIONAL PERSONNEL

Faculty: Milos Seidl, Professor of Physics, Principal Investigator
        Wayne Carr, Professor of Physics
        H. 1. Cui, Assistant Professor of Physics

Postdoctoral Research Associate: Seong In Kim

Graduate Doctoral Students: Andrew Souzis
        Stephan Melnychuk
        Joshua Isenberg
        Brian S. Lee
        Handing Huang   (summer)
        Enrique Samano (summer)
        H.J. Kwon   (summer)

Technician: George Wohlrab

9. DEGREES AWARDED

Andrew E. Souzis, Ph.D. in Physics (May 90)
Thesis: Cesium Ion Bombardment of Silicon.

Stephan T. Melnychuk, Ph.D. in Physics (May 91)
Thesis: Electron transfer in backscattering hydrogen atoms from low-work function surfaces.

SURFACE PRODUCTION OF NEGATIVE HYDROGEN IONS BY REFLECTION OF HYDROGEN ATOMS FROM CESIUM OXIDE SURFACES

M. Seidl, S.T. Melnychuk, S.W. Lee, and W.E. Carr
Department of Physics and Engineering Physics
Stevens Institute of Technology, Hoboken, NJ 07030

ABSTRACT

Negative hydrogen ions are produced by backscattering a thermal distribution of hydrogen atoms from a converter surface coated with a mixture of cesium oxides. The thick film of cesium oxide is produced by thermal decomposition of cesium carbonate and subsequent thermal activation aided by atomic hydrogen. About 60% of atoms with energies greater than 1.5 eV are reflected as negative hydrogen ions for a temperature of 0.22 eV in the thermal distribution. The H^- ions have a Maxwellian parallel energy distribution with a temperature equal to the atomic temperature. Replacing the thermal source of hydrogen atoms with a discharge source results in H^- ions of 1 eV temperature and 100 times lower intensity.

INTRODUCTION

At the last Brookhaven meeting we reported on experiments involving surface production of negative hydrogen ions by simultaneous bombardment of metal targets with cesium and hydrogen ions [1]. In pursuing this work , we noticed that a fraction of the negative hydrogen ion population had a low energy spread of about 0.2 eV. Further experiments have shown that the slow H^- ions were due to backscattering of hydrogen atoms produced by thermal dissociation of hydrogen gas on hot tungsten filaments. In the past three years we have studied production of H^- ions by backscattering the Maxwellian tail of thermally produced hydrogen atoms from several low work function converter surfaces [2-4]. The following conclusions have come out from this work:

a) H^- ions can be produced with high efficiency (> 10%) by backscattering low energy (> 1eV) hydrogen atoms from low work function (< 1.5 eV) surfaces. This has been demonstrated experimentally by scattering hydrogen atoms. However , theory indicates that the same result holds for proton scattering.

b) Low incident energy of hydrogen atoms guarantees low energy spread of the backscattered negative hydrogen ions.

c) An additional bonus of low incident energy is the elimination of physical damage to the converter surface. This has opened up new avenues for the optimization of the converter surface.

Possible applications of low energy surface production in H^- ion sources are schematically shown in Fig.(1). In principle , the converter surface can be placed in two different positions with respect to the hydrogen plasma. The "internal converter", shown in Fig.(1a), is in direct contact with the plasma, the voltage across the plasma sheath being close to the floating potential (a few volts). The converter surface is exposed to a flux of H^+, H_2^+ and H_3^+ ions in addition to hydrogen atoms and excited molecules. All these species contribute to surface production of H^- ions which enter the plasma with low kinetic energy and must be extracted from the plasma.

The "external converter", shown in Fig. (1b), is separated from the plasma (e.g. by means of a magnetic field). Only hydrogen atoms and excited molecules

(1)

contribute to surface production of H⁻ ions which are extracted in a plasma- free region with a high extraction voltage.

Apparently, surface production of H⁻ ions by means of an internal converter has been recently observed in volume sources in which the work function of the converter was reduced by adding cesium [5,6] or barium [7] to the discharge. Low electron temperature in the extraction region of the volume source made the extraction of the H- ions possible.
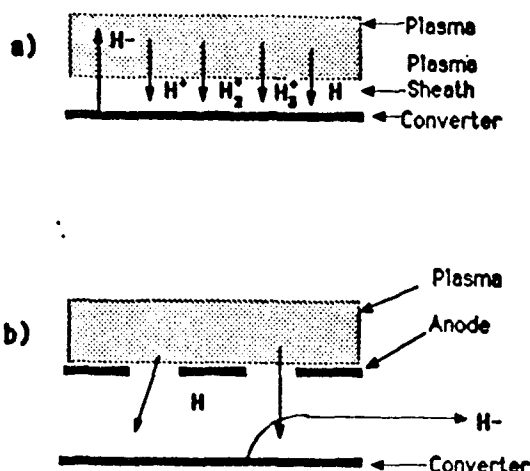

Fig. 1 (a) Internal Converter
(b) External Converter

An H⁻ ion source using an external converter has yet to be built. It critically depends on the availability of a source of hydrogen atoms with a kinetic energy in the 1 to 2 eV range. According to our estimates [4], these atoms will be backscattered as H⁻ ions with a probability better than 50% assuming a converter work function between 1.2 and 1.5 eV. Dissociative electron collisions with hydrogen molecules produce hydrogen atoms with a minimum energy of 2.2 eV. More studies are needed to determine the fraction of atoms reaching the converter without substantial energy loss. Temperature measurements of hydrogen atoms in discharges show that a large fraction of the atoms have an energy higher than 1 eV [8].

Most important for low energy surface production of H- ions is the converter surface. A good converter must have a work function of 1.5 eV or less, it must be chemically stable under exposure to atomic hydrogen and must be easy to use. The first two conditions are met with some single crystal surfaces ,like Si(100) [9], W(110) [10], covered with about half monolayer of cesium. The high vapor pressure of cesium makes this type of converter somewhat inconvenient to use.

The production of surfaces with work functions near or below 1.0 eV have been reported by several groups [10-16]. These surfaces can be divided into two classes. The first represented by Si/Cs/O [12,13] and W/Cs/O [10,11] require atomically clean and structurally perfect surfaces with precise dosing of Cs and O_2 in the submonolayer regime. These surfaces are difficult to produce and maintain and would not be suitable for a negative ion source environment. Recently we have experimented with converters consisting of thick Cs/O and Ba/O layers. The advantage of oxide layers is the fact that their vapor pressures as well as their work functions are lower than the values corresponding to their metals. The Cs/O surface can have a work function as low as 1.1 eV [14-16]. The work function of the Ba/Sr/O cathode is 1.4 eV at 1000° K [17]. In this paper we describe our experiments with cesium oxide converters.

EXPERIMENTAL APPARATUS

The experimental apparatus is shown in Fig.(2). It consists of a planar diode H⁻ surface conversion source, a movable Faraday cup, a rotating magnetic

sector mass spectrometer, two interchangeable atomic hydrogen sources, and a tuneable light source.

The planar diode H⁻ source consists of a cesium oxide converter surface , a tungsten mesh anode, a cover plate with a 1.25 mm exit aperture, and a pair of vertical and horizontal deflector plates. The atomic hydrogen beam impinges on the target through a hole in the front cover plate. The converter is a 0.002" thick Mo ribbon which is coated with a layer of cesium oxide. The Mo ribbon can be ohmically heated and its temperature can be monitored with a thermocouple spotwelded to the ribbon.

Total negative ion and electron currents leaving the exit aperture are detected with the Faraday cup. The electron current is separated from the ion current by imposing a magnetic field perpendicular to the beam by external Helmholtz coils. The magnetic sector is used for checking for impurity ions and for measuring the angular profile of the H⁻ beam.
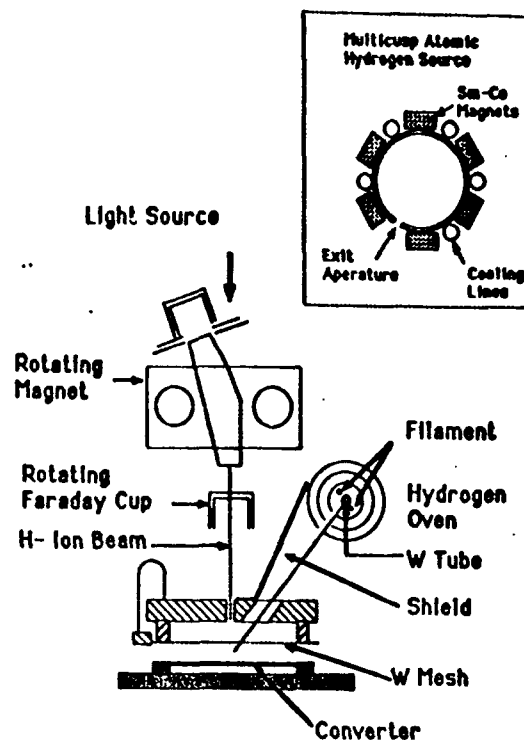

Fig. 2. Experimental Apparatus

PRODUCTION OF ATOMIC HYDROGEN

Two methods for H atom production are used. The first method consists of thermal dissociation of hydrogen gas in a heated tungsten tube similar to that used by Pargellis and Seidl [18], while the second method relies on dissociation of hydrogen gas in a multicusp plasma source similar to that of Leung et. al. [19].

The thermal dissociation source consists of a W tube 3.6 mm O.D., 2.38 mm I.D. and 64 mm long with a 0.7mm hole in the side of the tube. The tube is closed on one end while the other end is Cu brazed into a water cooled SS 304 base through which gas is admitted into the tube. A 20 mm long section is heated by electron bombardment. The tube and filament are enclosed by a water cooled heat shield.

Atomic and molecular hydrogen are assumed to be in thermal equilibrium in the tube. For effusive molecular flow [20] we can write:

$$1/4*CA*[1/2*n_a v_a + n_m v_m] = Q/kT_0 \qquad (1)$$

where n is the number density of atoms or molecules in the tube, v is the mean velocity in the tube, Q is the H_2 gas throughput, T_0 is the H_2 gas temperature in the chamber, A is the area of the exit aperture, and C is the Clausing factor [21]. The molecular and atomic hydrogen pressures in the tube are related by the equilibrium constant for the H_2 dissociation reaction

$$K = P_H/(P_{H2})^{\frac{1}{2}} \tag{2}$$

where K is given in the JANAF tables [22]
Combining equations (1) and (2) and using the ideal gas law $p = nkT$ we can solve for the atomic density

$$n_a = K^2/(2/2kT) \ast \{-1 + (1 + 8Q/CA \ast 1/K^2 \ast (4\pi mkT)^{\frac{1}{2}}/kT_0)^{\frac{1}{2}}\} \tag{3}$$

where T is the tungsten tube temperature. The H effusion flux density impinging on the target is given by

$$\Phi = 1/4 \ast Cn_a v \ast \cos(\alpha) \ast (r/R)^2 \tag{4}$$

where $\alpha = 35.5$ is the angle between the target normal and the exit aperture of the tube, $r = 0.35$ mm is the radius of the exit aperture in the tube, $R = 75.8$ mm is the distance between the converter and the H source, and the Clausing factor C = 0.61. Under typical operating conditions $1 < Q < 50$ sccm, and the tube temperature is in the range $1900° K < T < 2700° K$. At a flow rate of 11 sccm, and $T = 2500° K$ the atomic hydrogen pressure in the tube is 1.4 torr, the chamber pressure is 2.4×10^{-4} torr, and the atomic hydrogen flux density impinging on the target is 8.4×10^{15} cm^{-2}sec^{-1}.

For a thermal dissociation source where the atoms have a Maxwellian distribution only 1% of the beam atoms have energies above 1.5 eV at a temperature of $2600° K$. This illustrates the limitations of this type of source for producing large fluxes of energetic atoms.

The second source of H atoms used in this experiment was a bucket type source using a 0.5 mm tungsten filament, and Sm-Co permanent magnets, see inset in Fig.(2). The source was operated in a constant current mode, and the discharge voltage was changed by varying the pressure and filament temperature. Typical operating parameters were I(discharge) = 2.0 to 3.5 Amps, V(discharge) = 40 to 100 volts and $P(H_2) = 1$ to 50 mtorr. The H energy distribution and density in our source are presently unknown. In the current experiment this source was used for comparison with the thermal dissociation source.

CESIUM OXIDE CONVERTER

Previously three methods have been reported for producing low work function thick Cs/O layers [14]. The first method involves the deposition of Cs on a substrate followed by alternate exposure to Cs and O_2 until a minimum work function is reached. The second method consists of simultaneous exposure to Cs and O_2 with careful control of the pressures. The third method used in this experiment involves the production of Cs/O by thermal decomposition of Cs_2CO_3.

The converter surface is prepared in a way analogous to the conventional way of making BaO thermionic cathodes. A suspension of organic binder and finely ground Cs_2CO_3 powder is brush painted onto the Mo ribbon producing a 0.10 mm thick coating. Since the finely ground powder is unstable in air and absorbs large amounts of water, the entire grinding and coating procedure is carried out in a nitrogen filled enclosure.

The coated converter is initially heated to $720° K$ for approximately 1 hour to evaporate the binder. During the initial heating the temperature is ramped slowly to keep the chamber pressure below 10^{-6} torr.

After degassing, the substrate is heated to 883° K for 50 - 60 sec to convert the Cs_2CO_3 to some mixture of cesium oxides and suboxides presumed to be Cs_2O and Cs_2O_2 [14,15].

Following this procedure the substrate is allowed to cool down to 300° K and H is admitted into the chamber at a flux of approximately 10^{16} $cm^{-2}sec^{-1}$ and an oven temperature of 2500° K. The H^- ion current from the converter as monitored by the mass spectrometer increases by several orders of magnitude after initial exposure to atomic hydrogen. The H^- current saturates in 2500 to 3000 sec. After this initial growth a further increase in the H^- current can be realized by adjusting the substrate temperature to an optimum value of 475° K. An additional increase in the H^- signal can be achieved by repeating the overheating procedure in the presence of atomic hydrogen. The converter is said to be "activated" when the H^- current reaches its maximum steady state value. The activation history of the converter is shown schematically in Fig.(3). The data show that exposure to atomic hydrogen activates the surface.
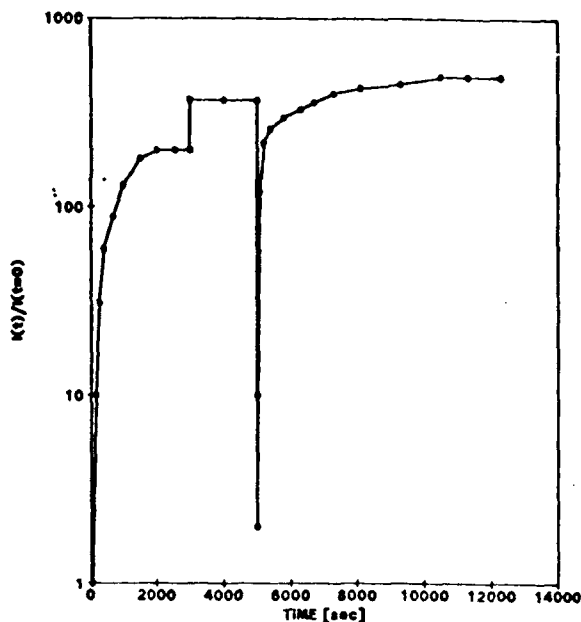

Fig. 3. Converter Activation. 60 to 3000 sec. initial activation by atomic hydrogen, T = 300 K. 3000 to 5000 sec. T = 475 K. 5000 to 13,000 sec., additional activation by heating in atomic hydrogen.

SURFACE PRODUCTION OF H^- IONS

The H^- ion current was measured as a function of the H oven temperature, the extraction voltage, the chamber pressure, and the converter temperature. Yields were calculated by taking the ratio of the negative ion flux at the exit aperture to the incident atomic flux from the H oven. Fig.(4) shows the H^- yields at several chamber pressures and an extraction voltage of 600 volts as a function of $1/T(oven)$. These data were taken at an optimum substrate temperature of 475° K. The effect of changing the substrate temperature will be discussed later. We attribute the variation in yields as a function of pressure to variations in the daily activation of the converter. The data at pressures of 6.24 x 10^{-4}, 2.4 x 10^{-4}, and 2.9 x 10^{-5} torr all show a maximum in the yield curves. The calculated yields depend on the incident atomic flux and on the target properties. Assuming that the ionization probability continues to increase with atomic beam temperature then the apparent drop in the yield would indicate a drop in the H flux on the order of 1.3 times the calculated value. Variations in the H flux may be due to a departure from equilibrium conditions in the tungsten tube. These effects are currently being investigated. No maximum was observed for the data taken at $1.1x10^{-5}$ torr. All of the yield curves exhibit a exp(-C/kT) dependence at temperatures below the turnover point. The highest measured yield was $6.5x10^{-3}$ at an oven temperature of 2593° K and a chamber pressure of $6.2x10^{-4}$ torr. The solid lines in the figure are the calculated fractions of atoms leaving the W tube

(5)

with energies greater than 1.0 eV and 1.5 eV. It can be seen that about 62% of the atoms with energies higher than 1.5 eV are reflected as H- ions at a temperature of 2600° K.

Fig.(5) shows the H⁻ yield at several extraction voltages and a chamber pressure of 6.24 x 10⁻⁴ torr as a function of 1/T(oven). The yields show an increase with extraction voltage due to a Schottky dependence on the extraction field. The usefulness of an atomic reflection type negative ion source is demonstrated here since large extraction fields can be applied which are not possible in conventional H- sputter sources due to excessive sputtering of the extraction electrodes.

The dependence of the H⁻ yield and the ratio of electron to ion current on the converter temperature is shown in Fig.(6). An optimum in the converter temperature is observed where the negative ion yield reaches a maximum and the corresponding ratio of electrons to ions is a minimum. This optimum occurs in the neighborhood of 475° K and is observed at all atomic oven temperatures and pressures. This optimum was stable and reproducible in day to day operation and for several different cesium oxide targets. We attribute the optimum in the substrate temperature to maintenance of a minimum work function surface due to an optimum coverage of Cs and Cs_2O/Cs_2O_2 on the surface.

The dependence of the ratio of electron to ion current on 1/T(oven) for several pressures is shown in Fig.(7). An exponential increase in the ratio is observed for decreasing oven temperature. At high oven temperatures in the range of 2500° K to 2700° K electron to ion ratios on the order of 1 can be achieved.
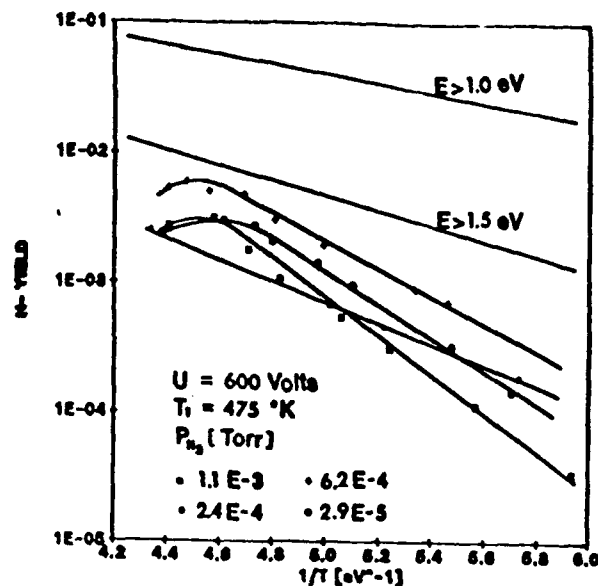

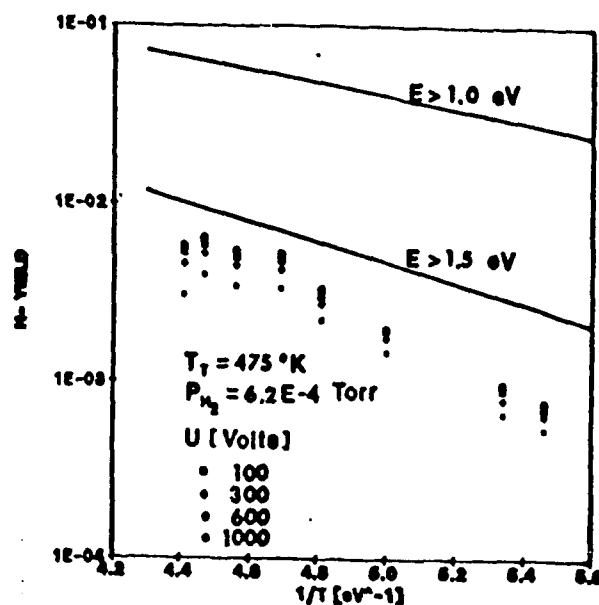Fig. 4. Negative Hydrogen Ion Yield vs. 1/T(oven) at several chamber pressures. Extraction voltage = 600 volts.

Fig. 5. Negative Hydrogen Ion Yield vs. 1/T(oven) at several extraction voltages. Chamber pressure = 6.2E-4 torr.

The increase in the ratio with decreasing oven temperature may be due to trapping and recombination of slow atoms on the surface. The slow atoms are chemisorbed by the image force and recombine on the surface releasing 4.4 eV of energy corresponding to the binding energy of the H_2 molecule. Since this energy is larger than the work function electrons may be emitted from the surface by an "Auger-like" process. This process has not yet been investigated.

Measurements of the H^- angular distributions were done for the activated and non-activated converter surfaces. The angular distributions were converted into parallel energy distribution as described in ref [3].

Fig.(8) shows the H^- parallel energy distribution at an H oven temperature of 2523° K (0.22eV) for activated and non-activated target surfaces. The temperature of the distribution for the nonactivated case is 0.43 eV compared with 0.28 eV for the activated surface. The activation procedure serves not only to increase the H^- yield, but also to remove patch effects [23] due to Cs coverage on the surface. After activation the energy spread was independent of converter temperature variations from 325° K to 550° K. It has previously been shown by Melnychuk et.al.[3] that the parallel energy distribution of H^- ions formed by reflecting thermal energy H atoms from cesiated Mo and n or p type Si (100) surfaces have temperatures equal to the incident atomic temperature. The Cs/O surface has a similar dependence except that patch effects are more pronounced.

Fig. 6. Ratio of electrons to ions and H^- Yield vs. Converter Temperature.

The H^- energy distributions obtained with the tungsten tube source were compared with the distributions from the plasma H source. See Fig.(8). The discharge source was operated under conditions where there were no positive ions extracted from the plasma, therefore all the H^- ions produced on the converter are due solely to reflected hydrogen atoms. The parallel energy distribution indicates the existence of a slow and a fast component. The temperature of the slow component is approximately 0.5 eV and the fast component has a temperature of 1.1 eV. This is a temperature well above that obtainable by thermal dissociation.

The H^- current was optimum at a source pressure of 30 mtorr and increased with the discharge voltage. The maximum H^- currents obtained were approximately 100 times smaller than those obtained with the W tube source at the same chamber pressure. This indicates a low production rate of fast hydrogen atoms in the discharge.
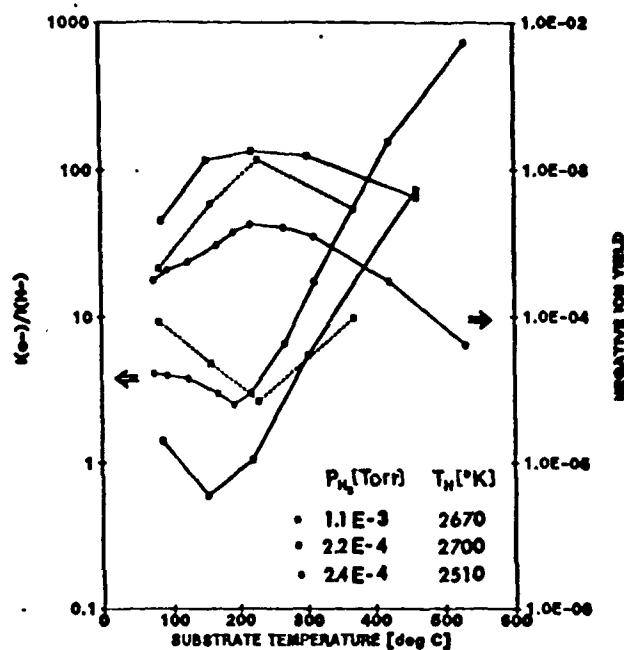
(7)
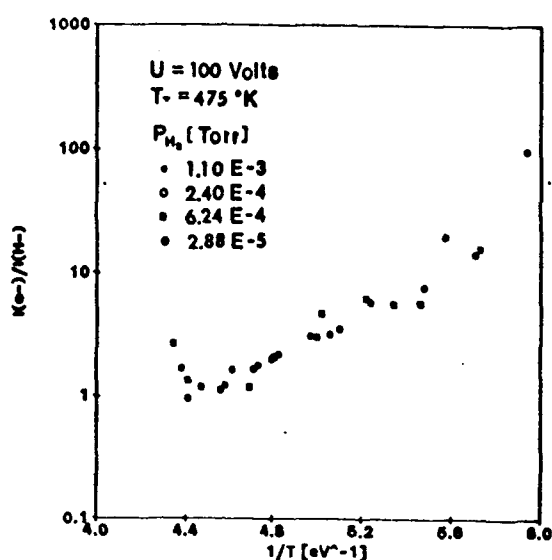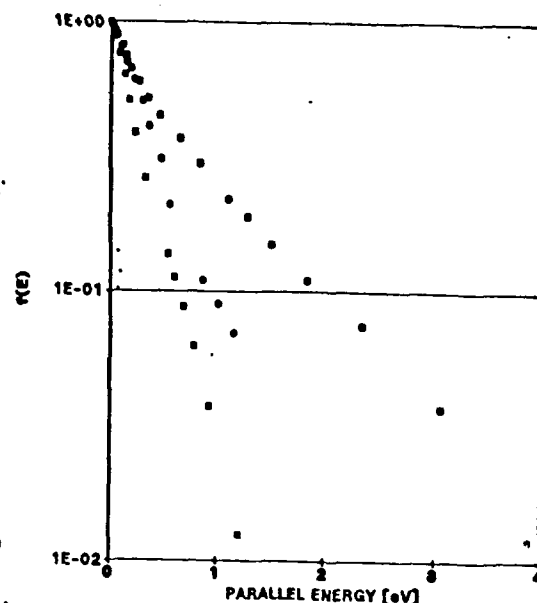
Fig. 7. Ratio of Electrons to Ions vs. 1/T(oven).

Fig. 8. H⁻ Parallel Energy Distribution.
Thermal H atom source: o non-activated
surface T = 0.43 eV, ■ activated surface
T = 0.28 eV. Plasma H atom source: ●
T_{slow}= 0.5 eV, T_{fast}= 1.1 eV.

CONCLUSIONS

Thick films of cesium oxides produced by thermal decomposition of cesium carbonate have been successfully used as converter surfaces for production of negative hydrogen ions by backscattering hydrogen atoms. These surfaces are easy to use, and after activation are stable in a flux of atomic hydrogen of 10^{16} atoms/cm²/sec and of 0.22 eV temperature.

About 60 % of the atoms with an energy higher than 1.5 eV are reflected as H⁻ ions for a temperature of 0.22 eV in the thermal distribution. Under optimum conditions the electron to ion ratio is smaller than one. Large extraction fields can be used since the converter surface is not exposed to ion bombardment.

For a thermal distribution of the incident hydrogen atoms the H⁻ ions have a Maxwellian parallel energy distribution with a temperature nearly equal to the incident atoms (0.22 eV). For a discharge source of atomic hydrogen a fraction of the H⁻ ions have a parallel temperature of 1 eV but an intensity 100 times lower.

ACKNOWLEDGEMENT

(8)

REFERENCES

1. M. Seidl, J.L. Lopes, S.T. Melnychuk, W.E. Carr, and G.S. Tompa, Production and Neutralization of Negative Ions and Beams, edited by J. Alessi (Brookhaven National Laboratory), American Institute of Physics Conference Proceedings No. 158, p.432 (New York,NY, 1987).

2. M.Seidl, W.E. Carr, J.L.Lopes, and S.T. Melnychuk, Proc.3rd European Workshop on Production and Application of Light Negative Ions, FOM Institute for Atomic and Molecular Physics, Amsterdam, February 1988, p 157.

3. S.T. Melnychuk, M.Seidl, W. Carr, J. Isenberg, and J. Lopes, J. Vac. Sci. Tech. A7, 2127 (1989).

4. M.Seidl, W.E.Carr, S.T. Melnychuk, A.E. Souzis, J.Isenberg, and H. Huang, Conference Proceedings, SPIE Vol. 1061, Microwave and Particle Beam Sources and Directed Energy Concepts (1989) p. 547.

5. S.R. Walther, K.N. Leung, and W.B. Kunkel, J. Appl. Phys. 64, 3424 (1988).

6. Y. Okumura, M.Hanada, T. Inoue, H. Kojiman, Y. Matsuda, Y. Ohara, M. Seki, and K. Watanabe, This Symposium.

7. K.N. Leung, S.R. Walther, and W.B. Kunkel, Phys. Rev. Lett. 62, 764 (1989).

8. A.S. Schlachter, A.T. Young, G.C. Stutzin, J.W.Stearns, H.F. Dobele, K.N. Leung, W.B. Kunkel, in ref. 4, p. 610.

9. J.D. Levine, Surf. Sci. 34, 90 (1973).

10. J.L. Desplat and C.A. Papageorgopoulos, Surf.Sci. 92, 97 (1980).

11. J.L. Desplat, Surf.Sci. 34, 588 (1973).

12. R.U. Martinelli, J. Appl. Phys. 45, 1183 (1974).

13. A.E. Souzis, M. Seidl, W.E. Carr, and H. Huang, J. Vac. Sci. Tech. A7, 720 (1989).

14. T.R. Briere and A.H. Sommer, J. Appl. Phys. 48, 3547 (1977).

15. A.H. Sommer, J. Appl. Phys. 51, 1254 (1980).

16. B. Woratschek, W. Sesselmann, J. Kuppers, G. Ertl, and H. Haberland, J. Chem. Phys. 86, 2411 (1987).

17. G. Herrman and S. Wagener, The Oxide Coated Cathode vol. 2 (Chapman & Hall, London, 1951) p. 223.

18. A. Pargellis and M. Seidl, Phys. Rev. B25, 4356 (1982).

19. K.N. Leung, K.W. Ehlers, C.A. Hauck, W.B. Kunkel, and A.F. Lietzke, Rev. Sci. Inst. 59, 453 (1988).

20. E.H. Kennard, Kinetic Theory of Gases (McGraw-Hill, New York 1938) p. 60-64.

21. S. Dushman, Scientific Foundations of Vacuum Technique, Second Edition (John Wiley & Sons, New York, 1962) p. 91.

22. JANAF Thermochemical Tables (Dow Chemical, Midland, MI, 1965) p.91.

23. C. Herring, M.M. Nichols, Rev. Mod. Phys. 21, 185 (1949).

Reflection of hydrogen atoms from alkali and alkaline earth oxide surfaces

S. T. Melnychuk and M. Seidl

Department of Physics and Engineering Physics, Stevens Institute of Technology, Hoboken, New Jersey 07030

Negative hydrogen ions were produced by scattering thermal energy H atoms with a Maxwellian distribution, from converter surfaces consisting of thick coatings of barium oxide, a mixture of cesium oxides and cesium carbonate, cesium oxides produced by decomposition of cesium carbonate, and submonolayer coatings of cesium on polycrystalline Mo. The H ion yields and the ratio of electrons to ions were measured as a function of the incident H atom temperature for each of the converter surfaces. The ion yield and the electron to ion ratio were found to depend strongly on the temperature of the incident H atoms, and on the work function of the surface. The best results were obtained with the cesium oxide converter. H yields from the cesium oxide were above 1% at H atom temperatures above 0.22 eV, and the surface was stable in a flux of atomic hydrogen of 10^{16} atoms/cm^2/s for over 20 h of exposure time with no deterioration in performance.

I. INTRODUCTION

In this paper we present the results of our study of the electron transfer from alkali and alkaline earth oxides to thermal energy H atoms reflected from these surfaces. The most important factor for low energy surface production of H ions is the type of converter surface used. A good surface must have a low work function, it must be chemically stable under exposure to atomic hydrogen, and it must be easy to use. When the incident energy of the hydrogen atom or ion is on the order of a few eV, the restrictions present in most surface conversion sources operating at 100 eV bombarding energy do not apply. Sputtering and implantation are negligible, and complex multicomponent converters such as barium and cesium oxides can be used. The advantage of oxide layers is the fact that their vapor pressures as well as their work functions are lower than the values corresponding to their metals. The benefits of this approach have been recognized in this laboratory some time ago, and research along these lines has been pursued in the past two years.[1-3]

The production of surfaces with work functions around 1.0 eV has been achieved by the coadsorbtion of cesium and oxygen, on a variety of substrates. It is well known that a monolayer of cesium adsorbed on Si(100), or W(110) followed by exposure to oxygen can produce surfaces with work functions of 0.9 eV.[4,5] These Si/Cs/O and W/Cs/O surfaces are extremely sensitive to the substrate surface conditions and require an ultrahigh vacuum environment, and a perfect substrate surface crystal structure. These surfaces would not be suitable for a negative ion source environment. Work functions of 1.0 eV can be achieved by the progressive oxidation of thick Cs films ($\sim$10 atomic layers),[6] while slightly higher work functions, 1.05 to 1.2 eV, have been produced by the deposition of thick films (25 to 50 monolayers) of cesium oxides produced by thermal decomposition of Cs$_2$CO$_3$.[7,8]

We have investigated the production of H ions by backscattering thermal energy hydrogen atoms from thick coatings of BaO produced by the thermal decomposition of BaCO$_3$, and thick coatings of Cs$_2$O/Cs$_2$O$_2$/CsO$_2$ produced by the thermal decomposition of Cs$_2$CO$_3$. These results were compared with H ions produced by atomic backscattering from submonolayer vapor deposited coatings of cesium on molybdenum.

II. EXPERIMENTAL DETAILS

All experiments were performed in a diffusion pumped high vacuum chamber equipped with a liquid nitrogen cryobaffle. The base pressure was 3×10^{-8} Torr. The experimental apparatus is shown in Fig. 1. It consists of a planar diode surface converter, a rotating 28° magnetic sector mass spectrometer, a rotating Faraday cup, a thermal atomic hydrogen source, a cesium oxide or pure cesium evaporation
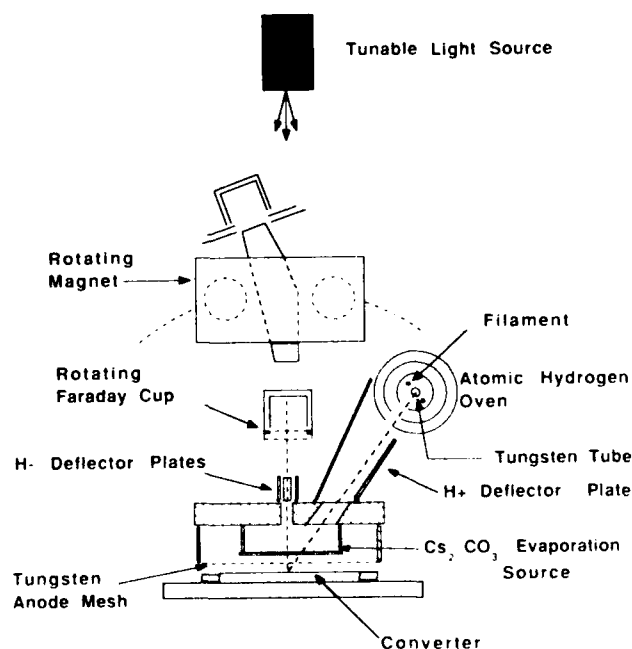

FIG. 1. Experimental apparatus.

source, a residual gas analyzer (RGA) monopole mass spectrometer, and a tunable light source mounted outside the chamber.

The planar diode H⁻ source consists of a Mo ribbon cathode 8.2 mm wide, which was coated by the particular material under investigation, a tungsten mesh anode, and a stainless steel cover plate with a 1.25 mm exit aperture for the extracted H⁻ and e⁻ beams. The cover plate also contained the entrance aperture for the incident H atom beam, and a shield separating the H atom source from the H⁻ analysis region. Vertical and horizontal deflector plates for steering the extracted beam, and a deflector plate for deflecting any positive ions emitted from the atomic hydrogen source, are mounted on the cover plate. The Mo ribbon cathode could be ohmically heated up to 1500 K, and its temperature was monitored with a thermocouple spotwelded to the ribbon.

The atomic hydrogen source consisted of a tungsten tube with a 0.7 mm aperture in the side of the tube. The tube was closed on one end and the open end was brazed into a water cooled base through which H_2 gas was admitted into the tube. The end section of the tube in the vicinity of the exit aperture was heated by electron bombardment from a heated tungsten filament. The total gas flow into the source was measured by a gas flow meter calibrated for H_2 gas. Typical operating temperatures for the source were between 1950 and 2750 K. The flux of hydrogen atoms impinging on the target was calculated based on the assumption of thermal equilibrium in the source, and a knowledge of the conductance of the exit aperture, the tube temperature, and the gas flow into the source.[30] The tube temperature was measured with a disappearing filament type optical pyrometer.

Four types of H⁻ converters were tested. The first two types of converters consisted of $BaCO_3$ or Cs_2CO_3 applied directly onto the Mo cathode ribbon before insertion into the vacuum chamber. Before the Mo ribbon was coated with Cs_2CO_3 or $BaCO_3$ it was cleaned in vacuum by heating to 1350 K for 30 to 60 min in a background pressure of H_2 gas of $8 \cdot 10^{-7}$ Torr. These coated targets were then heated in vacuum to decompose the carbonates to their oxides, and H atoms were reflected from the decomposed targets. The details of the decomposition process will be described in the next section. The third type of converter used consisted of a thick coating of cesium oxides on the Mo substrate ribbon, made in situ, by collecting the evaporation products of Cs_2CO_3 decomposed at 960 K. The cesium oxide evaporation source consisted of a Ni ribbon 7.62 mm wide and 25.4 mm long, onto which was spotwelded a fine tungsten mesh of the same dimensions. The Ni ribbon and mesh were spotwelded onto two stainless steel mounts which served as the electrical contacts. The source plane was oriented at 45° to the converter normal such that some fraction of the evaporated material would be collected by the Mo substrate ribbon. The purpose of the mesh was to increase the surface area of the source to allow a substantial amount of Cs_2CO_3 to be applied onto the surface. The Ni ribbon could be ohmically heated, and its temperature could be monitored with a thermocouple. The last type of converter used was a partially cesiated Mo converter. The Cs_2CO_3 evaporation source was replaced by a Cs dispenser capable of delivering from 10^{13} to

10^{16} Cs atoms/cm²/s to the target. Evolution of gases during the $BaCO_3$ and Cs_2CO_3 decomposition was monitored with the RGA.

Negative ion species and electrons in the extracted beam were identified with the magnetic sector mass spectrometer. The extracted beam consisted of H⁻ ions and e⁻. No impurity ions were detected. The total current leaving the exit aperture was measured by the movable Faraday cup. Electrons were separated from the H⁻ beam by a magnetic field of 20 to 25 G produced by a pair of Helmholtz coils located outside the chamber.

For each of the converter surfaces used, we measured dependence of the H⁻ ion and electron currents, on the incident H atom temperature, and the converter temperature. The H⁻ yield is defined as the ratio of the H⁻ ion current density leaving the converter to the H atom current density incident on the converter. The yield was determined by measuring the H⁻ ion current to the Faraday cup, and calculating the corresponding current density at the exit aperture. Since the exit aperture only samples a small area of the converter surface, and we have a planar extraction geometry, we assume a uniform current density at the exit aperture which is related to the current density at the converter surface by the transmission factor of the anode mesh.

III. EXPERIMENTAL RESULTS

The H⁻ ion yield data, and the ratio of electrons to ions, for each of the converters tested are presented in Figs. 2 and 3. These data are plotted as a function of $1/T$ [eV⁻¹], where T is the temperature of the atomic H oven.

A. Barium oxide converter

The BaO converter was prepared by brush coating the Mo cathode ribbon with a commercially obtained $BaCO_3$ sus-
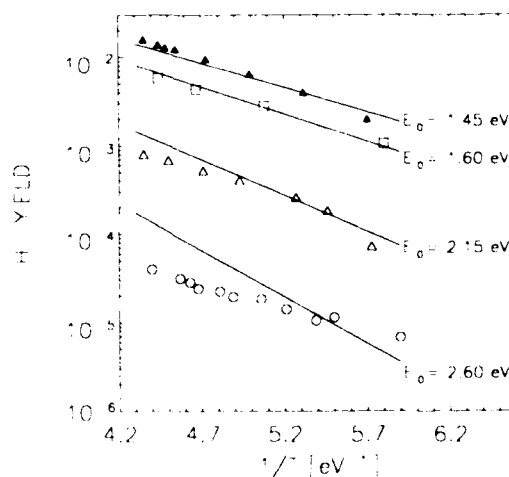

FIG. 2 H⁻ ion yield as a function of the atomic hydrogen oven temperature. BaO, △ Cs_2CO_3, ▲ $Cs_2O \cdot Cs_2O_2$, ○ Cs-Mo converters. The yields from the BaO, $Cs_2O \cdot Cs_2O_2$, and Cs-Mo converters were measured at an extraction voltage of 300 V, and the yield from the Cs_2CO_3 converter was measured at 900 V. The solid lines are the calculated fractions of atoms hitting the target with energy greater than E.
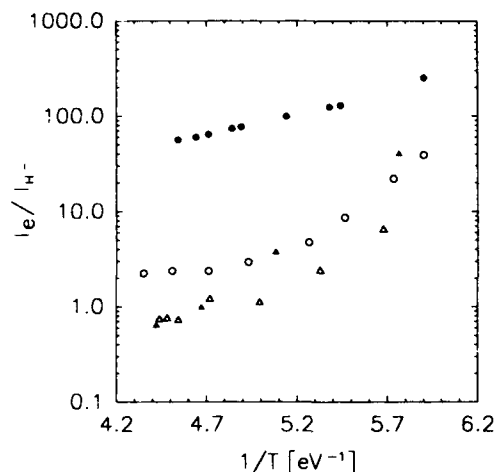
FIG. 3. Ratio of electrons to H ions in the extracted beam. ● BaO, ○ Cs$_2$CO$_3$, △ Cs/Cs$_2$O/Cs$_2$O$_2$, ▲ Cs/Mo converters. The ratios for the BaO, Cs/Cs$_2$O/Cs$_2$O$_2$, and Cs/Mo converters were measured at an extraction voltage of 300 V, the ratio for the Cs$_2$CO$_3$ converter was measured at 900 V.
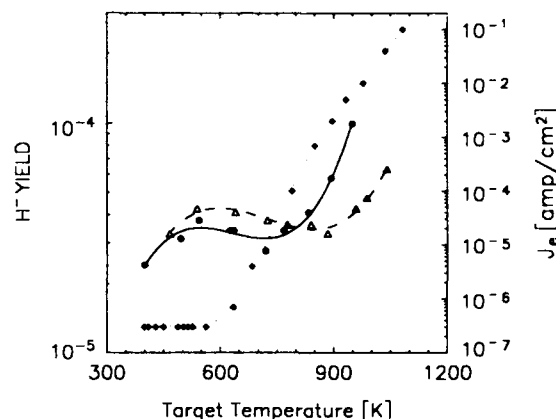

FIG. 4. The dependence of the H ion yield, and the electron current density, on the temperature of the BaO converter at an extraction voltage of 300 V. The H atom flux to the converter was 9.7×10^{15} atoms/cm^2/s at an oven temperature of 2490 K. ◆ J_e; △, ● H ion yield.

pension followed by conversion of the BaCO$_3$ to BaO by heating the coated ribbon in vacuum. Production of a well activated BaO depends on the production of free Ba and on the diffusion of the Ba into the BaO crystals and to the surface of the converter.[10,11] Decomposition of the BaCO$_3$ to BaO was carried out by heating the converter to 1073 K for 2–3 h, followed by a further heating of the converter to 1273 K for approximately 3 min in order to produce free Ba from the BaO, and diffuse it into the BaO coating. Following this activation procedure the converter could function as a stable electron emitter at an operating temperature of 873 K. Further activation of the converter was carried out by repeating the overheating procedure with H$_2$ gas in the chamber, at a pressure of 1×10^{-4} Torr, and with a flux of 1×10^{16} H atoms/cm^2/s impinging on the converter. The overheating procedure in the presence of H$_2$, and atomic H resulted in a sixfold increase in the electron emission current at an operating temperature of 873 K. The converter overheating procedure described above was repeated daily before measuring H yields.

H ion currents, and electron currents were measured at an extraction voltage of 300 V, and a converter temperature of 373 K. The H$_2$ gas flow rate was 26 sccm corresponding to a chamber pressure of 4.1×10^{-4} Torr. The yields ranged from 5×10^{-5} at 2670 K down to 7×10^{-6} at 1960 K. Measurements of the thermionic work function under these conditions gave results ranging from 1.81 to 2.18 eV at a converter temperatures from 628 to 944 K. This may be compared with 2.5 eV which is the work function of clean barium.

The dependence of the H yield and the electron current on the converter temperature is shown in Fig. 4. These data were taken at a constant H oven temperature of 2490 K. At 925 K the yield increases by 3 to 4 times compared with operation at 373 K, however the electron to ion ratio is about 3×10^5. We could not measure H ion currents at tempera-

tures above 925 K due to the large extracted electron current. The increase in the yield at high converter temperatures is most likely due to a lowering of the work function due to diffusion of Ba to the surface of the converter. The dependence of the electron current on the converter temperature shows that at low temperatures the electrons are primarily due to the interaction of atomic hydrogen with the surface, however at high temperatures thermionic emission is the dominant electron production mechanism.
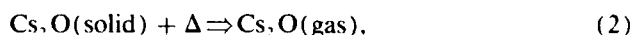
B. Cs$_2$CO$_3$ converter

Preparation of the Cs$_2$CO$_3$ coated converter was carried out in a manner analogous to that used with the BaCO$_3$ coated converter. A suspension of organic binder, and finely ground Cs$_2$CO$_3$ powder was brush painted onto the Mo ribbon producing a 0.1 to 0.2 mm thick coating. Because the finely ground Cs$_2$CO$_3$ powder is extremely moisture sensitive, the entire grinding and coating procedure was carried out in a nitrogen filled enclosure.
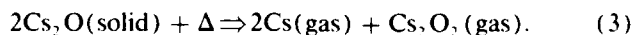
Cs$_2$CO$_3$ decomposes according to the reaction[7,12]

$$Cs_2CO_3 + \Delta \Rightarrow Cs_2O + CO_2, \qquad (1)$$

where Δ is the heat supplied for the reaction to proceed. Below 673 K Cs$_2$O evaporates according to the reaction

$$Cs_2O(\text{solid}) + \Delta \Rightarrow Cs_2O(\text{gas}), \qquad (2)$$

but above 773 K Cs$_2$O reacts to form Cs$_2$O$_2$ according to the reaction[13]

$$2Cs_2O(\text{solid}) + \Delta \Rightarrow 2Cs(\text{gas}) + Cs_2O_2(\text{gas}). \qquad (3)$$

We have attempted to produce a low work function coating directly on the Cs$_2$CO$_3$ converter by appropriate heat treating of the coating, and by exposure to atomic hydrogen. The Cs$_2$CO$_3$ converter was initially heated without H$_2$ gas in the chamber up to a maximum temperature of 879 K. During this heating the gas evolution was monitored with the RGA, and the thermionic electron emission current was monitored with the Faraday cup. Decomposition of the nitrocellulose based organic binder occurred at converter tem-

peratures from 358 to 730 K.[14] As the converter temperature was raised above 763 K a significant increase in the CO_2 peak on the RGA was observed, accompanied by an increase in the electron emission current. At a converter temperature of 879 K the CO_2 peak was 75 times greater than at the base pressure, and the electron emission current increased by 10^3 times when the converter temperature was raised from 707 to 838 K. The evolution of CO_2 gas, and the increase in the electron emission, was indicative of the onset of the Cs_2CO_3 decomposition reaction (1), and a lowering of the work function. The converter was maintained at 879 K for approximately 2 min, after which the converter was cooled to 373 K. After this initial decomposition of the Cs_2CO_3, H_2 gas was admitted into the chamber at a flow rate of 16 sccm, corresponding to a chamber pressure of 3.24×10^{-4} Torr, and the converter was exposed to an H atom flux of 1.2×10^{16} atoms/cm²/s at an oven temperature of 2523 K. At this point the extracted H⁻ ion current was less than 100 pA with the converter at 373 K. The converter was then heated to 843 K for 60 s, in the presence of atomic hydrogen, followed by cooling back down to 373 K. After this second overheating the extracted H⁻ ion current increased to 120 pA corresponding to a yield of 5×10^{-5} H⁻ ions per incident atom. This overheating procedure was repeated 20 more times, until the yield reached a maximum steady state value of 4×10^{-4} ions per atom at a 2523 K oven temperature, and 373 K target temperature. Each heating of the converter was carried out at a 16 to 17 sccm H_2 gas flow rate, and a 2523 H oven temperature, with a flux of 1.2×10^{16} H atoms/cm²/s impinging on the converter surface. Based on reactions (1), (2), and (3), and on ultraviolet photoelectron spectroscopy (UPS) data identifying the presence of O_2^- and O^2- species present on the surface of Cs_2CO_3 targets heated in atomic hydrogen,[15] we assume that the final activated converter surface consisted of a mixture of Cs_2O, Cs_2O_2, CsO_2, and unreacted Cs_2CO_3.

Measurements of the photoelectric threshold of Cs_2CO_3 targets heated in the presence of atomic hydrogen in our vacuum system give values in the range of 1.88 to 1.68 eV depending on the temperature of the converter, and on the degree of activation. Work functions as low as 1.5 eV have been obtained under ultrahigh vacuum (UHV) conditions after several days of heat treating the converter in the presence of atomic hydrogen, however values around 1.7 eV are more typical of this type of target.[15] H⁻ yields from this converter were 20 times greater than from the BaO converter, while the electron to ion ratio was from 5 to 30 times smaller depending on the H oven temperature.

C. Vapor deposited cesium oxide converter

A thick coating of cesium oxides was produced on the converter, in the presence of atomic hydrogen, by heating the Cs_2CO_3 evaporation source above the decomposition temperature of the carbonate, and collecting the products of this decomposition on the Mo substrate ribbon. Briere and Sommer[7] reported obtaining work functions of 1.05 to 1.15 eV from thick films of Cs oxides (25 to 50 monolayers) produced by collection of the thermal decomposition products

of Cs_2CO_3 heated above 873 K. We have measured work functions of thick cesium oxide coatings produced by the above method ranging from 1.45 to 1.2 eV, using the electron retarding technique in a UHV environment.

Before the Mo ribbon was coated it was cleaned by heating to 1000 K for 10 to 15 min, in a background H_2 pressure of 4.0×10^{-4} Torr, with a flux of 9.5×10^{15} H atoms/cm²/s impinging on the ribbon at an oven temperature of 2443 K. The Cs_2CO_3 evaporation source was heated to 963 K approximately 1 min before the heating of the Mo ribbon was shut off in order to allow the source time to degas. No H⁻ ion current was detected with the target at 1000 K, and the source at 963 K. The source was kept at 963 K, while the target was rapidly cooled to approximately 360 K by shutting off the heating current to the Mo ribbon. Material was deposited onto the ribbon for a total of 6 min. Auger electron spectroscopy data[15] of thick films (> 30 A) produced by the decomposition of Cs_2CO_3 under UHV conditions show only Cs and O present on the surface. Based on reactions (1), (2), and (3), and on the data of Klemm and Scharf[13] who have identified Cs and Cs_2O_2 in the condensate of decomposed Cs_2O, we assume that the converter was covered with a mixture of Cs, Cs_2O, and Cs_2O_2.

The converter coating procedure, and the dependence of the H⁻ ion current on the target temperature, are summarized in Fig. 5. As the Mo ribbon cooled after heating to 1000 K, evaporated material from the source was deposited onto it, and a rapid rise in the H⁻ ion current was observed. After approximately 20 s of deposition the H⁻ current peaked at 10 nA, with a target temperature of 425 K, corresponding to a yield of 1.8×10^{-3} H⁻ ions per H atom, followed by a continuous decrease in the ion current for the remainder of the time that the evaporation source was heated. After the deposition source was shut off the H⁻ ion current slowly increased with the converter at 350 K. Upon heating the converter to 445 to 455 K the ion current rose rapidly, and increased for several minutes before reaching a saturation value of 50 nA corresponding to a yield of 9.1×10^{-3} ions per H atom, at an oven temperature of 2443 K.
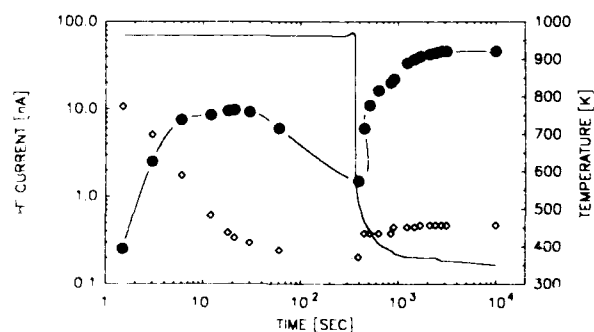

FIG. 5. The time evolution of the H⁻ ion current ● ●, during the Cs_2CO_3 decomposition process. The solid line   (no symbol), shows the temperature of the Cs_2CO_3 decomposition source as a function of time, and the dashed line ⋯ , shows the temperature of the converter as a function of time. The H atom flux to the converter was 9.5×10^{15} atoms/cm² s, at an oven temperature of 2443 K.

The stability of these cesium oxide coatings was studied by measuring the behavior of the H⁻ ion current as a function of time. The extracted H⁻ current remained steady at the optimum converter temperature of 455 K for at least 20 h of cumulative operation over the course of 3 days of testing, during exposure to atomic hydrogen at a flux of 10^{16} atoms/cm²/s. The coated converter survived overnight in a residual vacuum of 3×10^{-8} Torr after it was cooled down to room temperature, and the H_2 gas was pumped out of the chamber. Each day following the initial deposition, in order to achieve the optimum H⁻ yield after the converter sat overnight at room temperature, it was necessary to heat the converter to about 455 K. The growth in the H⁻ ion current with time, showed a sharp increase when the converter was heated above 400 K, followed by a stabilization in the H⁻ current around 450 K.

The dependence of the H⁻ yield on the temperature of the converter is shown in Fig. 6. The optimum converter temperature agrees well with the observed optimum temperature of Briere and Sommer[7] for their 1.2 to 1.05 eV work function surface produced by decomposition of Cs_2CO_3. These data were taken with the H atom source operating at 2443 K, a gas flow rate of 17 sccm corresponding to a chamber pressure of 3.36×10^{-4} Torr, and an H atom flux of 9.5×10^{15} atoms/cm²/s. The yield decreased by 90 times when the converter temperature was raised from 455 to 675 K for approximately 5 min, however upon cooling the converter back to 455 K it recovered to its optimum value after approximately 30 min. The thermal stability of the oxide coatings can be compared with pure Cs. The decomposition temperatures of Cs_2O and Cs_2O_2 are 763 and 863 K,[16] respectively, indicating that these compounds are relatively stable below these temperatures. At 450 K the vapor pressure of pure Cs is 3.52×10^{-3} Torr corresponding to an evaporation rate of 5×10^{15} atoms/cm²/s ($\approx 10^4$ monolayers/s), while at 675 K the vapor pressure is 21 Torr corresponding to an evaporation rate of 2.5×10^{21} atoms/cm²/s ($\approx 10^7$ monolayers/s).[17] Therefore cesiated converters cannot be maintained at elevated temperatures without a constantly resupplying Cs to the surface. When the $Cs/Cs_2O/Cs_2O_2$ converter was kept at 675 K for long periods of time (> 10 min), the yield did not recover fully, suggesting that some components of the coating may have evaporated.

Yields above 10^{-2} can be obtained at H oven temperatures above 2520 K. The highest measured yield was 1.6×10^{-2} at an oven temperature of 2667 K, while the lowest measured yield was 2.0×10^{-3} at an oven temperature of 2035 K. Above 2500 K, the electron to ion ratio is less than 1 and remains fairly constant, while at temperatures below 2470 K the electron to ion ratio increases exponentially up to a value of 6.6 e^-/ion at a temperature of 2045 K.

D. Cesiated molybdenum converter

The final type of converter which was investigated was a partially cesiated polycrystalline Mo converter. The lowest attainable work function for a submonolayer of Cs on polycrystalline Mo is 1.55 eV.[18,19] In this experiment we replaced the Cs_2CO_3 evaporation source with a Cs dispenser.[20] The Cs flux incident on the converter was determined by heating the Mo converter ribbon above the critical temperature for complete ionization of all the incident Cs atoms,[21] and measuring the saturated Cs⁺ ion current density leaving the converter. This saturation value corresponded to the incident Cs neutral flux. Cs fluxes to the converter ranging from 10^{11} to 10^{16} atoms/cm²/s could be obtained.

In order to obtain the optimum H⁻ yields it was necessary to heat clean, and sputter clean the Mo ribbon. The procedure used was similar to that used with the Cs_2CO_3 evaporation source. The Mo ribbon was initially heated to 1360 K for 5 to 10 min in the presence of H_2, and atomic hydrogen, with no Cs vapor incident on the converter. Approximately 2 min before cooling the Mo ribbon, the Cs source was heated up to its operating temperature corresponding to a flux of 10^{15} Cs atoms/cm²/s to the converter. With the Cs source at operating temperature the Mo ribbon was rapidly cooled down by shutting off the heating current, and simultaneously the W anode mesh was heated up to 1200 K to ionize a fraction of the incident Cs neutral flux. As the target cooled it was bombarded with 6 μA/cm² of Cs⁺ ions at 300 V extraction energy for approximately 5 min. During the Cs ion bombardment the H⁻ current grew to a steady state value dictated by the incident H atom temperature, and by the steady state coverage produced on the surface by ion bombardment. After 5 min of ion bombardment the W mesh was cooled down and the converter was coated with Cs vapor. The H⁻ ion current increased to a maximum value corresponding to an optimum Cs coverage, followed by a continuous drop in the current as the converter became over cesiated.

Yields were calculated using the peak value of the H⁻ ion current obtained after sputtering, for several different oven temperatures. The yield ranges from 6×10^{-3} at 2640 K, down to 1×10^{-3} at 2013 K. These yields match very closely with previous measurements of the H⁻ yields from cesiated Mo converters, where a heated tungsten mesh was used as the source of atomic hydrogen. The ratio of ions to electrons varies from 0.65 e^-/ion at 2640 K, up to 41 e^-/ion at
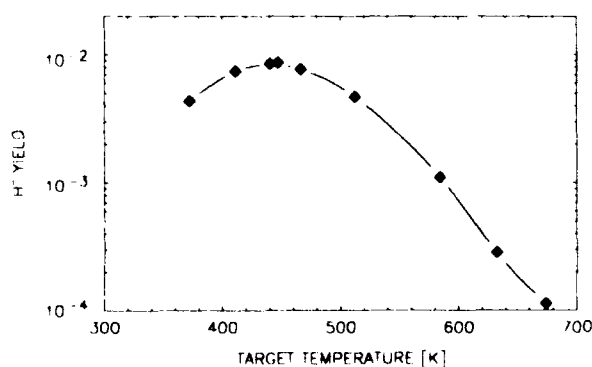

FIG. 6. H⁻ ion yield as a function of the temperature of the $Cs/Cs_2O/Cs_2O_2$ coated converter produced by decomposition of Cs_2CO_3.

2013 K. These values fall in between those for the Cs_2O converter, and the Cs_2CO_3 converter.

IV. DISCUSSION

Theoretical calculations of the ionization probability of H atoms reflected from metal surfaces show a strong dependence of the ionization probability on the velocity of the reflected atoms when the escape energy is close to the binding energy to the surface.[1,22,23] Only atoms with kinetic energies great enough to overcome the potential barrier due to the image force near the surface can escape as negative ions. This leads to a cutoff energy below which the ionization probability rapidly drops to 0. This cutoff energy depends on the difference between the work function and the electron affinity level of hydrogen, and typically lies near 1 eV for surfaces of interest for H⁻ ion production. H⁻ ions which do not have sufficient energy to escape from the surface are trapped and eventually recombine to form H_2 molecules releasing 4.4 eV per molecule at the surface. This recombination energy is sufficient to eject electrons from a surface with a low work function.

Due to the trapping of low energy H atoms, only the atoms in the high energy tail of the incident distribution contribute appreciably to the H⁻ ion current. The observed exponential dependence of the H⁻ yields on $1/T$ is due to the convolution of the relatively constant ionization probability above the cutoff energy with the incident H atom distribution. The fraction of atoms in the incident flux distribution ($\#/cm^2/s$) with energy greater than E_0 is given by the expression

$$f(E > E_0) = \left(1 + \frac{E_0}{kT}\right) \exp(-E_0/kT). \quad (4)$$

Using Eq. (4) we can see that the yields shown in Fig. (2), from the $Cs/Cs_2O/Cs_2O_2$, Cs/Mo, and Cs_2CO_3 targets correspond to $E_0 = 1.45$, 1.6, and 2.15 eV, respectively. Choosing $E_0 = 2.6$ eV for BaO gives an order of magnitude agreement. The values of E_0 correspond to all atoms with energies above E_0 being ionized upon reflection from the target.

The H⁻ ion yields and the electron to ion ratios obtained from the four different converters depended strongly on the temperature of the incident atoms, and on the work function of each converter. At an H oven temperature of 2670 K the H⁻ yield from each of the targets was: $5 \cdot 10^{-5}$ for the BaO converter ($\Phi \approx 2$ eV); $8 \cdot 10^{-4}$ for the Cs_2CO_3 converter ($\Phi \approx 1.7$ eV); $8 \cdot 10^{-3}$ for the Cs/Mo converter ($\Phi \approx 1.55$ eV); and $1.6 \cdot 10^{-2}$ for the $Cs/Cs_2O/Cs_2O_2$ converter ($\Phi \approx 1.2$ to 1.4 eV). The electron to ion ratios at an H oven temperature of 2670 K were: 0.65 e^-/ion for the $Cs/Cs_2O/Cs_2O_2$ and Cs/Mo converters; 2.2 e^-/ion for the Cs_2CO_3 converter; 60 e^-/ion for the BaO converter.

Both the BaO, and the Cs_2CO_3 converters gave substantially lower yields than the $Cs/Cs_2O/Cs_2O_2$ and Cs/Mo converters, and these converters required a complicated activation procedure to obtain the optimum yields. The Cs/Mo converter has the disadvantage that the optimum work function depends strongly on the condition of the Mo substrate, and on the thickness of the Cs coating. This converter also requires a continuous supply of Cs to the surface in order to maintain the desired coverage at typical operating conditions.

The $Cs/Cs_2O/Cs_2O_2$ converter has the lowest work function and the highest yield of all four converters tested. This surface has clear advantages over the BaO, Cs_2CO_3, and Cs/Mo converters. The coating can be several hundred angstroms in thickness, and its work function is independent of the substrate composition. Cesium oxides have a lower vapor pressure than pure Cs making them more stable at elevated temperatures. Additional advantages of the $Cs/Cs_2O/Cs_2O_2$ converter are that it is highly reproducible, stable in a hydrogen environment, and it survives for several days without deterioration in diffusion pumped vacuum system. The stability of these coatings at atomic hydrogen fluxes above 10^{16} atoms/cm^2/s has yet to be determined. The strong dependence of the H⁻ yield on the temperature of the incident atoms suggests that significantly higher yields can be achieved with sources producing hyperthermal H atoms above 1 eV.

[1] M. Seidl, W. E. Carr, S. T. Melnychuk, A. E. Souzis, J. Isenberg, and H. Huang, Conference Proceedings, SPIE Vol. 1061, Microwave and Particle Beam Sources and Directed Energy Concepts, 1989 (unpublished), p. 547.

[2] M. Seidl, S. T. Melnychuk, S. W. Lee, and W. E. Carr Conference Proceedings from the Fifth International Symposium on the Production and Neutralization of Negative Ions and Beams, Brookhaven National Laboratory, Upton, New York, October 29, 1989, to be published in AIP Proceedings.

[3] A. E. Souzis, M. Seidl, W. E. Carr, and H. Huang, J. Vac. Sci. Technol. A 7, 720 (1989).

[4] R. U. Martinelli, J. Appl. Phys. 45, 1183 (1974).

[5] J. L. Desplat and C. A. Papageorgopoulos, Surf. Sci. 92, 97 (1980).

[6] B. Woratschek, W. Sesselmann, J. Kuppers, G. Ertl, and H. Haberland, J. Chem. Phys. 86, 2411 (1987).

[7] T. R. Briere and A. H. Sommer, J. Appl. Phys. 48, 3547 (1977).

[8] A. H. Sommer, J. Appl. Phys. 51, 1254 (1980).

[9] A. Pargellis and M. Seidl, Phys. Rev. B 25, 4356 (1982).

[10] G. Herrman and S. Wagener, The Oxide Coated Cathode vol. 1 (Chapman and Hall, London, 1951) pp. 54–73.

[11] S. Rittner, Philips Res. Rep. 8, 184–253 (1953).

[12] Encyclopedia of Chemical Reactions, edited by C. A. Jacobson (Reinhold, New York 1948), Vol. 2, p. 652, 11–2577.

[13] W. Klemm and H. J. Scharf, Z. Anorg. Allg. Chem. 303, 263 (1960).

[14] H. Kaneko, Y. Yasuoka, K. Gamo, and S. Namba, J. Vac. Sci. Technol. B 7, 1778 (1989).

[15] H. Huang, Stevens Inst. of Tech., Physics Dept., Hoboken NJ. (private communication)

[16] Comprehensive Inorganic Chemistry, edited by J. C. Bailar, H. J. Emeleus, Sir Ronald Nyholm, and A. F. Trotman-Dickenson (Pergamon, Oxford, Eng., 1973), pp. 421, 422.

[17] S. Dushman and J. M. Lafferty, Scientific Foundations of Vacuum Technique, 2nd ed. (Wiley, New York, 1962), pp. 692–700.

[18] T. W. Swanson and R. W. Strayer, J. Chem. Phys. 48, 2421 (1968).

[19] J. R. Hiskes and P. J. Schneider, Proceedings of the Second International Symposium on the Production and Neutralization of Negative Hydrogen Ions and Beams, edited by Th. Sluthers, 1980 (unpublished).

[20] SAES Getters, Milano, Italy.

[21] R. G. Wilson, J. Appl. Phys. 37, 4125 (1966).

[22] S. T. Melnychuk, M. Seidl, W. Carr, J. Isenberg, and J. Lopes, J. Vac. Sci. Techol. A 7, 2127 (1989).

[23] H. L. Cui, J. Vac. Sci. Technol. A 9, 1823 (1991).

Solid state cesium ion guns for surface studies [a)]

A. E. Souzis, W. E. Carr, S. I. Kim, and M. Seidl

Physics and Engineering Physics Department, Stevens Institute of Technology, Hoboken, New Jersey 07030

Three cesium ion guns covering the energy range of 5–5000 V are described. These guns use a novel source of cesium ions that combine the advantages of porous metal ionizers with those of aluminosilicate emitters. Cesium ions are chemically stored in a solid electrolyte pellet and are thermionically emitted from a porous thin film of tungsten at the surface. Cesium supply to the emitting surface is controlled by applying a bias across the pellet. A total charge of 10.0 C can be extracted, corresponding to greater than 2000 h of lifetime with an extraction current of $1.0 \mu A$. This source is compact, stable, and easy to use, and produces a beam with $> 99.5\%$ purity. It requires none of the differential pumping or associated hardware necessary in designs using cesium vapor and porous tungsten ionizers. It has been used in ultrahigh-vacuum (UHV) experiments at pressures of $< 10^{-10}$ Torr with no significant gas load. Three different types of extraction optics are used depending on the energy range desired. For low-energy deposition, a simple space-charge-limited planar diode with a perveance of 1×10^{-7} A/$V^{3/2}$ is used. Current densities of $10.0 \mu A/cm^2$ at the exit aperture for energies $\leqslant 20$ V are typical. This type of source provides an alternative to vapor deposition with the advantage of precise flux calibration by integration of the ion current. For energies from 50 to 500 V and typical beam radii of 0.5 to 0.2 mm, a high perveance Pierce-type ion gun is used. This gun was designed with a perveance of 1×10^{-9} A/$V^{3/2}$ and produces a beam with an effective temperature of 0.35 eV. For the energy range of 0.5 to 5 keV, the Pierce gun is used in conjunction with two Einzel lenses, enabling a large range of imaging ratios to be obtained. Beam radii of 60 to 300 μm are typical for beam currents of 50 nA to $1.0 \mu A$. Results are presented and discussed for UHV studies of ion implantation, electronic surface changes induced by adsorbates, and negative secondary-ion mass spectrometry.

INTRODUCTION

It is well known that the work function of a metal or semiconductor surface is lowered when the surface is covered with a submonolayer deposit of cesium.[1-3] This effect has been used in cold cathode electron sources,[4,5] negative-ion sources,[5] and for enhancing the secondary negative-ion yield of atoms and molecules.[6-10] The presence of cesium greatly enhances the low-temperature oxidation and nitridation kinetics on semiconductor surfaces.[11-13]

Cesium may be deposited on surfaces either by vapor deposition or an ion beam. Vapor deposition sources require shielding, differential pumping, and flux calibration. With an ion source, the incident flux is determined by direct measurement of the target current, and differential pumping may not be necessary. On the other hand, space-charge effects put a lower limit on the incident ion energy. Cs^+ ion sources are typically of the surface ionization type, since the ionization potential of cesium is smaller than the work function of most surfaces. Surface ionization sources also have an inherently low beam temperature.

There are two basic types of Cs^+ surface ionization sources. One is a heated porous tungsten plug that is fed from behind with cesium vapor from a hot liquid-metal oven.[14,15] It has a high current density and low beam temperature, with the disadvantages of differential pumping and problematic routine venting due to pore clogging. A second type typically consists of a thin layer of aluminosilicate de-

posited on a heated tungsten base. Cesium ions are chemically stored in the aluminosilicate and are emitted thermionically.[15] This arrangement is simpler, and no differential pumping is required, but other disadvantages exist. The emitting surface is not unipotential, resulting in large energy spreads, and the amount of cesium stored in the thin layer is small.

We have developed a cesium ion source that combines the advantages of porous metal ionizers and aluminosilicate emitters.[16] Cesium ions are chemically stored in a solid electrolyte pellet whose emitting surface is coated with a porous thin film of tungsten. At an operating temperature of ≈ 1000 °C the solid electrolyte is a good conductor of cesium ions. This makes it possible to control the cesium supply to the emitting surface by a voltage applied across the pellet. Cesium ion emission occurs on the surface of the porous tungsten cathode by surface ionization. This source is clean, compact, efficient, and is compatible with any vacuum system from 10^{-5} to $< 10^{-10}$ Torr.

In this article, we first describe the source in more detail. We then discuss three types of extraction geometries using this source. For energies from 5 to 50 eV a space-charge-limited planar diode geometry is used. In the energy range of 50 to 500 eV, we use a Pierce-type[17] extraction geometry. For the energy range of 0.5 to 5 keV, this Pierce gun is followed by a two-lens optical column. Applications of these guns are also discussed.

I. Cs⁺ SOURCE

The basic element of this source is a cylindrical pellet (0.5 cm in diameter and 1 cm long), sintered from cesium mordenite (Cs-M) powder. The pellet and its emission characteristics are described in detail elsewhere,[18] but the basics are as follows. Cs-M is a solid electrolyte that has an aluminosilicate matrix with an interchangeable cation. When heated, Cs⁺ ions are conducted through its channel structure. The structure has a two-dimensional channel system and its pore size is about 6 Å in diameter. This is known as large-port mordenite.[19]

The Cs-M powder [$Cs_2OAl_2O_3(SiO_2)_{10}$] is obtained from Na-M [$Na_2OAl_2O_3(SiO_2)_{10}$] by ion exchange[20] and then heating to 1050 °C, resulting in a phase transformation from Na-M to Cs-M structure. It is then crushed and ground to a particle size of $\approx 1\,\mu$m, pressed in a cylindrical die, and sintered at 1350 °C for 3 h. The resulting pellet can be machined with a small grinding wheel for use in special applications.

The pellet is heated by an alumina-coated 0.25-mm tungsten filament coiled around the pellet. In order to reduce the power losses, coaxial Ta shields are mounted around the filament. The entire arrangement is placed inside a thin-walled stainless-steel tube with the emitting electrode at one end, and a spring loaded compression assembly at the other. Figure 1 shows this assembly as used with the Pierce electrodes to be discussed later. Around 15–18 W of power are required to achieve an operating temperature of 1000 °C. At this temperature, the Cs-M is an ionic conductor with a conductivity of $\approx 10^{-5}\,(\Omega\,\text{cm})^{-1}$.

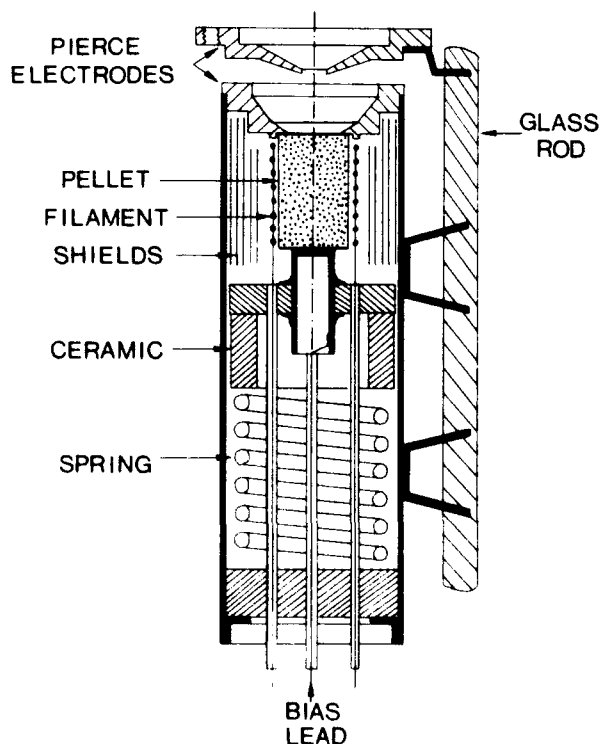The emitting surface of the pellet is sputter coated with a thin porous tungsten layer. This layer improves the energy spread of the beam by providing a unipotential surface for emission and provides a means to supply a flux of ions to the emitting surface. By coating the back of the pellet with a thick layer of platinum, the flux of cesium ions can be controlled by a voltage placed across the pellet. Cesium diffuses through the porous tungsten film to the emitting surface, where it is surface ionized and extracted. A total charge of 10.0 C can be extracted from the source. This corresponds to greater than 2000 h of lifetime at an extraction current of 1 μA.

This source has the same high emission current density properties as the porous tungsten ionizers. In its present form, we have extracted up to 30 mA/cm² in dc steady-state operation. However, it does not need to be differentially pumped, and the thin tungsten film can be vented repeatedly to atmosphere without any pore-clogging problems, which can occur with thicker porous plugs. In addition, the cesium stored in the Cs-M is stable upon repeated exposure to atmosphere and can be handled without any special precautions or dangers, unlike the liquid-metal-based sources.

The time needed to degas the source is ≈ 1 day at a pellet temperature ≈ 1100 °C. Once outgassed, there is no discernible gas load at a pressure of $< 10^{-10}$ Torr, and the source may be operated without changing the system pressure. After the initial break-in period, the source is normally kept hot (≈ 500 °C), eliminating start-up outgassing, and preventing adsorption of contaminants on the gun assembly. It has been reported that zeolite sources are gassy and easily contaminated by active gases,[4] but we have not found this to be a problem with our arrangement.

The beam produced by an early version of this source contained $< 0.40\%$ Rb⁺, $< 0.05\%$ K⁺, and $< 0.02\%$ Na⁺. The relatively high percentage of Rb⁺ was due to Rb impurity in the CsCl (99% pure) used in the ion-exchange process. This form of contamination has been seen before[21] and is greatly reduced by using higher-purity CsCl (99.9%).

II. EXTRACTION GEOMETRIES AND RESULTS

A. Planar diode

For deposition energies from 5 to 50 eV, a planar diode extraction geometry is used. The source is assembled as shown in Fig. 1, with the substitution of planar electrodes for the Pierce electrodes. The emitting end of the pellet is machined with a small step, such that the emitting surface is flush with the exterior of the electrode surface. The extraction electrode is spaced 0.75 mm from the pellet surface and has a tungsten mesh spot welded over the extraction aperture in order to provide a uniform field. The theoretical perveance of this planar diode arrangement is 1×10^{-7} A/V$^{3/2}$. Target currents $\approx 1\,\mu$A at energies < 20 V are typical. This gun has been used in studies of electronic surface changes induced in silicon by cesium deposition,[22] where it is seen to be fully equivalent to a vapor deposition source, with the advantage of precise calibration of the flux by integration of the ion current and other advantages described previously. Results of this study include the attainment of a work func-

FIG. 1. Cesium ion source assembly drawing, shown with the Pierce electrodes as an example.

Labels in figure: PIERCE ELECTRODES, GLASS ROD, PELLET, FILAMENT, SHIELDS, CERAMIC, SPRING, BIAS LEAD

tion equal to 0.9 eV by Cs⁺ bombardment and oxygen coad-sorption and experimental support for an asymmetric dimer model for the sputter-cleaned and annealed Si(100) target.

B. Pierce gun

For energies from 50 to 500 V, a Pierce-type[17,23] extraction system of our own design is used, as shown in Fig. 1. It consists essentially of three conical sections: two for the focus electrode and one for the extraction electrode. The analytic solution for the field in a spherically convergent ion gun has been worked out in detail.[24] It gives a complete representation of the potential distribution at the beam edge with the perveance, convergence angle, and radius of curvature of the cathode as parameters. The perveance (P) is defined from the Child-Langmuir equation for space-charge-limited flow in a diode,

$$I = PV^{3/2},\qquad(1)$$

and is determined for a given setup only by geometric factors. The design values were as follows: a perveance of 1.0×10^{-9} A/V$^{3/2}$, a convergence angle of 11.8°, and a cathode radius of 9.76 mm.

A computer program written in house is used to determine the potential distribution at the beam boundary for a given electrode configuration. This calculation is subject to the boundary condition that the gradient of the potential at the beam edge be parallel to that edge, and to boundary conditions at the electrode surfaces. The program uses a triangular grid, which allows the density of grid points to be adjusted to give greater accuracy in the regions of higher field. This method gives good accuracy without requiring excessive computation time. The angles of the electrodes are varied until the error between the computed beam-edge potentials and the analytic values is less than 1%. These computer calculations indicate that a deviation in the angle of the electrode surface in contact with the emitter of as little as 1° results in an average error close to the emitter of 4.5%.

The emitting surface of the pellet is placed in electrical contact with the beam-forming electrode of the Pierce gun as shown in Fig. 1. The aperture in the extraction electrode is covered with an 84% transmitting W mesh to remove aberration and divergent lens effects.[23] The electrodes are assembled on a mounting jig and are then secured and insulated by glass rods. The rods are mounted by heating them until they are soft and inserting the electrode supports into them. The machining accuracy of the focus electrode is critical to obtain an acceptable beam. We have seen experimentally that an electrode with a 7° error results in a source that is drastically different and in complete disagreement with the intended design. The electrodes used in this gun have an angular error of ~0.5°.

In Fig. 2, the I-V characteristics are shown for several temperatures. A perveance of 1.2×10^{-9} A/V$^{3/2}$ is experimentally determined from the slope of these lines. The lowest-temperature data illustrates the effect of sample bias. For zero bias, the current increases as $V^{3/2}$, as it should for space-charge-limited emission. However, at ≈100 V the rate of increase begins to drop, indicating that the current is becoming emission limited. With the proper bias voltage placed
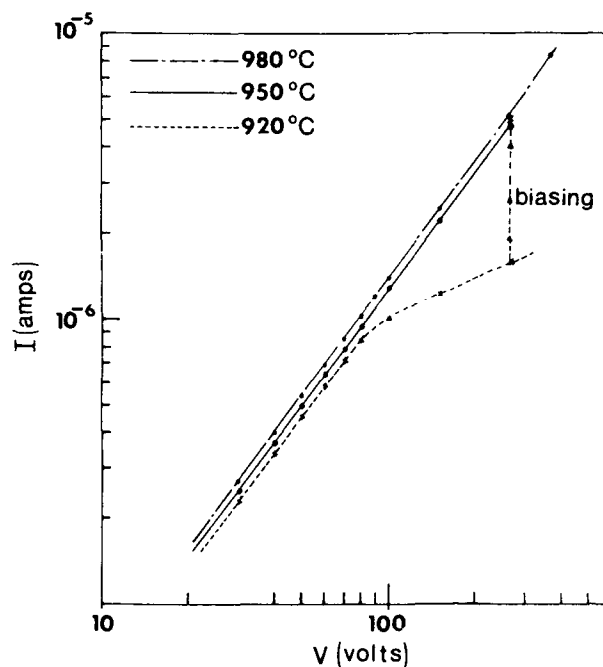
across the pellet, the emission increases to its space-charge-limited value.

The theoretical value for the position of minimum beam radius, taking only space charge into account,[23] is 10.9 mm from the cathode surface. The actual focal point varies slightly, from 10.5 mm at 100 V to 11.5 mm at 500 V. The beam radius at the focal point is measured by passing a Faraday cup with two slits a known distance apart, across the beam. The beam radius is then determined by measuring the peak half width at half maximum and calibrating using the known slit distance. In Fig. 3 are plotted experimental data, showing the beam radius at the focal point versus beam energy. The solid line represents the equation

$$R = f(T/\pi U)^{1/2} + \Delta,\qquad(2)$$

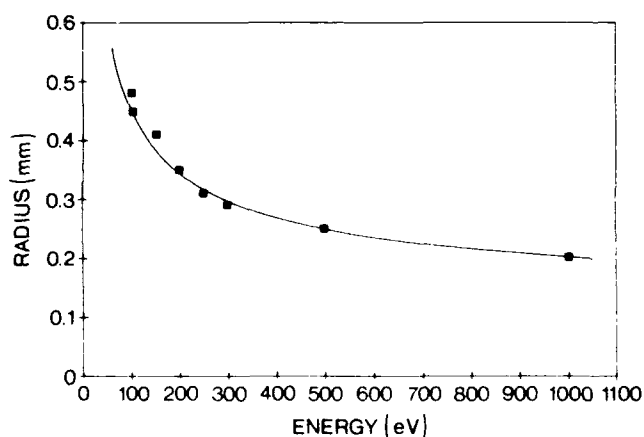where R is the beam radius at the focal point, f is the focal

FIG. 3. Pierce gun beam radius at the focal point vs beam energy. The squares are experimental data, and the curve represents Eq. (2) in the text for an effective beam temperature of 0.35 eV.

distance, T is the effective beam temperature in eV, U is the beam energy, and Δ is the spread due to space charge. The only variable parameter in this equation is the effective beam temperature. All the other values are known. This equation is arrived at by assuming that the beam starts off with a Maxwellian distribution of initial transverse velocities. The value for the spread due to space charge can be calculated[23] and is found to be $\Delta = 0.086$ mm. Using T as a fitting parameter we obtain the curve shown in Fig. 3 for an effective beam temperature of 0.35 eV. This is to be compared to the actual temperature of 0.11 eV. The fact that this effective spread is greater than the true thermal spread can be attributed to deviations from true Pierce geometry caused by a combination of design ($< 1\%$) and machining ($< 0.5°$) errors.

This gun has been used in studies of composite thin-film production by ion bombardment.[25] Results show the relationship between steady-state surface concentration of Cs, incident energy, and substrate mass.

C. High-energy gun

For energies from 0.5 to 5 keV, the Pierce gun described in Sec. IIB is mated to an optical column consisting of two Einzel lenses of the three-tube type. This column is depicted schematically in Fig. 4. It consists of an initial aperture that is mounted at the Pierce gun focal point. This aperture is then imaged by a condenser lens to a point inside a drift tube, at the end of which is a beam-limiting aperture. The ions that pass this aperture are then focused to the sample by an objective lens and rastered by deflector plates mounted after the lens. Basic optics yields the imaging ratio[26] (see Fig. 4):

$$\frac{d_2}{d_0} = \frac{b_1}{a_1} \frac{b_2}{a_2} = \frac{b_2}{a_1/(c/b_1 - 1)}. \tag{3}$$

By changing the strength of the condenser lens, the focal point b_1 inside the drift tube is changed. If this focal point is
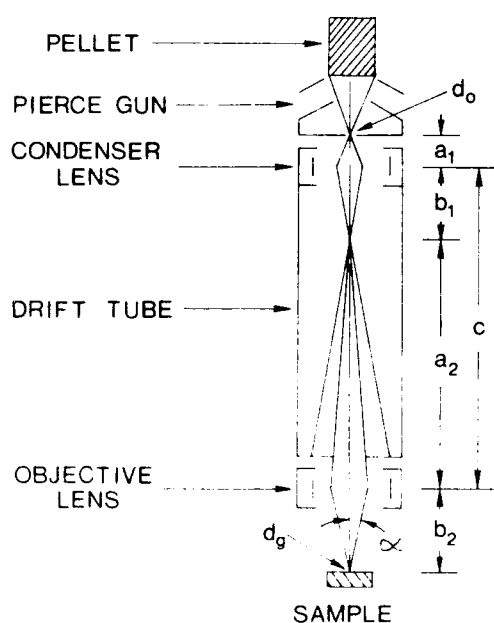
close to the aperture at the end of the tube, a large beam diameter and high beam current result. If the focal point is close to the condenser lens, a small beam diameter with low beam current is obtained. By this method, a wide range of imaging ratios is covered.

An approximate relation for the beam radius as a function of beam current is derived,[26]

$$R = \frac{1}{2}[(4I/\beta)(\pi\alpha)^{-2} + (C_s^2\alpha^3)/4]^{1/2}, \tag{4}$$

where α is the convergence half angle and β is the beam brightness, defined in A cm^{-2} sr^{-1}. C_s is the spherical aberration coefficient. Because of the intrinsically low energy spread of the source, we can ignore chromatic aberrations. If we know the optical properties of the lens column, we can then determine the brightness. In Fig. 5, experimentally determined values for beam radius versus beam current are shown for a beam energy of 2.5 keV. The solid line is a plot of Eq. (3) using the estimated values[27] $\alpha = 1.17 \cdot 10^{-3}$ rad and $C_s = 100$ cm and using β as a fitting parameter. The brightness value for a best fit is found to be $\beta = 1.0$ A/cm^2 sr. We are currently developing a microprobe ion gun using a version of this same source that will have an estimated brightness an order of magnitude larger.

This gun has been used for implantation studies, and for negative secondary-ion mass spectrometry (SIMS). Implantation studies were undertaken to provide evidence for a simple model developed for formation of composite thin films by ion bombardment.[25] Calculated concentration profiles were found to match qualitatively the experimental SIMS depth profiles. Negative SIMS studies indicate that using cesium as a primary bombarding ion enhances the yield of atoms and molecules with high electron affinity.[9,10] In Fig. 6, the ratio of ^{29}Si yield due to Cs$^+$ ion bombardment to the yield due to xenon bombardment is shown as a function of Cs$^+$ dosage. Xenon is used because its mass is essentially the same as that of cesium; thus only the electrochemical differences will affect the results. The data show a gradual increase as a function of dose, which is attributed to formation of a thin layer of cesium, as described in a previous paper.[25] At steady state, the yield levels off at a value 50 times greater than that due to xenon bombardment.
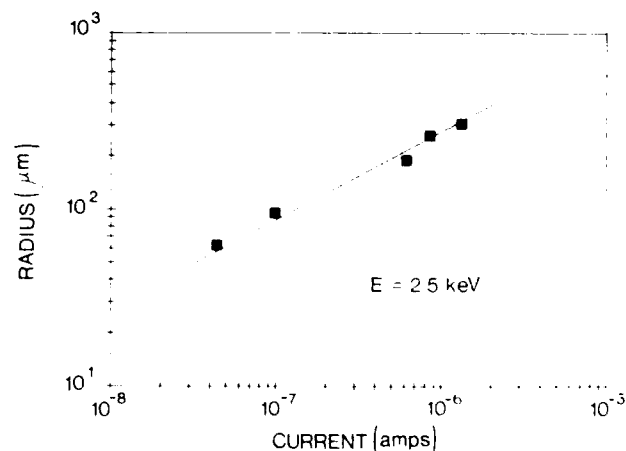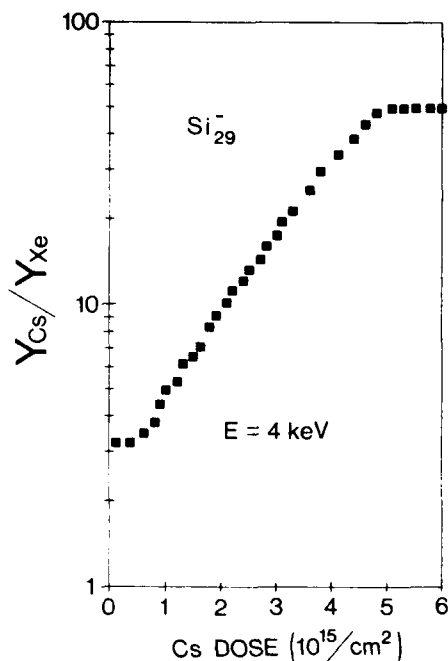
FIG. 6. Ratio of the SIMS yield of negative ^{29}Si under cesium ion bombardment to the yield under xenon bombardment as a function of cesium ion dose. Bombarding energies were both 4 keV.

III. SUMMARY

We have developed a solid-state cesium ion source that can be used in a variety of extraction geometries. It is clean, compact, and is compatible with a wide range of system pressures.

Applications described in this paper are low-energy bombardment as an alternative to vapor deposition, studies of low- and high-energy bombardment and implantation, and negative SIMS. Studies of low-temperature oxidation and nitridation promoted by cesium deposition are in progress.

ACKNOWLEDGMENTS

a) The abstract of this paper appears in Proceedings of the Ion Source Conference [Rev. Sci. Instrum. **61**, 658 (1990)].

[1] D. L. Ferhs and R. E. Stickney, Surf. Sci. **8**, 267 (1967).
[2] L. W. Swanson and R. W. Strayer, J. Chem. Phys. **48**, 2421 (1968).
[3] C. A. Papageorgopoulos and J. M. Chen, Surf. Sci. **39**, 283 (1973).
[4] H. Yasunaga, Rev. Sci. Instrum. **47**, 726 (1976).
[5] R. E. Weber and W. T. Peria, Surf. Sci. **14**, 13 (1969).
[6] R. U. Martinelli, J. Appl. Phys. **45**, 1183 (1974).
[7] A. H. Sommer, J. Appl. Phys. **51**, 1254 (1980).
[8] J. L. Lopes, J. A. Greer, and M. Seidl, J. Appl. Phys. **60**, 17 (1986).
[9] M. Seidel, A. E. Souzis, W. E. Carr, and G. S. Tompa, 37th Pittsburgh Conference and Exposition, March, 1986, Book of Abstracts, No. 743.
[10] H. A. Storms, K. F. Brown, and J. D. Stein, Anal. Chem. **49**, 2023 (1977).
[11] A. Franciosi et al., Phys. Rev. B **35**, 910 (1987).
[12] P. Soukiassian et al., J. Vac. Sci. Technol. A **6**, 1535 (1988).
[13] D. G. Welkie, Secondary Ion Mass Spectrometry SIMS V, edited by A. Benninghoven et al. (Springer-Verlag, New York, 1986), p. 146.
[14] G. R. Brewer, Ion Propulsion (Gordon and Breach, New York, 1970), Chap. 4.
[15] O. Heinz and R. T. Reaves, Rev. Sci. Instrum. **39**, 1230 (1968).
[16] M. Seidl, U. S. Patent No. 4 783 595 (8 November 1988).
[17] J. R. Pierce, Theory and Design of Electron Beams (Van Nostrand, Princeton, NJ, 1954), pp. 173–193 and Chap. 10.
[18] S. I. Kim and M. Seidl, J. Appl. Phys. (to be published).
[19] J. Ito, Am. Mineralogist **61**, 170 (1976).
[20] Donald W. Breck, Zeolite Molecular Sieves (Wiley, New York, 1974), Chap. 7.
[21] R. E. Weber and L. F. Cordes, Rev. Sci. Instrum. **37**, 112 (1965).
[22] A. E. Souzis, M. Seidl, W. E. Carr, and H. Huang, J. Vac. Sci. Technol. A **7**, 720 (1989).
[23] R. G. Wilson and G. R. Brewer, Ion Beams With Applications to Ion Implantation (Wiley, New York, 1973), Chap. 3.
[24] I. Langmuir and D. Blodgett, Phys. Rev. **24**, 49 (1924).
[25] W. Carr, M. Seidl, G. S. Tompa, and A. Souzis, J. Vac. Sci. Technol. A **5**, 1250 (1987).
[26] H. Liebl, Vacuum **33**, 525 (1983).
[27] A. Adams and F. H. Read, J. Phys. E **5**, 150 (1972).

A new solid-state cesium ion source

S. I. Kim and M. Seidl

Physics/Engineering Physics Department. Stevens Institute of Technology. Hoboken. New Jersey 07030

A novel Cs⁺ ion source combining the advantages of porous metal ionizers with those of zeolite emitters has been developed. Cesium ions are chemically stored in a cesium-mordenite solid electrolyte (Cs-M SE) pellet whose emitting surface is coated with a porous tungsten thin film. Cesium supply to the emitting surface is controlled by a voltage applied across the solid electrolyte pellet. Cs⁺ ion emission takes place on the surface of the porous tungsten electrode by surface ionization. The ionic conductivity of Cs⁺ ion in the Cs-M SE is of order of 10^{-5} Ω cm⁻¹ at 1000 °C. The interface properties between electrolyte and electrodes play a major role in the cesium ion source. The cathode electrode interface (emitting electrode) determines the stability of the supply current density to the emitting surface. The lifetime of the source is found to depend on the anode interface. In a steady-state operation, an ion-emission current density of the order of 20 mA/cm² has been extracted for 30 h at a total ion-emission current of 100 μA at 1000 °C. This corresponds to 10 C of extracted charge.

I. INTRODUCTION

Cesium ions are widely used in secondary ion mass spectroscopy[1] (SIMS) in the production of negative hydrogen ions by surface conversion,[2] and in sources of cold electrons,[3] etc. There are two basic types of Cs⁺ ion sources presently available: porous metal ionizer,[4,5] shown in Fig. 1(a), and zeolite emitter,[6] Fig. 1(b).

Recently a novel solid source of Cs⁺ ions has been developed in this laboratory.[7,8] It combines the advantages of porous metal ionizers with those of zeolite emitters. A schematic diagram of the cesium ion source is shown in Fig. 1(c). Cesium ions are chemically stored in a cylindrical pellet of cesium-mordenite solid electrolyte (Cs-M SE). The pellet is operated at a temperature of about 1000 °C. At this temperature, Cs-M is a good ionic conductor for Cs⁺ ions. A porous tungsten thin film (about 1 μm in thickness) is sputter deposited on one circular face of the pellet while the anode is provided with a thick platinum coating. Cesium ions are driven to the porous electrode by the biasing current across the electrolyte which is controlled by the biasing voltage U_b. The cesium atoms diffuse through the porous tungsten electrode to its surface where they are emitted as ions or neutrals depending on the work function of the surface. The emitted ions are accelerated by the voltage U_a applied between the emission surface and the accelerator electrode. In this way, we could achieve a high performance solid-state cesium ion source which has the current density of a porous metal ionizer and the simplicity of a zeolite emitter. In this paper we present experimental studies of the Cs-M SE and porous tungsten electrode system. The theory of the metal-solid electrolyte interface has been published elswhere.[9,10]

In the first part of this paper, material aspects of the Cs-M SE such as structural and chemical properties and preparation of the pellet and of the electrodes will be discussed. In the second part, the effects of the interface properties on the ion transport from the electrolyte to the emitter surface will be presented. Finally, measurements of cesium ion and neutral emission will be discussed.

II. CESIUM-MORDENITE SOLID ELECTROLYTE (Cs-M SE)

A. Cesium mordenite (Cs-M)

Cs-M is a synthetic zeolite of formula $Cs_2O \cdot Al_2O_3 \cdot 10SiO_2$ (unit-cell formula is $4 \cdot Cs \cdot [(AlO_2) \cdot (SiO_2)_5]$) which has an aluminosilicate matrix with an interchangeable cation. The structure of Cs-M consists of a single-layer framework containing five-membered rings of the Al and Si tetrahedra. It has a two-dimensional channel system with
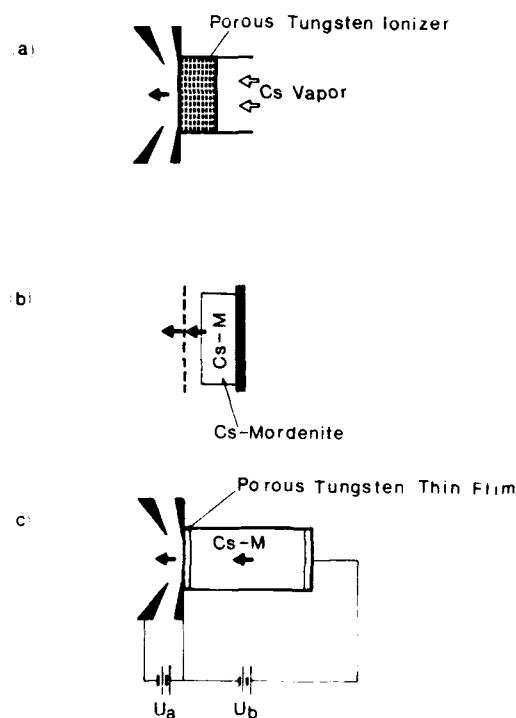

FIG. 1. Schematic diagram of various types of Cs⁺ sources. (a) Metal-ionizer-type source. (b) zeolite-type source. (c) our source, a combination of (a) and (b).

pore size about 6 Å in diameter. This is known as the large-port mordenite.[11]

1. Ion exchange

The Cs-M powder is formed from Na-M powder ($8 \cdot Na \cdot \{(AlO_2) \cdot (SiO)_x\}$) (large-port Na-M, Union Carbide, Inc.) by the ion-exchange method.[13] The sodium cation is exchange for cesium in a CsCl acid solution. Ion exchange is done by the following method: 31 g of Na-M powder in a 2 M CsCl solution is heated at about 80 °C with magnetic stirring for several days. The solution is filtered through a vacuum frit (5 μm) and the residual powder is dried in a hot vacuum oven (200 °C).

2. Phase transformation

The ion-exchanged Cs-M is in an unstable phase both chemically and structurally. Chemical analysis (Table I) shows that the ion-exchanged Cs-M contains more cesium than the stoichiometric value as well as residual sodium. X-ray powder diffraction of the ion-exchanged powder shows that it still has a Na-M structure. It has been found that the structural change to Cs-M occurs after firing the powder above 1050 °C. After transformation, Cs-M is stable in chemical composition (Table I).

By differential thermal analysis (DTA), two exothermic reactions are observed at 1050 °C and 1420 °C. The former one is due to the phase transformation (Na-M structure to Cs-M structure) and the latter is due to glass transformation (melting).

3. Pellet preparation

The ion-exchanged Cs-M powder is fired at 1050 °C. The recrystallized Cs-M is crushed and ground in a high-purity zirconia ball mill. The particle size of the Cs-M powder is controlled by the grinding time in the ball mill. After grinding, the powder is dried in a hot vacuum oven (200 °C) and it is press formed in a hardened-steel cylindrical plunger (0.95 cm in diameter) at a pressure of about 200 atm. The cylindrical pellet is sintered at 1350 °C for 3 h. The final density of the pellet depends on the particle size and also on the sintering time and temperature. At a sintering temperature and time given above, the densities of the sintered pellets vary in the range of 2.00–2.6 g/cm³ for presintered particle sizes from 3 to 1 μm. Theoretical density of the Cs-M is 2.83 g/cm³.

B. Electrode preparation

The emitting cathode is made by sputter deposition of tungsten. A triode magnetron sputter source (I. M. Simard

Inc.) has been used. To obtain a porous thin film, high pressure (about 30 mTorr) of argon gas has been used. The deposition rate of the thin film is about 2 A/s at a target current density of 0.5 A/cm², and a target voltage of 500 V$_{dc}$. The thin film has a submicron size of pores and pore density of the order of 3×10^8 /cm². SEM pictures of the porous tungsten thin-film electrode are shown in Fig. 2.

The anode electrode is prepared by applying platinum paste (Engelhard). Thick platinum paste is painted and it is cured at 800 °C for 2 h.

C. Ionic conductivity

In Cs-M SE, Cs⁺ is the only mobile charge moving through the negatively charged matrix skeleton by the hopping mechanism.[15] Figure 3 shows the temperature depend-
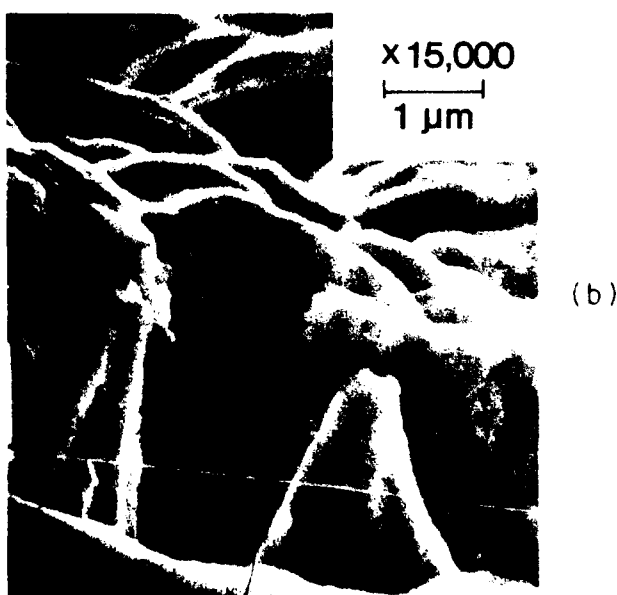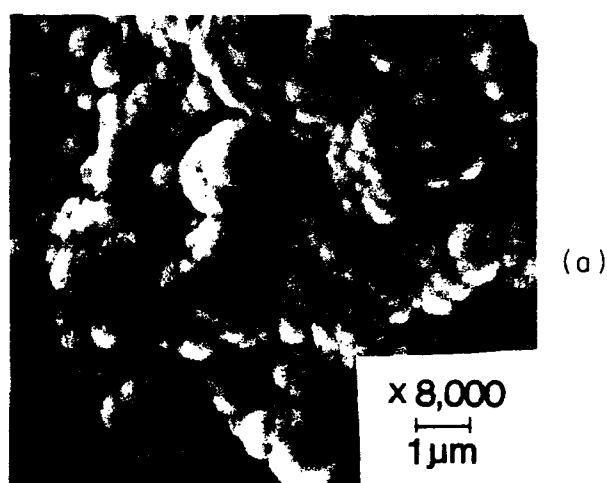

(a)

×8,000
⊢——⊣
1 μm

×15,000
⊢——⊣
1 μm

(b)

FIG. 2. Morphology of the porous tungsten thin film (a) Top view, (b) cross-sectional view.

TABLE I. Chemical analysis by EDX (in wt. %)

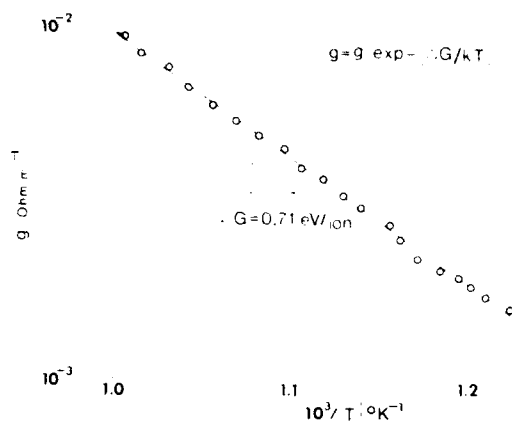|	Al	Si	Cs	Na	Cs/Si	Al/Si
Ion exchanged	3.3	33.4	55.2	0.1	1.65	0.1
Sintered	7.1	49.7	43.2		0.87	0.14
Stoichiometry	8.8	49.3	41.9		0.85	0.18

FIG. 3. Temperature dependence of the Cs⁺ ion conductivity.

ence of the cesium ion conduction. The ionic conductivity g has an Arrhenius-type dependence on the temperature; $g = g_0 \exp - (\Delta G^0/kT)$. The activation energy of the ionic conduction ΔG^0 is found to be 0.71 eV/ion. The effect of the current on the conductivity is negligible in the current density range up to 1 mA/cm². A slight decrease of conductivity has been seen in the high-current range (> 1 mA/cm²).

III. ION TRANSPORT ACROSS THE INTERFACE

A. Interface process

A comprehensive theory of the metal-SE interface has been presented elsewhere.[9,10] Distribution of the space charge and the potential across the interface are shown in Figs. 4(a) and 4(b). The electrified interface (i.e., double layer) consists of the inner layer and the diffusion layer. Those layers are equivalent to a series connection of two capacitors.
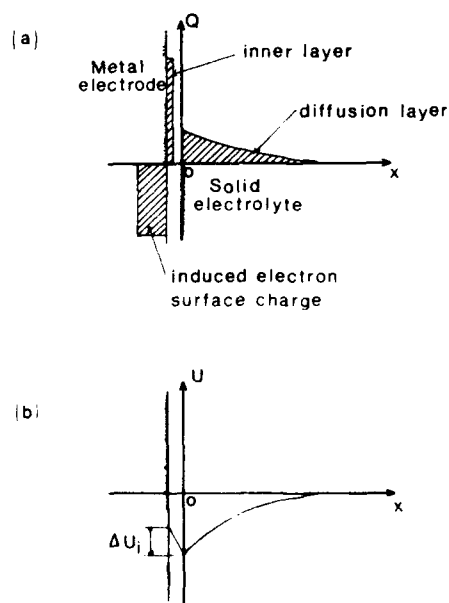

FIG. 4. Electrified interface between the metal electrode and solid electrolyte. (a) Space-charge distribution in the interface double layer. (b) potential distribution.

1. Current interruption method

In order to explore the interface properties, the current interruption method[14] is employed, using the circuit diagram given in Fig. 5. The cathode and the reference electrode are electrically separated by a groove in the porous tungsten thin film. The pellet is heated with the tungsten filament and placed inside the cylindrical cavity in the pellet. A constant current source has been used. The interruption of the current is controlled by a mercury relay with a response time of less than 10⁻⁴ s. The potential of the cathode with respect to the reference electrode is measured by an electrometer and the output signal from the electrometer is plotted with a high-speed strip chart recorder.

The current interruption method is a technique of constant current interruption chronopotentiometry. A constant current is applied between the anode and the cathode. [Fig. 6(a)]. Since the reference electrode is not affected by the biasing current, the dependence of the electrochemical properties such as current-overpotential characteristics and the capacitances of the double layer could be obtained by measuring the potential difference between the reference electrode and the cathode electrode. The schematic diagram of potential transient by current interruption is shown in Fig. 6(b). The abrupt drop of the potential is the potential drop across the bulk of the electrolyte (i.e., ohmic). The transient of the potential is the interface potential (i.e., electrochemical overpotential). Two different time constants of the interface potential decay have been observed. It is believed that this is the effect of the double layer (i.e., inner layer and diffusion layer) at the interface.

2. Electrode reaction

There are charge-transfer reactions on both of the electrodes:

(anode) Cs-M = Cs⁺ + M⁻ = Cs⁺ + M + e, (1a)

(cathode) Cs⁺ + e = Cs°, (1b)
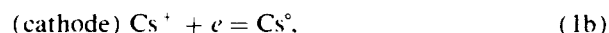
where M is the matrix anion $[(AlO_2)\cdot(SiO_2)_x]$. Electric field is applied between the anode and cathode electrodes. Cathode electrode is the emitting electrode in cesium source arrangement as shown in Fig. 1(c). On the anode, the matrix anions (M^-) are deionized and the electrons are transferred
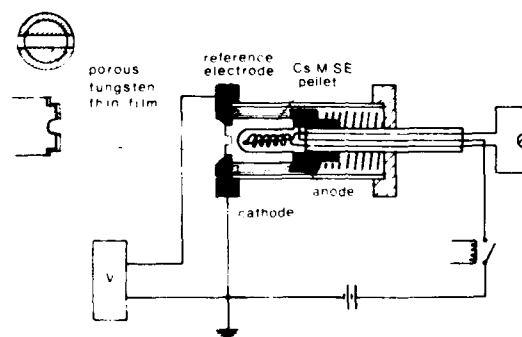

FIG. 5. Schematic diagram of the conductivity and interface potential measurements (cathode and reference electrodes are drawn in large scale on the upper left-hand side).
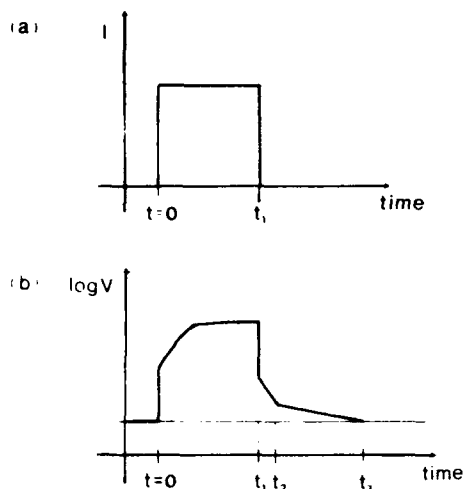
(a)

(b)

FIG. 6. The current interruption method. (a) Constant current is applied and current interruption is made after the steady state is reached. (b) potential transient of the cathode with respect to the reference electrode.

anode metal electrode as indicated in Eq. (1a). Cs^+ ions are driven to the cathode and neutralized on the cathode as in Eq. (1b). The neutralized cesium atoms diffuse through the porous tungsten cathode to its surface where they evaporate as either ions or atoms.

B. Cathode interface

At the cathode interface, cesium ions are accumulated and a *double layer is formed. The measured current-overpotential characteristics for the cathode by using current-interruption method are presented in Fig. 7.* In order to compare the results with Ref. 10, the measured current density is normalized to the exchange current, obtained numerically in Ref. 10. The exchange current is only a function of temperature. A good agreement between theoretical curves and experimental results has been found. The limiting current density across the interface is about the same as the exchange
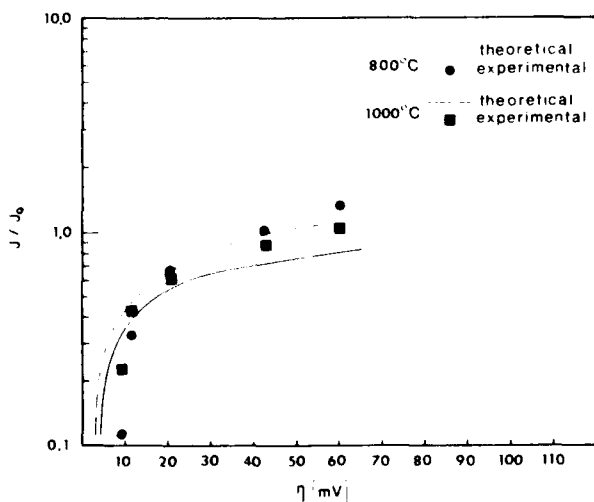

FIG. 7. Current-overpotential characteristic (curves are obtained numerically in Ref. 10).

current. A typical limiting current density of the order of 1 mA/cm^2 has been observed at 1000 °C.

The capacitances of the double layer depend on temperature and current density. The absolute value of the capacitances of the double layer could not be measured by the current interruption method, however, and the difference of the capacitances between the steady state ($J \neq 0$) and the equilibrium state ($J = 0$) could be obtained. The typical capacitances and time constants (at 1000 °C, $J = 50 \mu A/cm^2$) are found to be of the order of millifarad and minutes for the diffusion layer and of the order of a few tens of microfarad, and seconds for the inner layer.

C. Cesium diffusion through the porous tungsten electrode

The dc steady emission current depends on the steady supply of cesium onto the surface of the emitting electrode. As seen on the schematic diagram of the ion source [Fig. 1(c)], the supply of cesium is provided by the biasing current in the electrolyte and cesium diffusion through the porous tungsten electrode. The biasing current can be controlled externally by the biasing voltage, however, and the cesium diffusion through the porous tungsten electrode depends only on the concentration gradient which cannot be controlled externally. According to the theoretical results of the previous paper, high coverage (about 0.4 at 1000 °C) is found on the tungsten surface at the interface which is the inner layer in Fig. 3(a). The high coverage of cesium on the interface automatically enhances the cesium diffusion through porous tungsten electrode. Cesium diffusion through porous tungsten has been extensively studied. [15] Since our emitter is a fine porous structure (submicron pore diameter, Fig. 2), not a capillary tube, one can neglect the gas phase transport. The equation for the surface diffusion of cesium through porous tungsten is

$$ J = q \cdot \delta \cdot N = q \cdot \delta \cdot \left[2\pi a \cdot \sigma_o \cdot D \cdot \left(\frac{d\theta}{dx} \right) \right], \qquad (2) $$

where q is a charge of an electron, δ is the number of the pores in a unit area ($\delta = 2.8 \cdot 10^8$ cm^{-2}), N is the cesium flux per one pore, a is the pore radius ($a = 0.05 \mu m$) σ_o is the number of cesium per unit area in a filled monolayer on tungsten ($\sigma_o = 4 \cdot 10^{14}$ cm^{-2}), D is the surface diffusion coefficient for cesium on tungsten ($D = 1.0 \cdot 10^{-3}$ cm^2/s at 1000 °C), and θ is the coverage of cesium on tungsten. Assuming a linear gradient of cesium coverage through the electrode (i.e., $d\theta/dx \approx \theta/1$, 1 being the thickness of the emitter electrode, 1 μm) and zero coverage on the emitting surface, a cesium flux density J corresponding to 150 mA/cm^2 is obtained at 1000 °C. Thus cesium diffusion through the porous tungsten electrode is not the limiting factor for the supply of cesium onto the emitting surface.

D. Anode interface

On the anode, the matrix anions (M^-) are deionized and the electrons are transferred to the anode-metal electrode as seen in Eq. (1b). Since the matrix anions are fixed and no electron conduction occurs in Cs-M SE, there is a large electric field needed to pull the electrons to the anode

after one interface layer of anions is depleted. Figure 8 shows the voltage needed to draw a constant current measured as function of the amount of charge passed per unit area of anode surface. The sharp increase of the voltage after a critical amount of charge Q_0 could be explained by the depletion of electrons at the interface layer of matrix anions. The critical amount of charge Q_0 depends on the effective area of the interface, according to the equation

$$Q_0 \quad \sigma \cdot 1 \cdot A_{\mathrm{eff}} \cdot \qquad (3)$$

where σ is the charge density, 1 is the average interatomic distance between anions which is about 7 Å, and the effective area is $A_{\mathrm{eff}} = k \cdot A_0$ (where k is a constant and A_0 is a geometrical area). The constant k depends on the porosity, which in turn depends on the particle size d_0. The pore volume is proportional to d_0^{3}, thus the incremental factor of the effective area k is linearly proportinal to d_0^{3} (i.e., $k = \alpha \cdot d_0^{3}$). The value of $\alpha = 5.0 \cdot 10^{7}$ cm^{-1} has been empirically obtained for the 1-μm particle size. The values of Q_0 for the 2- and 3-μm particle size calculated by using Eq. (3) are shown in Table II. The calculated values reasonably agree with the experimental results in Fig. 8.

After depletion, the current depends exponentially on the applied potential which could be explained by the electron tunneling current through the depleted layer.[15] Thus the lifetime of the cesium source is limited by the anode depletion. Lifetime of the order of 10 C of cesium charge (corresponding to 300 h of operation with 10 μA) can be easily obtained by using about 5 cm^2 anode coating area.

IV. ION AND NEUTRAL EMISSION

A. Experimental arrangement

The schematic diagram of the measurement of ion and neutral emission is shown in Fig. 9. The Cs-M pellet is heated to its operating temperature (800 to 1200 °C) by an alumina-coated tungsten filament. The planar-diode-type arrangement has been used for ion extraction and the spacing between emitter and extracting mesh (145 · 145 tungsten mesh) is 0.2 cm. A Faraday cup is used to measure the ion current. In order to suppress secondary electrons due to the Cs$^+$ ion bombardment of the cup, a retarding field is applied in front of the cup. Thus the current to the Faraday cup is solely due to the ion-emission current. Cesium neutrals are
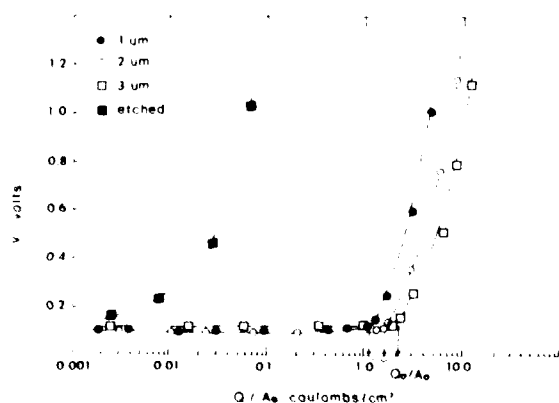
TABLE II. Calculation of critical charge for anode depletion.

d_0 (μm)	q (C·cm^{-3})	k ($\times 10^{5}$)	A_{eff}/A_0	Q_0 (C)	Q_0/A_0 (C·cm^{-2})
1	509	5.6		0.20	1.18
2	437	12.6		0.38	1.65
3	382	23.6		0.64	2.06

measured by a hot tungsten filament which is heated to 1700 °C. At this temperature, all the neutrals are ionized so that the neutral flux is equal to the ion current produced on the hot filament.

B. Surface ionization

On the emitter surface, Cs$^+$ ion emission takes place by surface ionization. The surface ionization process depends on the temperature and work function of the emitter surface according to the Sha-Langmuir surface ionization equation

$$J_n/J_i = w \cdot \exp[e(V_i - \phi)/kT]. \qquad (4)$$

where J_n and J_i are neutral- and ion-emission current densities, respectively. w is the statistical weight ratio of atoms to ions, $V_i = (= 3.9 \text{ eV})$ is the ionization potential of cesium, and ϕ is the workfunction of the metal electrode. From the slope of $\ln(J_n/J_i)$ as a function of $1/kT$ in Fig. 10, the effective workfunction of the emitting tungsten surface is calculated and its value is 4.2 eV.

C. Dependence of Cs$^+$ ion emission on cesium supply

In a steady-state operation, the ion-emission current density must be equal to the supply current density. Thus the Cs$^+$ ion-emission characteristics have to be studied in conjuctions with the supply of cesium to the emitter surface. In our Cs$^+$ ion source arrangement the supply is limited by the limiting current density across the interface and the self-consistent thermal leakage flux across the interface. In order to see the dependence of ion emission on cesium supply, ion-emission current was measured as function of extraction voltage with and without cesium supply by biasing current across the electrolyte. The I-V characteristic of ion emission is shown in Fig. 11. In the low-voltage range where a space-

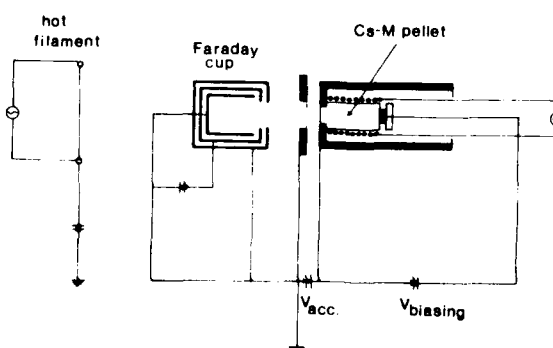FIG. 8 Critical charge of the anode depletion per unit area

FIG. 9 Schematic diagram of the measurement of the cesium ion and neutral emission
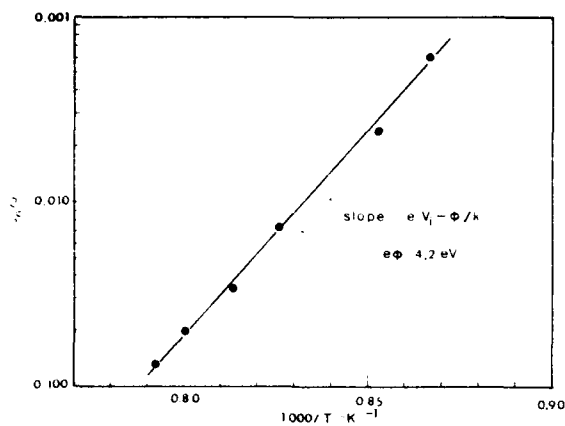
FIG. 10. Temperature dependence of the cesium ion and neutral emission.

charge-limited operation should be in effect, emission current density follows the Child–Langmuir law,

$$J = k \cdot V^{3/2}/d^2, \qquad (5)$$

where $k = 4.7 \times 10^{-8}$ V A cm for cesium, and $d (= 0.2$ cm$)$ is the spacing between the extraction mesh and the emitter surface. In the high-voltage range, the emission current is limited by the supply of cesium to the emitter surface. The emission currents have been extracted without biasing (i.e., open circuit between anode and cathode of the Cs-M SE pellet). The cesium supply without biasing could be explained by the thermal leakage flux across the interface
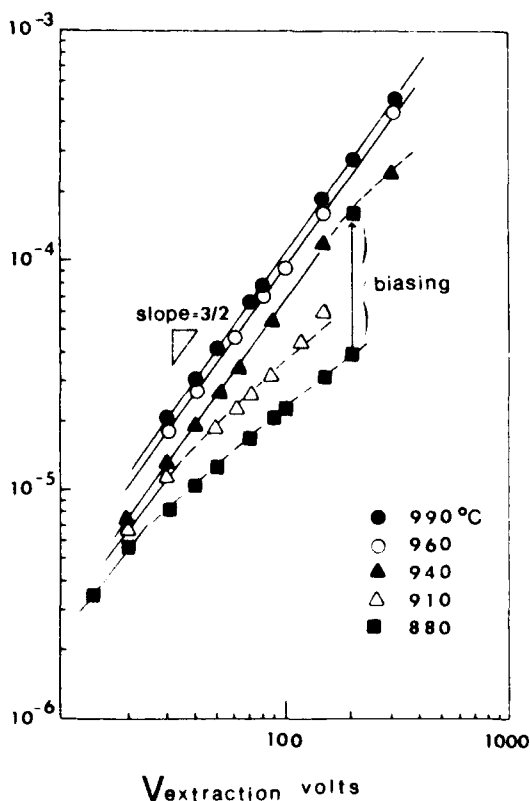

FIG. 11. I-I characteristics of Cs ion emission with and without biasing currents.

which is due to the self-consistent potential across the interface. With an additional supply of cesium by biasing current, one can extend the space-charge-limited region in the low-temperature range.

The thermal leakage flux is also observed in neutral emission. When there is no extraction field on the emitter surface, cesium is vaporized from the surface as neutral atoms. The flux is equal to the supply of cesium to the emitter surface in a steady state. Since there is no supply by external biasing current across the electrolyte, the neutral flux is just due to the thermal leakage flux. The dependence of the thermal leakage flux on temperature is shown in Fig. 12. The maximum space-charge-limited ion emission flux without supply by biasing current, shown in Fig. 11, is drawn as a dashed line in Fig. 12. It is seen that both fluxes are approximately the same. According to the potential diagram of the interface, shown in Fig. 4(b), an electric field directed in the x direction is produced by the interfacial potential difference ΔU_i between the tungsten electrode surface and Cs-M SE surface. The electric field is extracting electrons from the Cs-M SE surface. The electrons are then combined with the adsorbed cesium ions on the inner layer. The neutralized cesium atoms diffuse out to the vacuum interface of the emitting electrode. The flux of cesium is the thermal leakage flux across the interface. Thus one can interpret the results in Fig. 12 as the electron emission characteristics on the Cs-M SE surface. The linear slope in Fig. 12 indicates that the extracting field (i.e., potential difference across the interface, $\Delta U'$) is dependent on temperature. The potential difference across the interface, numerically obtained in Ref. 10, is almost constant in the temperature range 800–1000 °C.

There is one more piece of evidence that the thermal leakage flux is due to the electron emission from the Cs-M SE to the tungsten electrode surface. By observing the neutral flux over a long time, the neutral flux is decaying slowly with time. In the long run, the neutral flux goes to zero. The total amount of emitted neutrals is about equal to 1 ML of the M matrix anions. This fact is not only proving the mechanism of the thermal leakage flux but also provides a method for exact control of the supply of cesium to the emit-
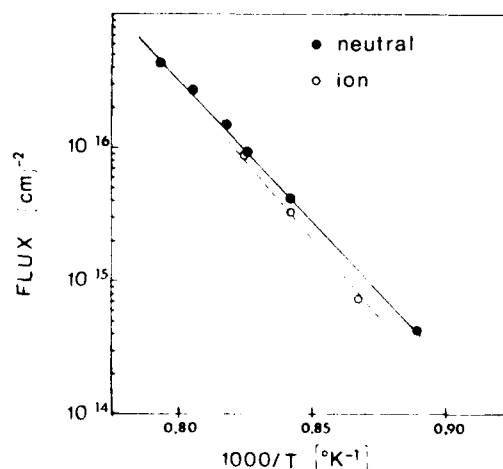

FIG. 12. Cesium neutral flux and the maximum space-charge-limited ion current density with a supply by the thermal leakage flux.

ter surface. After depletion of the electrons from the emitter interface, there is no supply of cesium by the thermal leakage flux. Thus the supply of cesium to the emitter surface is then exactly controlled by the external biasing current across the interface. Practically the electron charge to be depleted is of the order of 2 C/cm^3. This charge can be extracted in the reverse bias mode (i.e., positive potential on the emitting electrode and negative potential on the anode) in about 3 h at a total biasing current of 20 μA prior to using the ion source.

The supply of cesium to the emitter surface is now exclusively controlled by the biasing current across the electrolyte. However, the biasing current is limited by the maximum electrode reaction current density across the interface. From both theoretical and experiment results, the limiting current density across the interface is of the order of 1 mA/cm^2 at 1000 °C. In order to increase the emission current density to more than 10 mA/cm^2, we have modified the emitter configuration. A thin diaphragm with an aperture of 0.08 cm diam covers the emitter surface. Thus, all cesium supplied to the emitting electrode is delivered to this emitting aperture by surface diffusion. The ratio of the tungsten electrode area to the area of emitting aperture is about 200. Thus the emission current density is 200 times larger than the supply current density. In this way, one can obtain a high emission current density while minimizing the supply current across the electrolyte.

D. High Cs⁺ ion emission current density

In order to have a steady-state high-emission current density, the following extraction arrangement has been used: an extraction electrode with a single aperture, 0.08 cm in diameter, is aligned with the emitting aperture. The distance between the two apertures is 0.05 cm. All the other experimental arrangements are the same as in Fig. 9.

Since our source is a surface ionization source, the maximum ion-emission current density depends on the critical temperature of the emitter. The critical cesium ion-emission current density has been measured by Wilson[1,2] for several metal surfaces. His results are shown in Fig. 13 as solid lines. The points show experimental results obtained with our source for porous platinum and tungsten emitter coatings. The slightly smaller values compared to Wilson's data can be attributed to the porous surface of the emitter. In a de steady-state operation, up to 20 mA/cm^2 current density at a temperature of 1100 °C has been extracted for 30 h at a total current of 100 μA. The total amount of extracted cesium ions corresponds to 10 C.

V. SUMMARY

The new solid-state Cs⁺ source compares favorably with the metal-ionizer-type source with respect to the ion-emission current density and lifetime. It has the simplicity in construction and operation comparable to the zeolite-type source. Furthermore, it has the unique capability of exact control of cesium supply to the emitting electrode.
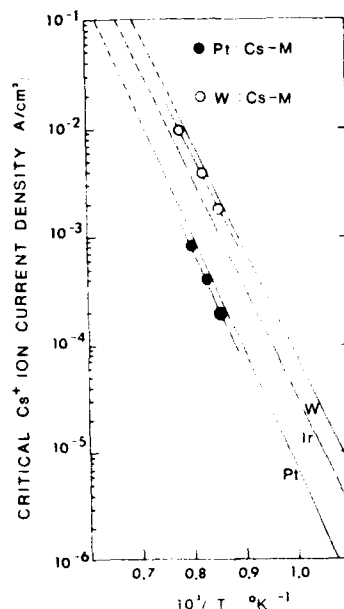

FIG. 13. Critical Cs⁺ ion current density (solid lines are from R. G. Wilson, J. Appl. Phys. 42, 972 (1965).)

A solid-state Cs⁺ ion microprobe (micron size beam and high current density > 10 mA/cm^2) has been developed by using this source. Design and operation of the microprobe will be presented in a forthcoming paper.

[1] H. A. Storms, K. F. Brown, and J. D. Stein, Anal. Chem. 49, 2023 (1977).
[2] J. L. Lopes, J. A. Greer, and M. Seidl, J. Appl. Phys. 60, 17 (1986).
[3] R. C. Martinelli, J. Appl. Phys. 45, 1183 (1974).
[4] G. R. Brewer, Ion Propulsion (Gordon and Breach, New York, 1970).
[5] D. G. Welkie, in Secondary Ion Mass Spectroscopy SIMS V, edited by A. Benninghoven et al. (Springer, New York, 1986), p. 146.
[6] O. Heinz and R. T. Reaves, Rev. Sci. Instrum. 39, 1230 (1968).
M. Seidl, A. E. Souzis, W. E. Carr, and G. Tompa, Pittsburgh Conference on Analytical Chemistry and Applied Spectroscopy, Abstr. No. 743, Atlantic City, 1986.
[7] M. Seidl, US Patent 4,783,595 (1988).
[8] S. I. Kim and M. Seidl, in Solid State Ionics, Vol. 135 of Materials Research Society Symposium Proceedings, edited by G. Nazri, R. A. Huggins, and D. F. Shriver (1988), pp. 95-100.
[9] S. I. Kim, Ph.D. thesis, Physics Engineering Physics Department Stevens Institute of Technology, Hoboken, NJ (1989).
[10] J. Ito, Am. Mine. 61, 170 (1976).
[11] D. W. Breck, Zeolite Molecular Sieves (Academic, New York, 1976).
[12] Y. Haven and P. Hagenmuller, in Solid Electrolytes, edited by W. van Gool (Academic, New York, 1978), Chap. 5.
[13] D. Y. Wang and A. S. Nowick, J. Electrochem. Soc. 126, 1155 (1979).
[14] A. T. Forrester, J. Chem. Phys. 42, 972 (1965).
[15] J. R. Bates and A. T. Forrester, J. Appl. Phys. 38, 1956 (1967).
[16] G. R. Brewer, Ion Propulsion Technology and Applications (Gordon and Breach, New York, 1970), p. 117.
[17] J. O'M. Bockris and A. K. N. Reddy, Modern Electrochemistry (Plenum, New York, 1970), Vol. 2, p. 254.
[18] R. G. Wilson, J. Appl. Phys. 37, 3161 (1966).
[19] R. G. Wilson, J. Appl. Phys. 42, 972 (1965).

Catalytic oxidation of silicon by cesium ion bombardment

A. E. Souzis, H. Huang, W. E. Carr, and M. Seidl

Physics/Engineering Physics Department, Stevens Institute of Technology, Hoboken, New Jersey 07030

Results for room-temperature oxidation of silicon using cesium ion bombardment and low oxygen exposure are presented. Bombardment with cesium ions is shown to allow oxidation at O_2 pressures orders of magnitude smaller than with noble gas ion bombardment. Oxide layers of up to 30 Å in thickness are grown with beam energies ranging from 20–2000 eV, O_2 pressures from 10^{-9} to 10^{-6} Torr, and total O_2 exposures of 10^0 to 10^4 L. Results are shown to be consistent with models indicating that initial oxidation of silicon is via dissociative chemisorption of O_2, and that the low work function of the cesium- and oxygen-coated silicon plays the primary role in promoting the oxidation process.

I. INTRODUCTION

Thermal oxidation of silicon typically requires heating to temperatures greater than 700 °C in O_2 pressures as high as 10^{-2} Torr with corresponding total oxygen exposures of 10^6 L ($1 \text{ L} \equiv 10^{-6}$ Torr s).[1] The ability to oxidize at low temperature and low O_2 exposure is of great interest since the rate of thermal defect production and the diffusion of impurities are greatly reduced. One possibility is to use an adlayer of vapor-deposited alkali metal as a catalyst. This has been seen to enhance the oxidation rate at room temperature by several orders of magnitude.[2] The alkali metal can then be removed by a relatively moderate 600 °C rapid thermal anneal (RTA). Thus, both the temperature and the exposure time are greatly reduced. Bombardment with noble gas ions at keV energies has also been seen to increase the room-temperature oxidation rate.[3] An advantage of this method is that the oxide can be formed by direct pattern writing with the ion beam. However, the necessary O_2 exposure is still quite high. We show that by using cesium ions as the primary bombarding species, these two methods can be combined, thus enabling the direct writing of SiO_2 at room temperature and low O_2 exposure.

In this work we present a study of SiO_2 formation on Si(100) using Auger electron spectroscopy (AES), ultraviolet photoelectron spectroscopy (UPS), and work-function shift measurements. Oxide formation due to cesium ion bombardment is compared to that due to xenon and argon bombardment. Xenon is used because its mass is essentially equal to that of cesium, thus the only changes will be due to electrochemical differences. Data are presented as a function of incident ion energy and mass, target temperature, and ion-to-O_2 flux ratio. Oxide layers up to 30 Å in thickness have been grown with beam energies ranging from 20–2000 eV, and O_2 pressures from 10^{-9} to 10^{-6} Torr. Total oxygen exposures of 10^0 to 10^4 L have been used.

II. EXPERIMENTAL DETAILS

These experiments are performed in a UHV chamber with a base pressure of $4 \cdot 10^{-11}$ Torr. This system has been described in a previous paper,[4] but the main details will be repeated here, including any variations from the previous arrangement. The sample is mounted on an *xyz* manipulator with both azimuthal rotation and sample tilt. It is also capable of electron-beam heating and liquid-nitrogen cooling of the sample. The system is equipped with a double pass, angularly resolved cylindrical mirror analyzer (CMA), with a coaxial electron gun for AES analysis, a low-energy electron gun for work-function (WF) shift measurements, a tunable light source and/or He-Ne laser (1.96 eV) for photoemission onset measurements, an ultraviolet discharge lamp for UPS analysis, low- (5–50 eV) and high- (100–5000 eV) energy cesium ion guns, and a noble gas ion gun. AES data are taken using minimal electron current (~ 5 μA) and analysis time ($\lesssim 30$ s), to eliminate any electron bombardment-induced changes in the oxide film.[5] UPS is performed using He I ($h\nu = 21.2$ eV) and He II ($h\nu = 40.8$ eV) discharges. He II data allow us to examine the valence-band density of states (DOS) up to 20 eV below the Fermi level due to the lower secondary electron background in the region of interest. The He I discharge has a much higher intensity, and hence a better signal-to-noise ratio. UPS is seen to be very surface sensitive, showing strong oxide features even when very little is detectable with the AES. UPS spectra are taken in the constant resolution mode of the CMA, at a pass energy of 25 eV, which corresponds to an energy resolution of 0.2 eV. Chamber pressures during the UPS analysis were $\sim 1 \times 10^{-8}$ Torr for He I, and $\sim 3 \times 10^{-9}$ Torr for He II. We found the He gas to have no detectable effects on the results at these pressures. The cesium guns are of our own design, use solid electrolyte sources, and are described in detail elsewhere.[6] Operation of these cesium ion guns does not result in a pressure rise above $\sim 2.5 \times 10^{-10}$ Torr. The noble gas ion gun is of the electron ionization type and is differentially pumped. It has separate bakeable UHV leak valves for the introduction of research purity xenon and argon. Chamber pressure while the gun is operating is $\sim 4 \times 10^{-9}$ Torr. Work-function shifts are measured using the retarding field diode method,[7] and the absolute work function is found by using photoemission onset data to determine a calibration point.

The Si sample is *n*-type (100), 5–9 Ω cm, and is cut from a commercial wafer. It is chemically etched before insertion into vacuum and is subsequently cleaned by sput-

ter bombardment with the cesium ion gun, typically 1 μA at 500 eV, and annealing at 800 °C. This procedure results in an oxide- and contaminant-free surface as determined by AES. Research purity O_2 gas is admitted through a bakeable UHV leak valve. The oxidation is accomplished by exposing the sample to an ion beam rastered across its surface, while at the same time exposing it to a flux of oxygen. After exposure, the target is heated to 600 °C for 10 min to remove the bombarding species, resulting in a clean SiO_2 layer. This is verified by using AES and UPS. The SiO_2 thickness is estimated by monitoring the attenuation of the AES Si (92 eV) signal through the oxide overlayer. It is calculated using the equation

$$I_{S_i} = I_{S_i}(0)\exp(-d/\lambda), \tag{1}$$

where I_{S_i} and $I_{S_i}(0)$ are the coated and clean AES peak heights of the Si (92 eV) signal, λ is the mean free path of the 92-eV electrons in SiO_2, and d is the oxide thickness. A value of 6.5 Å is used for λ, which includes a geometrical factor to account for the analyzer.[8] The noise level in the AES signal limits the data taken with this method to a thickness of $\sim$ 32 Å. This is sufficient for our results, as all our data are within this limit. The SiO_2 thickness is also reflected qualitatively by the size of the shoulder in the He I spectra at a binding energy of -3 eV. This shoulder is due to photoemission from elementary Si under the oxide film. Data collection and experimental control are accomplished using an AT&T microcomputer (IBM-AT compatible), which is equipped with an A to D converter, and an IEEE 488 bus controller. All of the experimental control software is developed in hous

III. RESULTS

A. Noble gas ion bombardment

Data are taken of oxide thickness versus oxygen-to-incident-ion-flux ratio for both xenon and argon bombardment. For an ion current density of 1 μA/cm^2 a flux ratio of 10 corresponds to an oxygen pressure in the chamber of 8.6×10^{-8} Torr. For a fixed flux ratio, oxide thickness increases with exposure until a steady state is reached. An exposure time of 1 h at this incident ion flux is found to be sufficient to reach steady-state thickness. Any increase in this exposure time results in negligible changes in oxide thickness. The time necessary to reach steady state is found to be directly proportional to the ion flux, or putting it another way, equilibrium is established only after a fixed dose of bombarding ions has been reached. This fixed dose is approximately 2×10^{16} ions/cm^2 s. The thickness under steady-state conditions, at a fixed energy, is seen to depend only on the ratio of oxygen to incident ion flux.

In Fig. 1 we show oxide thickness versus flux ratio for xenon ion bombardment, with ion energy as a parameter. For xenon, there is an oxidation onset at a ratio of about 8, after which the oxide thickness increases rapidly to around 25–30 Å. At this point, the growth rate of oxide as a function of flux ratio slows dramatically. There is no significant difference in the results when bombarding with 500 or 2000-eV ions. On the other hand, in Fig. 2 we show data
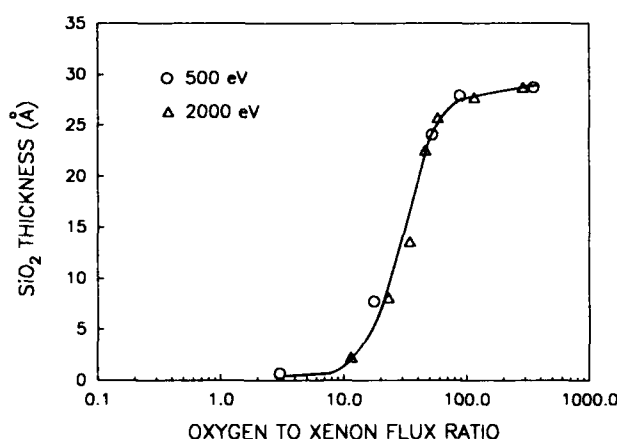

FIG. 1. SiO_2 thickness as a function of the oxygen-to-xenon-ion-flux ratio. The line is drawn merely to guide the eye.

taken under identical conditions for argon bombardment. Except for a slight change in the onset to a value of around 5, the 500-eV results are seen to be almost identical to the xenon data. The 1000- and 2000-eV results are significantly different. The onset of oxide formation does not change, but the rate of increase of the oxide thickness as a function of the oxygen-to-ion-flux ratio decreases as the bombarding energy increases. This results in the formation of thinner oxides for a given flux ratio.

AES data taken before heating for both xenon and argon bombardment, at all energies and pressures, show spectra characteristic of clean SiO_2, with its major peak at $\sim$ 77 eV.[8] Only trace ($< .04\ I_{\text{oxide}}$) amounts of noble gas are detectable. After heating, no noble gas can be detected with AES, while the oxide spectra remain unchanged. UPS data confirm this result. The initial spectra show peaks at -8.0, -12.0, and -14.7 eV, which remain unchanged upon heating. These peak positions and shapes are in excellent agreement with previously published data for clean SiO_2.[9]
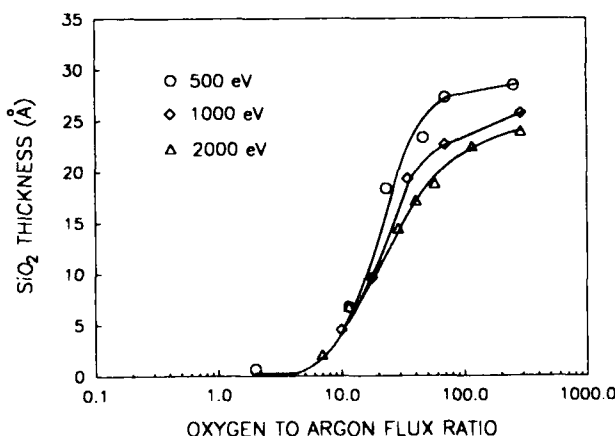

FIG. 2. SiO_2 thickness as a function of the oxygen-to-argon-ion-flux ratio. The lines are drawn merely to guide the eye.
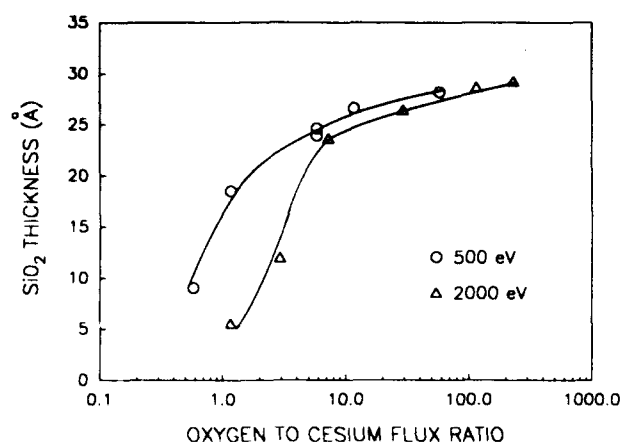
FIG. 3. SiO₂ thickness as a function of the oxygen-to-cesium-ion-flux ratio. The lines are drawn merely to guide the eye.

FIG. 4. SiO₂ thickness as a function of oxygen pressure, for 1-h exposures at 20 eV cesium ion energy and 1 μA/cm² cesium flux. The line is drawn merely to guide the eye.

B. Cesium ion bombardment

In Fig. 3 we again show oxide thickness as a function of oxygen-to-ion-flux ratio, this time for cesium ion bombardment. In this case, for runs of 500 or 2000 eV, the thickness ($\sim$ 30 Å) at which the rate slows does not vary. There is a difference however, in the value of the flux ratio at the onset. The higher-energy bombardment causes a shift in the overall curve to higher flux ratios. The oxidation onset occurs at approximately 0.2 for 500 eV and 0.7 for 2000 eV. These ratios are more than 1 order of magnitude smaller than the corresponding onsets for xenon and argon. At an incident ion flux of 1 μA/ cm², a ratio of 0.2 corresponds to an oxygen pressure of approximately 2×10^{-9} Torr. Data taken at 300 eV are consistent with this trend, indicating that the onset shifts to smaller ratios as the energy decreases. As with noble gas ion bombardment, the steady-state thickness is found to depend only on the ion-to-oxygen-flux ratio, and is established only after the same total dose of $\sim 2 \times 10^{16}$ ions/cm² is reached. Data are also taken at 2000 eV for sample temperatures of 200 and 300 °C. They show similar oxidation curves, except that they are shifted towards far higher flux ratios. At a sample temperature of 200 °C, the onset occurs at a flux ratio of $\sim$ 20, and for 300 °C it occurs at $\sim$ 50.

In a previous paper we have discussed the formation of a steady-state coverage of cesium under ion bombardment.[10] Data for cesium bombardment alone indicate that the steady-state cesium coverage is $\sim$ 0.5 monolayers (ML) at 500 eV, and $\sim$ 0.35 ML at 2000 eV. Monolayer coverage is defined here as a surface density of 6.78×10^{14} atoms/cm². Data taken for substrate temperatures ranging from $-$ 100 to 300 °C show that for 2000 eV bombardment, the steady-state cesium coverage is independent of temperature. These coverages are estimated from work-function shift measurements, and from previously published data relating the coverage of cesium on a silicon surface to the ratio between the 47-eV cesium, and the 92-eV silicon AES signals.[11] It should be noted that these are composite coverages due to ion bombardment, not pure coverages as typically achieved by vapor deposition.
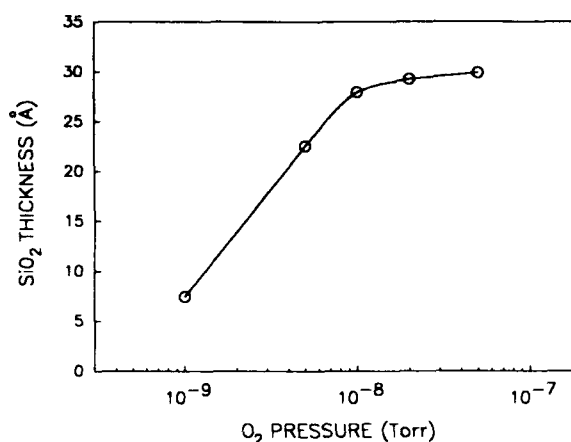
As with the noble gas ion bombardment, AES data at 500 and 2000 eV, taken before heating, show spectra which indicate that an SiO₂ coating is present. In this case however, heating makes a significant difference in the spectra. The oxide peak height before heating is $\sim$ 0.47 times the peak height after heating. This is consistent with a picture of an SiO₂ film covered with a submonolayer coating of cesium and oxygen. The peak height is smaller due to attenuation through this top layer. Before heating there is a large ($\sim$ 3 times oxide) cesium peak at 47 eV. After heating, this peak is gone. This result is supported by UPS spectra, where at both 500 and 2000 eV, evidence is seen for a SiO₂ film underneath an oxygen and cesium coating. The complete UPS spectra have a complicated dependence on experimental conditions, and will be shown and reviewed in detail at the end of this section.

C. Low-energy cesium deposition

Data are taken for 20 eV cesium ion bombardment with concurrent exposure to oxygen. As opposed to the previous sections, in this case there is no intermediate steady-state oxide thickness. The oxide grows continuously with exposure at a fast rate until it reaches a thickness of around 30 Å. At this point, the rate slows as seen in the previous data. This effect is present even at the lowest O₂ pressures used, which in this case was 1×10^{-9} Torr. At an O₂ pressure of 1×10^{-8} Torr, and 1 μA/cm² incident ion flux, a 1-h exposure time is sufficient to grow a 30-Å oxide film. At 1×10^{-9} Torr, a 1-h run grows a 7-Å film. However, by performing successive runs, the oxide film becomes thicker, and steady state can be reached. After five successive 1-h runs at 1×10^{-9} Torr the oxide thickness is 25 Å. In Fig. 4 we show the oxide thickness as a function of oxygen pressure for 1-h exposure times at a cesium flux of 1 μA/cm².

If the target is exposed to oxygen after dosing with cesium, instead of simultaneously, the thickness of the oxide is significantly smaller. For example, an oxide film grown with a total cesium dose of 3×10^{16} ions/cm² fol-

lowed by an O_2 exposure of 18 L (5×10^{-9} T for 1 h) has a thickness of 6.6 Å. A run performed under essentially the same conditions, but dosing the sample simultaneously results in an oxide thickness of 22.5 Å (see Fig. 4). Previously published work-function data taken on samples dosed sequentially show that for cesium coverages greater than ~0.5 ML, the work function as a function of oxygen exposure decreases, passes through a minimum, and then increases to a value larger than that before oxygen exposure.[4] AES data taken on a cesiated target both before and after an oxygen exposure sufficient to reach the minimum work function show an ~50% increase in the height of the 47-eV cesium peak, with no corresponding increase in the 563- and 575-eV cesium peaks. This is consistent with work done by other authors,[11,12] indicating that the oxygen adsorbs beneath the cesium, close to the silicon surface. The increase in the low-energy cesium peak is due to an increase in reflection from the electronegative oxygen layer beneath the cesium. The higher-energy cesium electrons are not affected, as their mean free path is significantly larger.

AES data taken before and after heating show a marked difference. Before heating we see a large peak at 47 eV corresponding to cesium. The silicon spectra look very different. There is a very small SiO_2 peak at 77 eV, a small Si peak at 92 eV, and much larger (~20 times SiO_2) peaks at 59 and 63 eV. The AES fine-structure spectra is known to be sensitive to the chemical environment of the silicon oxide species.[13] After heating, the cesium peak has disappeared, and the characteristic SiO_2 spectra has returned, with a large peak at 77 eV, and slightly smaller (~0.5 times SiO_2) peaks at 59 and 63 eV. We interpret these results to indicate that before heating, the silicon is in a different oxidation state. UPS spectra are also consistent with this result. As opposed to the higher energy bombardment, no evidence is seen for an SiO_2 layer beneath the oxygen and cesium overlayer. This interpretation is consistent with previously published core-level photoemission spectroscopy data where it is claimed that for vapor deposition of cesium and oxygen, several oxide states exist, and that the SiO_2 state does not form until after heating.[14]

D. UPS data

In Fig. 5, we show five different UPS He II spectra taken at various oxygen pressures and cesium energies after a 1-h exposure, but before heating to remove the cesium. The curves are labeled (a)–(e) on the figure. They indicate the presence of an overlayer consisting of a mixture of cesium oxide species. Some spectra imply a predominance of one species or another, and this is so indicated in the following description.

Figure 5(a): This data represents 20 eV bombardment at an O_2 pressure of 5×10^{-9} Torr. The three peaks at – 3.0, – 5.7, and – 7.7 eV belong to the $O_2^- \rightarrow O_2 + e$ process. This implies the presence of Cs_2O_2.[15] No evidence is seen of SiO_2.

Figure 5(b): This curve is for 20 eV bombardment at an O_2 pressure of 5×10^{-8} Torr. The four peaks that are at 2.4, – 5.0, – 6.9, and – 8.9 eV are assigned to the
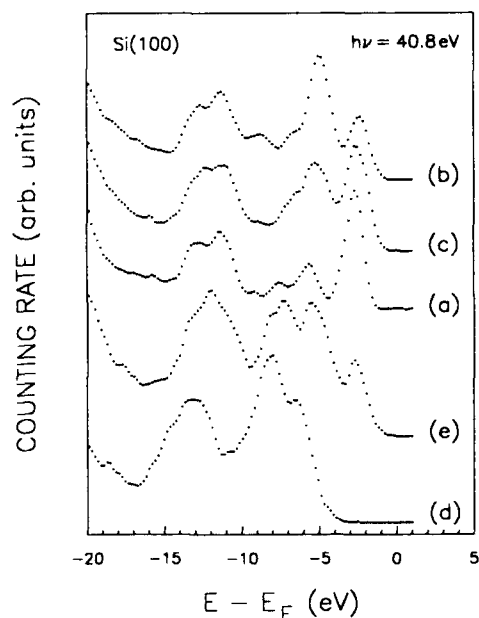

FIG. 5. UPS spectra taken before heating for various cesium energies and oxygen pressures. These are as follows: (a) 20 eV and 5×10^{-9} Torr, (b) 20 eV and 5×10^{-8} Torr, (c) 20 eV and 2×10^{-8} Torr, (d) 2000 eV and 5×10^{-8} Torr, and (e) 500 eV and 5×10^{-8} Torr. E_f is the Fermi-level energy, and the y-axis scale is the same for all curves.

process $O_2^- \rightarrow O_2 + e$.[15] In fact, for this process there is a five peak multisplit. This fifth peak, in our spectra, is overlapped by the Cs 5p peak at – 11.3 eV. This process indicates the existence of CsO_2.[16,17] Again, no SiO_2 evidence is seen.

Figure 5(c): This represents 20 eV bombardment at an O_2 pressure of 2×10^{-8} Torr. This spectra shows characteristics somewhere between those of curves (a) and (b). This indicates that both Cs_2O_2 and CsO_2 are present.

Figure 5(d): This curve was taken for 2000 eV cesium bombardment at an O_2 pressure of 5×10^{-8} Torr. The two peaks at – 6.4 and – 8.0 eV are due to an overlap of the O^2 2p peaks and the first SiO_2 peak. The O^2 peaks indicate the presence at the surface of a cesium oxide such as Cs_2O.[15] The SiO_2 peak indicates that the oxide has already formed beneath the cesium oxide overlayer, in agreement with AES results.

Figure 5(e): This curve is for 500 eV bombardment at an O_2 pressure of 5×10^{-8} Torr. This spectra shows evidence of a mixture of the oxygen states mentioned above. The shoulder at – 8.0 eV is evidence for the existence of SiO_2 as in curve (d). Under these conditions, we conclude that all of the species mentioned above are present in some amount.

In Fig. 6, we show UPS He II spectra recorded during a complete heating cycle. The sample was bombarded at 20 eV, with an O_2 pressure of 5×10^{-9} Torr for 1 h. Each curve corresponds to 5 min of heating at the specified temperature followed by cooling to room temperature to take the measurement. The data show large changes from room temperature up to 500 °C. From 500 to 600 °C there is a shift of 0.8 eV in the curve, without significant shape
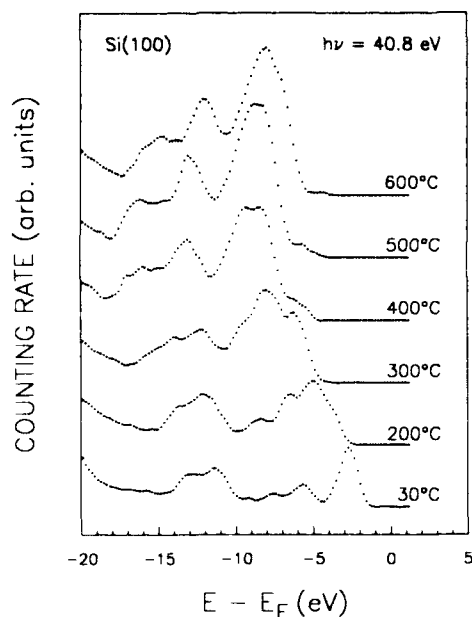
Si(100)   hν = 40.8 eV

600°C

500°C

400°C

300°C

200°C

30°C

COUNTING RATE (arb. units)

-20   -15   -10   -5   0   5

E − E$_F$ (eV)

FIG. 6. UPS spectra for a surface initially exposed for 1 h to 20 eV cesium ion bombardment with an oxygen pressure of $5 \cdot 10^{-9}$ Torr and then heated in stages to form SiO$_2$.

change. Further heating to 700 °C (not shown) results in no change in the curve. What we see is a gradual evolution from a room-temperature spectrum indicating Cs$_2$O$_2$ [as shown in curve c in Fig. 5] with no SiO$_2$ evident, to a 300 °C curve indicating Cs$_2$O [as shown in curve (a) in figure 5] with SiO$_2$ features beginning to make themselves evident. Finally, at 600 °C we have a clean SiO$_2$ spectrum. The thickness of this oxide is ~ 22 Å.

In Fig. 7, the low-energy secondary electron cutoff generated by He I is shown. These data were taken during the same heating cycle as above. The shift in the cutoff reflects the work-function change of the sample surface. For this run, the total shift is 3 eV. This represents an increase in the work function from a low value due to a cesiated and oxygenated surface to that of clean SiO$_2$. Pre-
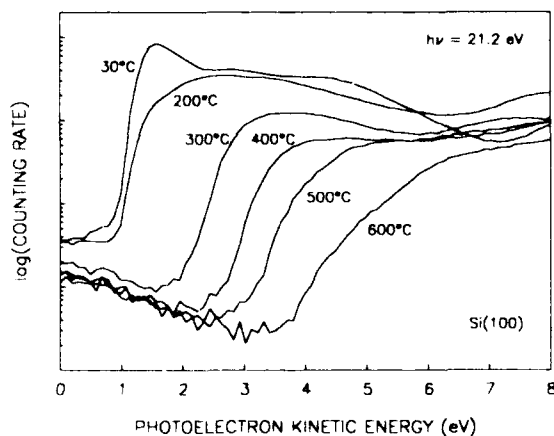

hν = 21.2 eV

30°C
200°C
300°C 400°C
500°C
600°C

Si(100)

log(COUNTING RATE)

0   1   2   3   4   5   6   7   8

PHOTOELECTRON KINETIC ENERGY (eV)

FIG. 7. Low-energy secondary electron cutoff for a surface initially exposed for 1 h to 20 eV cesium ion bombardment with an oxygen pressure of $5 \cdot 10^{-9}$ Torr and then heated in stages to form SiO$_2$.

viously published data indicate that the work function of thin SiO$_2$ films is between 0.5 and 0.75 eV below that of clean Si(100).[18] Using a value of 4.8 eV for clean Si(100), indicates that these cesiated and oxygenated surfaces have work functions $\leqslant 1.3$ eV. This is in agreement with our own previous work,[4] and with that of other authors, who measured similar low work functions for the various cesium oxides.[19]

IV. DISCUSSION

The process of silicon oxidation can be described in 3 basic steps: (i) sticking and dissociation of the O$_2$ molecule; (ii) Diffusion of the oxygen to the Si-SiO$_2$ interface; and (iii) oxidation reaction. Recent work, both theoretical and experimental, indicates that the initial oxidation of silicon is via dissociative chemisorption of oxygen.[20-23] It is also though that this dissociation of O$_2$ is the initial rate-limiting step for oxidation.[20] Our data are consistent with this interpretation.

Ion bombardment of silicon targets in the presence of gaseous oxygen creates surface damage and enhanced surface reactivity, which leads to enhanced near-surface (~ 5 Å) oxygen concentrations.[3] As the surface concentration increases, the overall concentration level as a function of depth will increase due to diffusion, all other conditions remaining equal. In addition, defect sites have been seen to serve as nucleation centers for SiO$_2$ formation.[24] These effects serve to increase the rate of all the steps outlined above. In addition to these effects, there is also sputter removal of target material. Oxide growth will taken place when the growth rate of the oxide exceeds the removal rate.

With the above in mind, we consider noble gas ion bombardment. In Figs. 1 and 2 the important difference is that for xenon bombardment, the oxidation is independent of energy for the range examined. This is not true for argon bombardment. For argon bombardment, the onset remains constant, but the slope of the curve becomes smaller as the energy increases. In other works, at a fixed flux ratio the oxide thickness decreases as the energy increases. The 500-eV argon curve is almost identical to the xenon curves. We have interpreted these results as follows. The enhanced surface reactivity and number of defect sites created are related to each other and are proportional to the amount of energy deposited per unit volume, close to the surface of the sample. Xenon, with a mass greater than 3 times that of argon, does not penetrate as far into the target at a given energy. LSS calculations indicate that for energies up to 2000 eV, the implantation depth of xenon ions is less than or equal to 30 Å. This is equal to or greater than the maximum oxide thickness formed in our experiments. Argon, on the other hand has an implantation depth greater than 30 Å at energies of 1000 eV and higher. Thus for xenon bombardment all the energy is deposited with in the oxide film, while for argon bombardment at 1000 eV and higher, some fraction of the energy is deposited outside the region of oxidation. This explains the slower rate of oxide growth for argon at high energy. The question now arises as to why the xenon bombardment curve is energy inde-

pendent. We believe that after a certain ion dose, the damage created lose to the surface saturates. The total dose of 2 × 10¹⁶ ions/cm² agrees well with our previous paper, in which we found that the composite surface coverage reached steady state after a similar dose, basically independent of energy.[10] It is also consistent with data published on damage produced by ion bombardment of silicon,[25] where computer calculations and experimental data indicate that bombardment-induced damage saturates at a total dose of ~ 3 × 10¹⁵ ions/cm².

For cesium ion bombardment, in Fig. 3 we have curves which are essentially similar to the noble gas curves except that he oxide growth onset is shifted more than an order of magnitude towards lower oxygen flux. This indicates that in addition to enhancing the oxidation by ion bombardment, the cesium has a catalytic effect of its own which increases the oxidation rate dramatically. This is in agreement with previous papers which saw a catalytic effect with cesium vapor deposition.[2,11,14] There are several factors which affect this catalytic promotion. One factor is that the presence of cesium at a silicon surface increases dramatically the sticking coefficient of oxygen,[18] leading to greater oxygen surface concentrations than can be obtained without cesium. As discussed previously, an increased surface concentration increases the overall diffusion profile. The other primary factor in this oxidation promotion is the reduced work function of the sample which occurs upon cesium and oxygen coating. Recent experimental[26] and theoretical[20] works have indicated that the effect of the low work function is to greatly enhance the rate of dissociation of the O₂ molecule on the silicon surface. Theory indicates that the mechanism for this effect is charge transfer from the low-work-function surface to the approaching O₂ molecule. This leads to an enhanced probability of finding the molecule in an excited O₂⁻ state, which is strongly dissociative. In Fig. 3, the effect of importance to note is that the data depend on energy, but not in the same way as the argon data. In this case the slope of the curve remains the same, but the onset shifts to higher oxygen ratios as the energy increases. The fact that the slope remains the same is consistent with our interpretation of the noble gas data, since cesium has essentially the same mass as xenon, and would thus cause similar damage due to bombardment. The shift in the onset to higher oxygen flux for higher energy is attributed to a coverage effect. In our previous work,[10] we demonstrated how the equilibrium coverage depends on a combination of factors, in this case the relevant one being the incident ion energy. Other experimental work has indicated that the catalytic effect of cesium coverage grows slowly at low coverages, with strong enhancement taking place for coverages 0.5 ML.[?] Our previous work showed that for cesium coverages of 0.25 ML and higher, the work function is more than 2 eV below the clean value, with the minimum occurring at 0.5 ML.[4] In addition, for coverages higher than 0.5 ML, the addition of oxygen resulted in an even larger shift, with an absolute work-function minimum of 0.9 eV occurring for oxygen adsorption on a sample coated with 1.0 ML of cesium. We have determined that at 500 eV, the steady-state coverage

is 0. ML, and for 2000 eV, it is 0.35 ML. Thus the shift in the oxidation curve is completely consistent with this explanation. At higher incident ion energy the cesium coverage is lower, hence the work-function shift and promoter effect are smaller, and a greater flux of oxygen is required to oxidize the sample. The increase in the flux of oxygen needed to maintain an SiO₂ film, as a function of sample temperature, is attributed to a reduction in the sticking coefficient for oxygen on silicon, between room temperature and 300 °C.[13] It is not due to any variation in the cesium coverage, as AES data discussed previously have shown that the coverage remains constant throughout this temperature range. In addition, if this effect were due to a reduction in the cesium coverage, the oxide formed would be identical to the xenon bombardment, since at these low temperatures the bombardment-induced damage is not greatly affected. In fact, significantly more oxygen is required at these temperatures than for the room-temperature xenon bombardment.

For 20 eV ion bombardment, there is no bombardment-induced oxidation. The only effect taking place here is the oxidation catalysis due to the presence of cesium. Even though there is no bombardment-induced enhancement, under identical exposure times the flux of oxygen needed to form an oxide coating is reduced by about an order of magnitude from that with 500 eV cesium bombardment. In addition, since there is no sputtering there is no onset as defined for bombardment. The amount of oxide is determined by the time of exposure, all other conditions being equal. For our data, as in Fig. 4, we used 1-h exposure times to remain consistent with the bombardment data. This increase in the catalytic effect is attributed to the larger coverage of cesium possible at these reduced energies. In addition, previously published work has shown that on silicon, the presence of cesium increases the sticking coefficient and maximum amount of oxygen that can be deposited, and that the presence of oxygen increases the saturation coverage of cesium.[18] Thus there is a synergistic effect which also explains why doing the exposures concurrently rather than sequentially gives much thicker SiO₂ coatings. UPS shows that for low O₂ pressure, the primary species is Cs₂O₂, while at higher pressures, such as 5 × 10⁻⁸ Torr, there is more CsO₂. Clearly, for the same surface coverage of cesium, CsO₂ provides more oxygen for the oxide formation process than does Cs₂O₂.

The fact that, under all experimental conditions, the oxide growth rate decreases dramatically as the film thickness approaches 30 Å is attributed to a reduction of oxygen reaching the interface region due to the existing oxide acting as a diffusion barrier. Other authors have oxidized silicon at room temperature with a 5-eV O beam. They claim a maximum thickness of ~ 17 Å for both the O beam case and a coating grown by steam oxidation, also at room temperature.[22] Their explanation also attributes this growth limitation to diffusion through the oxide layer. The discrepancy in thicknesses is most likely due to the fact that different methods are used in their determination. Other published work has investigated low-temperature microwave plasma oxidation.[25] In this paper the authors

extrapolate their data to zero substrate bias, which in essence leaves only diffusion as the transport mechanism. At zero bias they quote a value of 30 Å for their oxide thickness. This is in complete agreement with our data.

V. SUMMARY

The results that we have presented in this paper clearly demonstrate the effectiveness of using cesium ion bombardment as a method for low-temperature, low oxygen exposure, oxidation of silicon. Our results are consistent with models in which the initial oxide growth is limited by the dissociative chemisorption of O_2, while later, at room temperature, it becomes diffusion limited as the oxide thickness approaches 30 Å. Ion bombardment alone is seen to enhance the room-temperature oxidation rate due to an increased surface concentration of oxygen and a large number of defect sites which act as nucleation centers. Bombardment with cesium ions has the additional effect of creating a low-work-function surface. The dissociative chemisorption of O_2 is greatly enhanced by the presence of a low-work-function cesium oxide overlayer at the surface of the sample. Using low energy/vapor deposition of cesium allows even lower oxygen exposures than for higher-energy bombardment. This method has a drawback, in that it is difficult to localize the cesium flux at these low energies. At higher energies, it is easy to form a well-focused ion beam, and thus form SiO_2 only in the regions where the cesium beam hits the sample. The cesium is easily removed by a moderate heating, resulting in a clean SiO_2 film. Thus one can perform direct writing of thin SiO_2 layers at room temperature and low oxygen exposure. The thickness of the oxide is also precisely definable by control of the oxygen pressure. These thin oxides may have applications for use in tunnel diodes or any other device requiring precise control of oxide position and desired thicknesses of $\leqslant 30$ Å. Future work includes investigation of the quality of these oxides.

ACKNOWLEDGMENT

[1] G. Hollinger and F. J. Himpsel, Appl. Phys. Lett. **44**, 93 (1984).
[2] M. H. Bakshi, P. Soukiassian, T. M. Gentle, and Z. Hurych, J. Vac. Sci. Technol. A **5**, 1425 (1987).
[3] P. Sander, U. Kaiser, R. Jede, D. Lipinski, O. Ganschow, and A. Benninghoven, J. Vac. Sci. Technol. A **3**, 1946 (1985).
[4] A. E. Souzis, M. Seidl, W. E. Carr, and H. Huang, J. Vac. Sci. Technol. A **7**, 720 (1989).
[5] B. Carrère and B. Lang, Surf. Sci. **64**, 209 (1977).
[6] A. E. Souzis, W. E. Carr, S. I. Kim, and M. Seidl, Rev. Sci. Instrum. **61**, 788 (1990).
[7] A. G. Knapp, Surf. Sci. **34**, 289 (1973).
[8] J. Derrien and M. Commandré, Surf. Sci. **118**, 32 (1982).
[9] G. Hollinger, S. J. Sferco, and M. Lannoo, Phys. Rev. B **37**, 7149 (1988).
[10] W. Carr, M. Seidl, G. S. Tompa, and A. Souzis, J. Vac. Sci. Technol. A **5**, 1250 (1987).
[11] J. E. Ortega, E. M. Oellig, J. Ferrón, and R. Miranaa, Phys. Rev. B **36**, 6213 (1987).
[12] J. D. Levine, Surf. Sci. **34**, 90 (1973).
[13] P. Gupta, C. H. Mak, P. A. Coon, and S. M. George, Phys. Rev. B **40**, 7739 (1989).
[14] P. Soukiassian, T. M. Gentle, M. H. Bakshi, and Z. Hurych, J. Appl. Phys. **60**, 4339 (1986).
[15] C.-Y. Su, I. Lindau, and W. E. Spicer, Chem. Phys. Lett. **87**, 523 (1982).
[16] E. Bertel, F. P. Netzer, G. Rosina, and H. Saalfeld, Phys. Rev. B **39**, 6082 (1989).
[17] C. Wijers, M. R. Adriaens, and B. Feuerbacher, Surf. Sci. **80**, 317 (1979).
[18] M. Kamaratos and C. A. Papageorgopoulos, Surf. Sci. **219**, 317 (1989).
[19] B. Woratschek, W. Sesselmann, J. Küppers, G. Ertl, and H. Haberland, J. Chem. Phys. **86**, 2411 (1987).
[20] B. Hellsing, Phys. Rev. B **40**, 3855 (1989).
[21] U. Höfer, P. Morgen, W. Wurth, and E. Umbach, Phys. Rev. B **40**, 1130 (1989).
[22] M. H. Hecht, O. J. Orient, A. Chutijian, and R. P. Vasquez, Appl. Phys. Lett. **54**, 421 (1989).
[23] P. V. Smith and A. Wander, Surf. Sci. **219**, 77 (1989).
[24] F. M. Leibsle, A. Samsavar, and T.-C. Chiang, Phys. Rev. B **38**, 5780 (1988).
[25] D. J. Vitkavage, C. J. Dale, W. K. Chu, T. G. Finstad, and T. M. Mayer, Nucl. Instrum. Methods B **13**, 313 (1986).
[26] E. G. Michel, J. E. Ortega, E. M. Oellig, M. C. Asensio, J. Ferrón, and R. Miranda, Phys. Rev. B **38**, 13 399 (1988).
[27] H. I. Starnberg, P. Soukiassian, and Z. Hurych, Phys. Rev. B **39**, 12 775 (1989).
[28] T. Roppel, D. K. Reinhard, and J. Asmussen, J. Vac. Sci. Technol. B **4**, 295 (1986).

Resonant charge transfer in the scattering of hydrogen atoms from a metal surface

H. L. Cui

Department of Physics and Engineering Physics, Stevens Institute of Technology, Hoboken, New Jersey 07030

Electron transfer and the production of negative hydrogen ions in the reflection of hydrogen atoms from a metal surface is studied theoretically. Starting from the total Hamiltonian of the metal–atom system, the time development of the one-electron density matrix is determined. This is shown to be related to the time-dependent coupling of the affinity level of the moving atom with the metal states. In the limit of weak coupling, the occupation probability of the affinity level can be obtained in a closed form. This theory is applied to the problem of negative hydrogen ion production at a W(110) surface, both with and without Cs coverage, and the results are compared with available experimental data and predictions of existing theories.

I. INTRODUCTION

The problem of charge transfer during the reflection of a hydrogen atom (or H^+ ion) from a metal surface is of fundamental interest both from a theoretical point of view, and for practical applications. In the former case, it belongs to the general class of problems involving interactions between charged particles and metal surfaces, and the attendant charge and/or energy transfer. A sound theoretical understanding of such processes has diverse implications in a wide range of surface physics and chemistry problems such as sputtering, chemisorption, and catalysis. On the other hand, the practical impetus for developing simple and reliable surface H^- ion sources has been provided by the need of such sources in fusion plasma experiments for plasma heating, diagnostics, and acceleration. The conversion of neutral thermal hydrogen beam or proton beam to negative hydrogen ions by a low work function surface has therefore attracted much attention over the past decade.[1-19] Primary beams of various energies have been used, and a host of conversion surfaces has been tested. Conversion efficiencies have been found to be ~60% for backscattering of proton beams having ~10 eV perpendicular energy from cesiated tungsten (110) surfaces (work function ~1.5 eV),[14] and ~1% for backscattering of thermal H atoms from similar surfaces.[17-19] There have been many studies addressing the theory of charge transfer during atom-surface scattering,[20-28] with most of these works employing the Newns–Anderson type Hamiltonian with a time-dependent coupling between the atom and the metal states. A majority of the theoretical treatments to date aims to understand the processes of neutralization and positive ion formation in the scattering of electron positive elements such as Na from a metal surface, though it was recognized that the corresponding H atom-metal surface scattering problem can be treated similarly.[22,24,26]

In the present work we investigate the charge transfer and H^- formation in the scattering of a hydrogen beam from a metal surface, starting from a one-electron Hamiltonian with a prescribed time dependence arising from the motion of the projectile atom along a classical trajectory. The one-

electron density matrix under the action of the time-dependent Hamiltonian evolves in time according to the quantum Liouville equation, whose solution involves the coupling matrix elements between the affinity level of the moving atom with the metal states, which are first explicitly expressed in terms of the potential functions of the ion, the metal, and the interaction between them. These coupling matrix elements are then converted to integrals involving the surface density of states. To facilitate the solution of the Liouville equation a nonlocal self-energy is introduced, whose real and imaginary parts give the time-dependent broadening and shift of the atomic affinity level. In the limit of weak coupling (local interaction) the occupation probability is obtained in closed form. It is argued that for low incident energies, the velocity of the ion must be determined through considerations of conservation of energy, and the usual constant velocity approximation is not valid. The present treatment differs from the usual approach in another important aspect: instead of starting with the Newns–Anderson Hamiltonian with its coupling parameter chosen *a priori*, we evaluate the coupling as the matrix element of the potential functions characterizing the interacting metal–atom system, without making any assumption about its form of time dependence. This formalism is applied to the treatment of hydrogen reflection from W(110) surface, with various Cs coverages, simulated with different surface work functions.

II. FORMULATION

The electron density matrix of the metal–atom system satisfies the Liouville equation

$$i\frac{\partial \rho}{\partial t} = [H, \rho],\qquad (1)$$

where the total one-electron Hamiltonian is given as (atomic units are used throughout this paper, with $\hbar = e = m_e = 1$)

$$H = -\frac{1}{2}\nabla^2 + V_m(x) + V_a[x - R(t)] + V_{im}(x,t).$$

$$(2)$$

Here $V_m(x)$ is the potential confining the metal electrons

inside the metal surface which can be modeled as $V_m(x) = V_0$ for $z > 0$, and $V_m(x) = 0$, for $z < 0$. However, the actual expression of the surface potential is not essential in the development of our theory. It suffices that V_m approaches a constant value (set to zero) deep inside the metal, and likewise it approaches another constant value (set to V_0) far away from the metal. $V_a[x - R(t)]$ is the potential of the H^- ion centered at $R(t)$ which is the position of the center of mass of the atom, determined by classical law of dynamics. The coupling between the affinity level and the ionization level is ignored here, for they are separated by a large energy (~ 13 eV). Furthermore, the ionization level is generally below the bottom of the conduction band, and is therefore unlikely to be involved in the charge exchange process. (It is assumed that the ionization level is occupied throughout the scattering event.) Finally, $V_{im}(x,t)$ represents the interaction of the affinity level with the polarization charge on the metal surface due to the presence of the H^- ion outside the metal. This can be simply expressed as a classical image potential

$$V_{im}(x,t) \to V_{im}(z) = -\frac{1}{4(z+b)}, \quad (3)$$

where b is a screening length, and the minus sign accounts for the fact that the net interaction is attractive (due to the Coulomb interaction of the electron on the affinity level with its own image).

Considered alone, the semi-infinite metal subsystem and the H^- ion subsystem each presents a well defined, solvable eigenvalue problem. Thus, for the semi-infinite metal, we have the eigenvalue ϵ_k, eigenfunction $|k\rangle = u_k(x)$, of the Hamiltonian $H_m = -\frac{1}{2}\nabla^2 + V_m(x)$. Similarly, the atomic Hamiltonian $H_a = \frac{1}{2}\nabla^2 + V_a(x - R)$ has the eigenvalue ϵ_a and eigenfunction $|a\rangle = u_a(x)$. Taking the matrix elements of Eq. (1) between the various states $|a\rangle$ and $|k\rangle$, and employing the overly complete set $|i\rangle, i = 1,2,...N$, with $i \equiv k$ for $i = 1,2,...,N-1$, and $i \equiv a$ for $i = N$, we have (denote $\langle a|\rho|a\rangle = \rho_{aa}$, etc.)

$$i\frac{\partial}{\partial t}\rho_{aa} = \sum_k (V_{ak}\rho_{ka} - V_{ka}\rho_{ak}), \quad (4)$$

$$i\frac{\partial}{\partial t}\rho_{ka} = [\epsilon_k - \epsilon_a(t)]\rho_{ka} + V_{ka}[\rho_{aa} - f(\epsilon_k)], \quad (5)$$

and

$$i\frac{\partial}{\partial t}\rho_{ak} = -[\epsilon_k - \epsilon_a(t)]\rho_{ak} - V_{ak}[\rho_{aa} - f(\epsilon_k)], \quad (6)$$

where $V_{ka} = \langle k|H|a\rangle$, $\epsilon_a(t) = \langle a|H|a\rangle$, and we have assumed that $\rho_{kk} = f(\epsilon_k)$, the equilibrium Fermi–Dirac distribution, and have approximated $\langle k|H|k\rangle$ by ϵ_k. To proceed, we first eliminate the density matrix elements ρ_{ka} and ρ_{ak}. Integrating Eq. (5) we obtain

$$\rho_{ka}(t) = \rho_{ka}(t_0)\exp\left\{-i\int_{t_0}^t d\tau[\epsilon_k - \epsilon_a(\tau)]\right\}$$

$$-i\int_{t_0}^t dt' V_{ka}(t')[\rho_{aa}(t') - f(\epsilon_k)]\exp$$

$$\times\left\{-i\int_{t'}^t dt''[\epsilon_k - \epsilon_a(t'')]\right\}. \quad (7)$$

Similarly, Eq. (6) can be integrated to yield $\rho_{ak}^*(t)$ in terms of ρ_{aa}. These are then inserted in Eq. (4) to yield the integro-differential equation

$$i\frac{\partial}{\partial t}\rho_{aa}(t) = \sum_k \Bigg(V_{ak}(t)\int_{t_0}^t dt' V_{ka}(t')[\rho_{aa}(t')$$

$$- f(\epsilon_k)]\exp\left\{-i\int_{t'}^t dt''[\epsilon_k - \epsilon_a(t'')]\right\}$$

$$+ V_{ka}(t)\int_{t_0}^t dt' V_{ak}(t')[\rho_{aa}(t')$$

$$- f(\epsilon_k)]\exp\left\{i\int_{t'}^t dt''[\epsilon_k - \epsilon_a(t'')]\right\}\Bigg). \quad (8)$$

It is convenient to introduce a nonlocal self-energy[25] through the definition

$$\sum(t,t';t-t') = -i\sum_k \tilde{V}_{ak}(t)\tilde{V}^*_{ak}(t')e^{-i(\epsilon_k - \epsilon_a)(t-t')}, \quad (9)$$

where we have approximated the time-dependent part of $\epsilon_a(t)$ by the image potential, i.e., $\epsilon_a(t) = \epsilon_a + V_{im}[z(t)]$, and have redefined the coupling matrix element as

$$\tilde{V}_{ak}(t) = V_{ak}(t)\exp\left\{i\int_{t_0}^t dt' V_{im}[z(t')]\right\}. \quad (10)$$

Fourier transform of Eq. (9) according to $t-t' \to \omega$ yields

$$\sum(t,t';\omega) = i\sum_k \frac{\tilde{V}_{ak}(t)\tilde{V}^*_{ak}(t')}{\omega - \epsilon_k + \epsilon_a + i0^+}, \quad (11)$$

which leads to a nonlocal broadening of the affinity level as

$$\Delta(t,t';\omega) = \pi\sum_k \tilde{V}_{ak}(t)\tilde{V}^*_{ak}(t')\delta(\omega - \epsilon_k + \epsilon_a). \quad (12)$$

A resonant charge transfer process involves only electronic states of the same energy $[\epsilon_k \simeq \epsilon_a(t)]$. Thus to a first approximation we may replace ϵ_k by $\epsilon_a(t)$ in the Fermi function. This results in a simpler version of Eq. (8):

$$\frac{d}{dt}\rho_{aa}(t) = 2\int_{t_0}^t dt' \Delta(t,t';t-t')\{f[\epsilon_a(t')] - \rho_{aa}(t')\}. \quad (13)$$

Equation (13) is the starting point of evaluating the occupancy of the affinity level. It is obvious that the nonlocal level width of the affinity level plays a central role in the determination of such an occupation probability. As a generalization of the semiclassical probability model,[24] Eq. (13) incorporates all the essential quantum mechanical features of the amplitude model[23] as well. In addition, the intrinsic nonlocality and energy dependence of the level width are embodied in this equation. It is still a difficult task to solve Eq. (13) in general. Numerical solutions can in principle be obtained employing standard techniques. In the limit of weak coupling, however, the level width becomes local in time, $\Delta(t,t';t-t') \to \Delta(t)\delta(t-t')$, it then follows that the occupation probability satisfies a simple "rate" equation of the form

$$\frac{d}{dt}\rho_{aa}(t) = 2\Delta(t)\{f[\epsilon_a(t)] - \rho_{aa}(t)\}, \quad (14)$$

whose solution is readily obtained through a straightforward integration as

$$\rho_{aa}(t) = \rho_{aa}(t_0)\exp\left[-2\int_{t_0}^{t}d\tau\,\Delta(\tau)\right]$$
$$+ 2\int_{t_0}^{t}dt'\,\Delta(t')f[\epsilon_a(t')]$$
$$\times\exp\left[-2\int_{t'}^{t}dt''\,\Delta(t'')\right]. \tag{15}$$

Similar expressions have been derived by a number of authors with various approaches.[20,23-27] The first term on the right-hand side of Eq. (15) describes the decay of the affinity level of an H$^-$ ion already present at t_0, while the second term accounts for the formation of an H$^-$ ion along the trajectory.

It remains to specify the coupling matrix element $\tilde{V}_{ak}(t)$ in order to calculate the occupancy of the affinity level. Such a matrix element is usually given a pressumed form[18,23,25,28] $\tilde{V}_{ak}(t) = \tilde{V}_{ak}\exp(-\gamma t)$, where γ is a parameter characterizing the decay of the coupling strength away from the metal surface. We shall, however, evaluate the coupling matrix element following Easa and Modinos.[27] These authors have shown that the coupling matrix element can be converted to a surface integral at $z = 0$ (taken to be the metal surface) as

$$V_{ka}(t) = \frac{1}{2}\int d^2x\left\{u_a[\mathbf{x}-\mathbf{R}(t)]\frac{\partial}{\partial z}u_k^*(\mathbf{x})\right.$$
$$\left. - u_k^*(\mathbf{x})\frac{\partial}{\partial z}u_a[\mathbf{x}-\mathbf{R}(t)]\right\}_{z=0}. \tag{16}$$

For a metal surface of perfect two-dimensional (2D) crystalline structure, the periodicity of the wave function $u_k(\mathbf{x})$ in the xy plane at $z = 0$ makes it possible to expand it in the two-dimensional (2D) reciprocal lattice vector $\bar{G}$ space:

$$u_k(\mathbf{x}) = \sum_{\bar{G}}u_{\bar{G}k_z}(z)e^{i(\bar{k}+\bar{G})\cdot\bar{x}}, \tag{17}$$

where 2D vectors (in the xy plane) are designated with an overhead bar. The atomic wave function can also be Fourier analyzed

$$u_a(\mathbf{x}) = \sum_{\bar{k}}u_a(\bar{k},z)e^{i\bar{k}\cdot\bar{x}}. \tag{18}$$

Substituting Eqs. (17) and (18) into Eq. (16), we obtain the coupling matrix element

$$V_{ka}(t) = \frac{1}{2}\sum_{\bar{G}}\left\{u_a[\bar{k}+\bar{G},z-Z(t)]\frac{\partial}{\partial z}u_{\bar{G}k_z}^*(z)\right.$$
$$\left. - u_{\bar{G}k_z}^*(z)\frac{\partial}{\partial z}u_a[k+\bar{G},z-Z(t)]\right\}_{z=0}. \tag{19}$$

III. CALCULATIONS AND DISCUSSIONS

In our calculations we shall use for the metal states the plane-wave expansion

$$|k\rangle = A^{1/2}\sum_{\bar{G}}A_{\bar{G}k}\,e^{i(\bar{k}+\bar{G})\cdot\bar{x}-k_z z}, \text{ for } z > 0, \tag{20}$$

where A is a normalization area, $A_{\bar{G}k}$ is an expansion coefficient, and $k_z = [2(V_0-\epsilon)+(\bar{k}+\bar{G})^2]^{1/2}$. To simplify calculation we shall keep the $\bar{G} = 0$ terms only, and the ex-

pansion coefficient in Eq. (20) is absorbed into the normalization constant. For the atomic wave function we employ[26]

$$|a\rangle = \frac{[2\alpha\beta(\alpha+\beta)]^{1/2}}{4\pi(\beta-\alpha)}\left(\frac{e^{-\alpha r}-e^{-\beta r}}{r}\right). \tag{21}$$

with $\alpha = 0.2355$ a.u., $\beta = 0.7858$ a.u. This state has the proper affinity level position at $\epsilon_a = -0.5\alpha^2 = -0.75$ eV, measured from the vacuum level. With these wave functions we can now calculate the coupling matrix element, which is then put in Eq. (12) to evaluate the level broadening. In the evaluation of Eq. (12) we change the sum over k to integrations according to

$$\sum_{\mathbf{k}} \rightarrow \frac{A}{(2\pi)^2}\int d^2k\int d\epsilon\rho(\epsilon,\bar{k}), \tag{22}$$

where $\rho(\epsilon,\bar{k})$ is the 2D surface density of states. This makes it possible for the present formalism to include features associated with surface electronic structures. However, in the following we shall employ the free-electron density of states for a constant step potential

$$\rho(\epsilon,\bar{k}) = -\frac{1}{\pi V_0}\sqrt{2\epsilon - \bar{k}^2}, \tag{23}$$

in order to simplify the ensuing computations.

The above formulation is applied to treat the problem of charge exchange and H$^-$ formation in the scattering of low and intermediate energy hydrogen from a W(110) surface, with various coverages of Cs, simulated by a variable work function ϕ. The calculation, either using the simplified formula [Eq. (15)], or starting from the integro-differential equation [Eq. (14)], is straightforward, except at low incident energies. If the incident energy is the order of a few eV or lower, it is comparable with the binding energy of the H$^-$ ion with the surface. In this case, the constant velocity approximation ($z = vt$, v is the velocity of the projectile atom) is no longer valid,[17-19] and the atomic velocity must be determined from considerations of energy conservation. The potential energy of the H$^-$ ion, which is equal to the energy of the electron on the affinity level $\epsilon_a(z)$, plus the kinetic energy of the moving ion, must be conserved, leading to a z dependent atomic velocity $v(z)$. Such a variable velocity effect is most important for incident energies close to the difference between the work function ϕ and the affinity level $\epsilon_a(z)$, i.e., $\phi - \epsilon_a(z)$. In particular, for incident energy smaller than this value, the kinetic energy of the ion falls to zero at z, in which case the ion will be trapped to the surface. In the zero surface temperature limit the affinity level crosses the Fermi level at a point z_c. For $z < z_c$, the affinity level is in resonance with filled metal states, enabling electron transfer from these states to the affinity level to occur. Once the ion moves outside of z_c ($z > z_c$), the reverse process takes place, i.e., the electron on the affinity level can tunnel back to the metal. Those ions that survive this process at a large distance from the surface contribute to the H$^-$ yield. There is a critical incident energy, corresponding to $\phi - \epsilon_a(z_c)$, which is the minimum potential energy at the crossing point z_c. Below this energy, no ion can escape the binding of the surface. Of course, at finite surface temperature this cutoff will be smeared out to encompass a finite width $\sim k_B T$ about the Fermi level. Smearing also occurs as a result of the finite

lelvel width at z.

In our calculation we take the Fermi energy to be 8 eV. The constant potential barrier of the metal surface V_0 is given as the sum of the Fermi energy and the work function. Two specific cases are considered here: A bare W(110) surface with work function $\phi = 5.25$ eV, and a W(110) surface covered with half of a monolayer of Cs, with a work function of 1.45 eV. In addition to the Fermi energy and the work function, the screening length that enters the surface image potential is another important quantity which directly influences the calculated H⁻ yield. For a free-electron like metal surface this can be taken as the Thomas–Fermi screening length. However, for a metal surface with adsorbate coverage such a simple theory of screening does not seem to be valid. In our numerical calculation we employ the value $b = 0.81$ a.u. for the bare tungsten surface,[27] and $b = 3.2$ a.u. for the cesium covered tungsten surface.[26]

Numerical results obtained with Eq. (15) are presented in the figures. We first examine the distance dependence of the level width of the affinity level. Such dependence for the two surface work functions is shown in Fig. 1. The typical exponential dependence of the level width on the distance from the surface is obvious, except at very small distances. In the latter case there is some uncertainty in the actual form of the interaction potential between the affinity level and the metal surface. An image description at such close distances can no longer be trusted. A much stronger interaction (chemical reaction) is to be expected between the atom and the surface. We have not attempted to incorporate this region into our consideration. Instead, we shall assume that the turning point (z_0) is outside this region (taken to be $z_0 = 2$ a.u.), and that the occupation probability takes its equilibrium value at z_0. In Fig. 2 we plot the H⁻ yield as a function of the incident energy for a surface work function of 5.25 eV. For comparison we also show here the result of employing the constant velocity approximation. As expected, the difference arises mainly for energy below ~4 eV, where our theory predicts a vanishing yield, while the constant velocity approximation leads to a finite yield. The calculated maximum yield of about 1% is in agreement with previous predictions.[24] Results for the tungsten surface covered with cesium (work
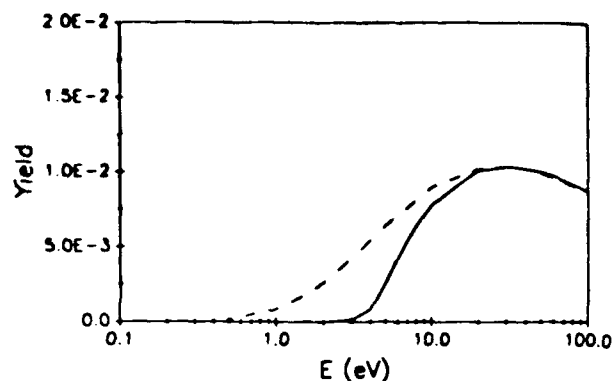
FIG. 2. H⁻ yield as a function of incident energy on a bare tungsten surface. Solid line: variable velocity; Dotted line: constant velocity.

function 1.45 eV) are depicted in Fig. 3. Again, the differnce of employing the constant velocity approximation from that of a variable velocity calculation is most significant for energies below about 0.7 eV: the former leads to a yield of ~40%, while the latter gives zero. The maximum (about 60%) yield obtains for both curves at a few eV, in agreement with both earlier predictions[24] and experiments.[6–14] Finally, we exhibit the effect of the target temperature on the H⁻ yield in Fig. 4, where the yield as a function of incident energy for different surface temperatures are plotted.

To summarize, we have developed a theory of charge transfer in the reflection of hydrogen atoms from a metal surface based on an analysis of the time development of the electron density matrix. Our numerical examples using a simple version of the theory showed good agreement with other theories and existing experimental data. We have not attempted to incorporate fully all the features of the theory in our sample calculation, such as the surface electronic structure, realistic metal band structures, as well as the nonlocal interaction of the atom with the metal surface. We believe that in order to achieve a quantitative understanding of the charge transfer process such complications are unavoidable. That is to say the integro-differential equation (Eq. 13) must be solved without the various approximations made in this note. Finally, it should be pointed out that the screening length in the image potential is still a free parameter at the present level of theoretical understanding, especially for ad-
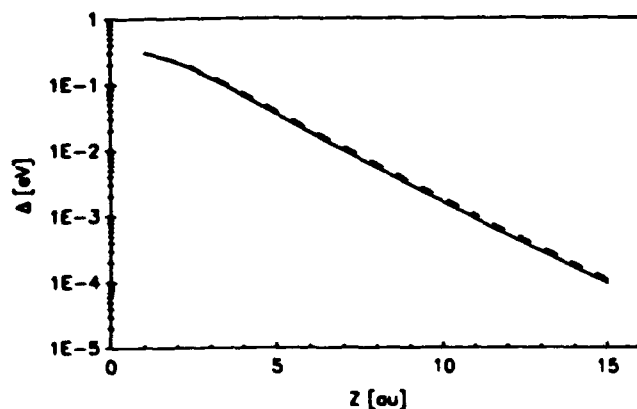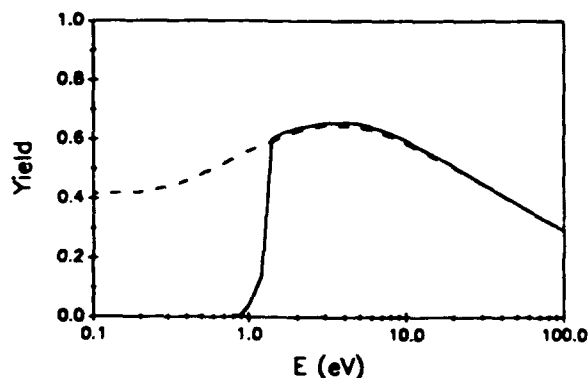

FIG. 1. Affinity level width of H⁻ as a function of the distance from the metal surface. Solid line: bare tungsten surface; Dotted line: cesium covered tungsten surface.

FIG. 3. H⁻ yield as a function of incident energy on a cesium covered tungsten surface. Solid line: variable velocity; Dotted line: constant velocity.
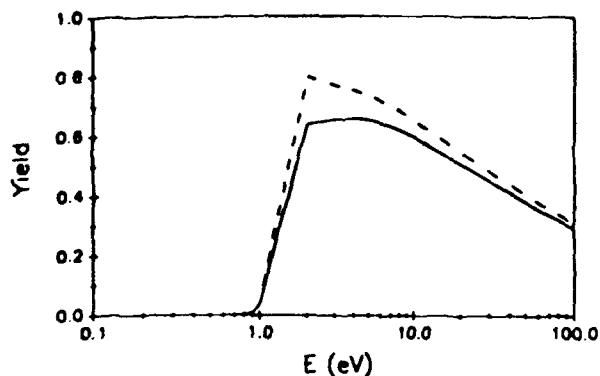
FIG. 4. H^- yield as a function of incident energy on a cesium covered tungsten surface for different surface temperatures. Solid line: $T = 500$ K; Dotted line: $T = 0$ K.

sorbate covered metal surfaces. This certainly leaves much to be desired. A more satisfactory theory should perhaps generate such screening characteristics from a self-consistent treatment of the many-electron system, incorporating the necessary modifications brought about by the presence of the adsorbates.

ACKNOWLEDGMENTS

[1]M. Seidl and A. Pargellis, Phys. Rev. B **26**, 1 (1982).
[2]J. L. Lopes, J. A. Greer, and M. Seidl, J. Appl. Phys. **60**, 17 (1986).
[3]C. F. A. van Os, P. W. van Amersfoort, and J. Los, J. Appl. Phys. **64**, 3863 (1988).
[4]K. N. Leung and K. W. Ehlers, J. Appl. Phys. **52**, 3905 (1982)
[5]K. N. Leung and K. W. Ehlers, Rev. Sci. Instrum. **53**, 803 (1982)
[6]W. Eckstein, H. Verbeek, and R. S. Bhattacharya, Surf. Sci. **99**, 356 (1980).
[7]J. R. Hiskes and P. J. Schneider, Phys. Rev. B **23**, 949 (1981).
[8]J. N. M. van Wunnik, J. J. C. Geerlings, and J. Los, Surf. Sci. **131**, 1 (1983).
[9]J. N. M. van Wunnik, J. J. C. Geerlings, E. H. A. Granneman, and J. Los, Surf. Sci. **131**, 17 (1983).
[10]P. J. M. van Bommel, J. J. C. Geerlings, J. N. M. van Wunnik, P. Massmann, E. H. A. Granneman, and J. Los, J. Appl. Phys. **54**, 5676 (1983).
[11]P. J. Schneider, K. H. Berkner, W. G. Graham, R. V. Pyle, and J. W. Stearns, Phys. Rev. B **23**, 941 (1981).
[12]P. W. van Amersfoort, J. J. C. Geerlings, L. F. T. Kwakman, A. Hershcovitch, E. H. A. Granneman, and J. Los, J. Appl. Phys. **58**, 3566 (1985).
[13]P. W. Amersfoort, J. J. C. Geerlings, R. Rodink, E. H. A. Granneman, and J. Los, J. Appl. Phys. **59**, 241 (1986).
[14]J. J. C. Geerlings, P. W. van Amersfoort, L. F. T. Kwakman, E. H. A. Granneman, J. Los, and J. P. Gauyacq, Surf. Sci. **157**, 151 (1985).
[15]W. G. Graham, Phys. Lett. A **73**, 186 (1979).
[16]A. Pargellis and M. Seidl, Phys. Rev. B **25**, 4356 (1982).
[17]M. Seidl, W. E. Carr, J. L. Lopes, and S. T. Melnychuk, *Proceedings of the Third European Workshop*, edited by H. Hopman and W. van Amersfoort, (FOM-Institute for Atomic and Molecular Physics, Amsterdam, the Netherlands, 1988).
[18]M. Seidl, W. E. Carr, S. T. Melnychuk, A. E. Souzis, J. Isenberg, and H. Huang, Conference Proceedings, SPIE, **1061**, 547 (1989).
[19]S. T. Melnychuk, M. Seidl, W. Carr, J. Isenberg, and J. Lopes, J. Vac. Sci. Technol. A **7**, 2127 (1989).
[20]A. Blandin, A. Nourtier, and D. Hone, J. Phys. **37**, 369 (1976).
[21]J. R. Hiskes, J. Phys. **40**, 179 (1979).
[22]E. G. Overbosch, B. Rasser, A. D. Tenner, and J. Los, Surf. Sci. **92**, 310 (1980).
[23]R. Brako and D. M. Newns, Surf. Sci. **108**, 253 (1981).
[24]B. Rasser, J. N. M. van Wunnik, and J. Los, Surf. Sci. **118**, 697 (1982).
[25]N. D. Lang, Phys. Rev. B **27**, 2019 (1983).
[26]J. P. Gauyacq and J. J. C. Geerlings, Surf. Sci. **182**, 245 (1987).
[27]S. I. Easa and A. Modinos, Surf. Sci. **183**, 531 (1987).
[28]A. T. Dorsey, K. W. Jocobsen, Z. H. Levine, and J. W. Wilkins, Phys. Rev. B **40**, 3417 (1989).

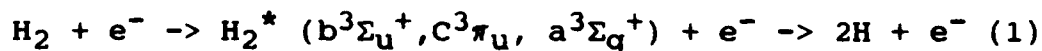# SURFACE PRODUCTION OF H⁻ IONS BY HYPERTHERMAL HYDROGEN ATOMS

Brian S. Lee and M. Seidl, Department of Physics and

Engineering Physics, Stevens Institute of Technology,

Hoboken, NJ 07030

ABSTRACT

Hyperthermal atomic hydrogen of energy in the range of
1-10 eV has been produced by electron impact dissociation in
a CW 2.45 GHz microwave ECR discharge using a Lisitano-Coil.
The flux and the energy of the hydrogen atoms have been
measured by negative surface ionization of the atoms
backscattered from pure and cesiated metal surfaces. The
temperature of the H⁻ ions has been estimated by measuring
the parallel energy spread of the H⁻ ions leaving the
surface in a uniform magnetic field. A temperature of 4-5 eV
has been obtained. A hyperthermal atomic hydrogen flux
density equivalent to more than 0.5 A/cm^2 has been produced
for 420 watts discharge power under CW condition. The
hyperthermal hydrogen atoms constitute a major source of
primary particles for surface production of H⁻ ions. These
hydrogen atoms can be directed onto an external converter
located outside the discharge. This opens up new
possibilities for H⁻ ion source design.

1

Hydrogen and deuterium negative ion sources have received much attention during the past few decades. Such sources may be used for the production of intense neutral beams for plasma heating, current drive and diagnostic purposes in Tokamaks. Negative ion beams may also be used in tandem and cyclotron accelerators and synchrotrons.[1,2]

It is well known that H^- ions can be produced by backscattering protons or neutral atoms from low work function surfaces.[3,4] Previous experiments had been done with protons[5,6] or thermal hydrogen atoms.[7,8] In this work, we have investigated the surface production of H- ions by backscattering hyperthermal hydrogen atoms produced in a discharge by electron impact dissociation. The following two reactions are the major source of hyperthermal hydrogen atoms in a plasma;[9]

$$H_2 + e^- \rightarrow H_2^* \ (b^3\Sigma_u^+, c^3\pi_u, \ a^3\Sigma_g^+) + e^- \rightarrow 2H + e^- \quad (1)$$

$$H_2^+ + e^- \rightarrow H_2^{+*} \ (2p\sigma_u) + e^- \rightarrow H^+ + H + e^-. \quad (2)$$

Electron impact excitation of the ground state molecule $(X^1\Sigma_g^+)$ to the lowest triplet state $(b^3\Sigma_u^+)$ has been known to lead to the production of a pair of ground state atomic hydrogens with minimum translational energy of 2.2 eV. The electronic excitation of the ground state H_2^+ ion results in dissociation to a proton and a hydrogen atom with even higher energy (>5 eV) under similar conditions. The reaction rates($<\sigma_i v_i>$) for the above processes were

2

calculated for electrons with a Maxwellian energy distribution.[10,11]

We have built a source of hyperthermal hydrogen atoms using a CW 2.45 GHz Lisitano-Coil[12] Microwave Electron Cyclotron Resonance hydrogen discharge. The structure consists of an interdigital transmission line slotted on a 3.5 cm diameter copper tube which is surrounded by an outer coaxial cylinder. Microwave power is fed by a vacuum sealed coaxial transmission line. The slotted-line structure is a broad band cavity supporting slow-waves which interact strongly with plasma electrons.[13]

The experiment consists of a vacuum chamber pumped with a 1100 l/s turbo-pump (base pressure 1.5×10^{-8} Torr), 8 modules of water-cooled electromagnets (10" ID, 24" OD), a CW 500 watt variable power microwave source, and a gas flow meter along with a baratron. A detailed description of the experiment will be given elsewhere.

The chamber is divided into two regions, the plasma region and the analysis region which includes the converter (Fig.1). The plasma is contained in a fused quartz tube. The hyperthermal hydrogen atoms produced in the discharge region effuse through an aperture (0.4 cm I.D. by 1.4 cm long) in the fused quartz plasma chamber , and are scattered from a converter surface consisting of a clean or cesiated

3

molybdenum. The work function of the cesiated Mo surface was independently obtained from photoelectric threshold measurement with a tunable light source. Work functions as low as 1.55 eV were obtained using a Cs dispenser. Although the work function was not measured during the experiment, the converter coverage was optimized for maximum H^- ion signal. The Mo converter was chemically cleaned and then thermally heated in vacuum to 1000 $^{\circ}$C for 20 minutes prior to the experiment. Two sets of electrostatic deflector plates are installed immediately after the exit aperture to remove the charged particles (e^-, H^+, H_2^+, H_3^+) which may diffuse across the magnetic field. The H^- ions produced on the converter surface are accelerated in a planar diode with a 1mm gap. The anode is a fine mesh and the cathode is the converter made of a spring loaded Mo ribbon, 1 cm wide and 10 cm long. The fully accelerated H^- ions gyrate across the homogeneous magnetic field (~875 Gauss) with Larmor radius and pass through a narrow slit aperture (0.05 cm wide and 1 cm long) mounted directly onto the Faraday Cup (Fig.1).

As shown in Fig.2, H^- ions with the same parallel energy (parallel to the converter surface) are geometrically focussed, and ions with different parallel energy are defocussed in the aperture plane. The slit width gives an energy resolution of $\triangle E < 0.4$ eV. The beam spread width in the slit, W, was calculated based on the orbital equation of

charged particles in a homogeneous magnetic field including ExB drift in the acceleration region, which is given by

$$W \approx 2r_L \sin(\theta), \qquad\qquad (3)$$

where $r_L = 144\sqrt{U}/B$, $\theta \approx \arctan\sqrt{(E_p(eV)/U(eV))}$. E_p is the parallel energy of the H$^-$ ions (parallel to the converter surface) ,and U is the extraction energy of H- ions. For small θ, $W \approx 2 \times 144 \sqrt{(E_p(eV))}/B$ independent of extraction energy. Since the beam spread is nearly independent of the extraction energy, one can obtain a distribution in parallel energy by scanning the extraction energy and holding the Faraday Cup with the slit in a fixed position. Fig.3 shows the definition of the angles and relationship of H$^-$ ion exit angle to parallel energy.

The H$^-$ ion current measured directly from the converter has been compared with the Faraday cup current integrated over the distribution. Here, the secondary and exo-electrons have been suppressed by the strong magnetic field (~ 875 Gauss). This was confirmed by photo-electric current and thermionic emission current measurements. The measured total H$^-$ ion current leaving the cesiated surface, $I_t(H^-)$, for 420 watts microwave power and 9 sccm hydrogen gas flow rate (3×10^{-4} Torr chamber pressure) is 0.125 mA. If the converter was located on the wall of the quartz tube, the corresponding H$^-$ ion current density would be $J(H^-) = 127$ mA/cm^2. This calculation is based on the following relationship:

5

$$J(H^-) \approx I_t(H^-) x (\pi/\Omega)/A, \tag{4}$$

where Ω is the solid angle subtended by the converter at the exit aperture (0.025 steradian), and A is the area of the exit aperture (0.125 cm^2). In this calculation, we have ignored the contribution of the tube wall, since the solid angle subtended by the converter, Ω, is smaller than the geometric solid angle of the tube.[14] The hyperthermal atomic hydrogen flux density can be estimated by knowing the value of the H^- ion yield. The total H^- ion yield can be expressed by

$$<Y(kT)> = \int_o^\infty F(E)Y_i(E)dE. \tag{5}$$

For a Maxwellian distribution,

$$<Y(kT)> = (2/\pi)(1/kT)^{3/2} \int_o^\infty E^{1/2} Y_i(E)e^{-E/kT}dE, \tag{6}$$

where $F(E)$ is the energy distribution of the incident atomic hydrogen beam with temperature T, and $Y_i(E)$ is the H^- ion yield as a function of the perpendicular energy of the backscattered atom. Therefore, the total H^- ion yield is the convolution of the energy distribution and the H^- ion yield. Fig.4 shows the calculated total H^- ion yield for the temperature range of 0.1 eV - 10 eV, using the theoretical yield $Y_i(E)$ calculated by Cui[15] for a work function of 1.45 eV. This yield curve is in excellent agreement with the experimental results for backscattering thermal hydrogen atoms.[8] From this curve we can estimate that the total H^- ion yield is about 25 % for a temperature of 5 eV. This gives a flux density of 0.5 A/cm^2 equivalent corresponding

to hyperthermal hydrogen atoms impinging onto the quartz tube wall with energy exceeding E_{min} (~1 eV).

The estimated temperature of 5 eV follows from measurements of parallel energy distribution. Fig.5 shows typical data for the H⁻ ion signal passing through the slit as a function of the parallel energy, E_p in eV, for the clean polycrystalline Mo and for the cesiated Mo converter. Here, only the data for low power case is shown due to the space charge spread. For high microwave power and cesiated converter surface, the H⁻ ion current density is high enough to cause space charge spread of the beam which redistributes the momentum components of the H⁻ ions along their trajectories. As the surface gets cesiated (work function gets lower), the H⁻ ion current increases by 2-3 orders of magnitude. The scattering angle can be directly converted to the parallel energy using the relationship,

$$E_p(eV)=E \tan^2\theta, \tag{6}$$

where E(eV) is the total energy of the H⁻ ion. The tails of the H⁻ ion parallel energy distribution carry the information of maximum atom energy (~10 eV) since an individual atom may experience 'local specular reflection' with small energy loss. The shape of the parallel energy distribution of the H⁻ ions closely follows a Maxwellian distribution with an average temperature of 4-5 eV.

7

It was shown previously that atomic hydrogen becomes the dominant neutral component as the input power to the discharge becomes larger.[10,16] Spectroscopic measurement of temperature and density in the Los Alamos Penning surface-plasma source[17] shows that a large fraction of the hydrogen is atomic hydrogen (n_{HO}~5x10^14 cm^{-3}, ~30% dissociation rate) with a temperature exceeding 1 eV. This corresponds to very large atomic hydrogen flux density of the order of 100 Amps/cm². Historically atomic hydrogen has been treated as a detrimental particle in H^- ion sources due to its large stripping cross-section. However, in surface conversion sources, a significant fraction of H^- ions can be produced by backscattered hyperthermal hydrogen atoms.

We have produced hyperthermal atomic hydrogen in a discharge. The flux and the energy of the hydrogen atoms was measured by negative surface ionization of the backscattered atoms. A large hyperthermal atomic hydrogen flux density equivalent to more than 0.5 A/cm^2 has been generated. The hyperthermal hydrogen atoms can be directed onto an external converter located outside the discharge in which the converter can be independently controlled to optimize the operating conditions without being effected by the plasma. This opens up new possibilities for H^- ion source design.[18] Further study is required towards a better understanding of the production and loss mechanism of hyperthermal hydrogen atoms in a discharge. Specifically, more data are needed on

reactive collision processes, and on particle/energy
reflection from various surfaces.

9

FIGURE CAPTIONS

Fig.1.   Experimental apparatus. The system is embedded in a
         uniform magnetic field B (~875 Gauss) generated by 8
         modules of electromagnets (not shown).

Fig.2.   H- ion trajectories. H- ions with the same
         scattering angle starting from any point on the
         converter surface (0.5 cm wide) are focussed in the
         aperture plane. H- ions with different angle are
         defocused. The beam spread width, W, for a 10°
         scattering angle is 0.89 cm for 875 Gauss magnetic
         field..

Fig.3.   Sign convention for angles (a), and relationship of
         parallel energy E_p and scattering angle θ (b). θ_s is
         the angle measured by magnetic spectroscopy, θ_d is
         ExB drift angle in a planar diode with 1 mm gap.

Fig.4.   Total H^- ion yield, $<Y(kT)>$, as a function of H^- ion
         temperature. The values for $Y_i(E)$ have been taken
         from Cui (Ref.14). Open circles are the experimental
         values from Ref.8 for Cs/Mo converter.

Fig.5.   H- ion current as a function of the parallel energy
         for cesiated (filled circles) and for uncesiated
         clean Mo metal surface (open circles). The H- ion

current passing through the narrow slit (0.05 cm wide and 1 cm long) is measured by a Faraday Cup. The solid angle of the converter from the atom exit aperture is 0.025 steradian.

REFERENCES

1. K.H. Berkner, R.V. Pyle, and J.W. Stearns, Nucl. Fusion 15, 249 (1975).

2. *Production and Neutralization of Negative Ions and Beams*, Fourth Int. Symposium, Brookhaven N.Y., (Ed. Alessi, J.A.), AIP Conf. Proc. No. 158 (1988).

3. B. Rasser, J.N.M. van Wunnik ,and J. Los, Surf. Sci. 118, 697 (1982).

4. J.R. Hiskes and P.J. Schneider, Phys. Rev. B 23, 949 (1981).

5. P.W. van Amersfoort, J.J.C. Geerlings, L. F. Tz. Kwakman , E.H.A. Graneman ,and J. Los, J. Appl. Phys. 58, 3556 (1985).

6. J.J.C. Geerlings, P.W. Van Amersfoort, L.F.Tz. Kwakman, E.H.A. Granneman, J. Los, and J.P. Gauyacq, Surf. Sci. 157, 151 (1985).

7. W.G. Graham, Phys. Lett. 73A, 186 (1979).

8. S.T. Melnychuk, and M. Seidl, J. Vac. Sci. Technol. A9(3), 1650 (1991).

9. H.S.W.Massey, in *Electronic and Ionic Impact Phenomena*, vol.2 (Oxford Univ. Press, GB, 1969) Chap.13, p877.

10. C.F. Chan, C.F. Burrell, and W.S. Cooper, J. Appl. Phys.54(11), 6119 (1983).

11. O. Fukumasa, R. Itatani, and S. Saeki, J. Phys. D: Appl. Phys. 18, 2433 (1985).

12. G. Lisitano, Appl. Phys. Lett. 16(3), 122 (1970).

13. T.H. Stix, *The Theory of Plasma Waves* (McGrow-Hill, N.Y., 1962).

14. G. Scoles, Atomic and Molecular Beam Methods, Vol. 1 (Oxford Univ. Press, N.Y., 1988), p.88.

15. H.L. Cui, J. Vac. Sci. Technol. A9, 1823 (1991).

16. M. Bacal, et.al., Proc. of the Third European Workshop on *Production and Application of Light Negative Ions* (Netherlands, 1988).

17. H.V. Smith, et.al., Rev. Sci. Instrum. 61, 2378 (1990).

18. M. Seidl, S.T. Melnychuk, S.W. Lee, and W. Carr, in AIP Proc. No.210, *Production and Neutralization of Negative Ions and Beams*, Brookhaven, N.Y. 1990, p.776.

⊗ X $\vec{B}$

WATER COOLED OUTER TUBE

QUARTZ TUBE

LISITANO-COIL

COLLIMATOR SLITS

SHIELDING BOX

FARADAY CUP

DEFLECTOR PLATES

SHUTTER

H^0 H^-

Cs DISPENSER

H^0

BEAM APERTURE

Cs

ANODE MESH

Mo CATHODE
(CONVERTER)
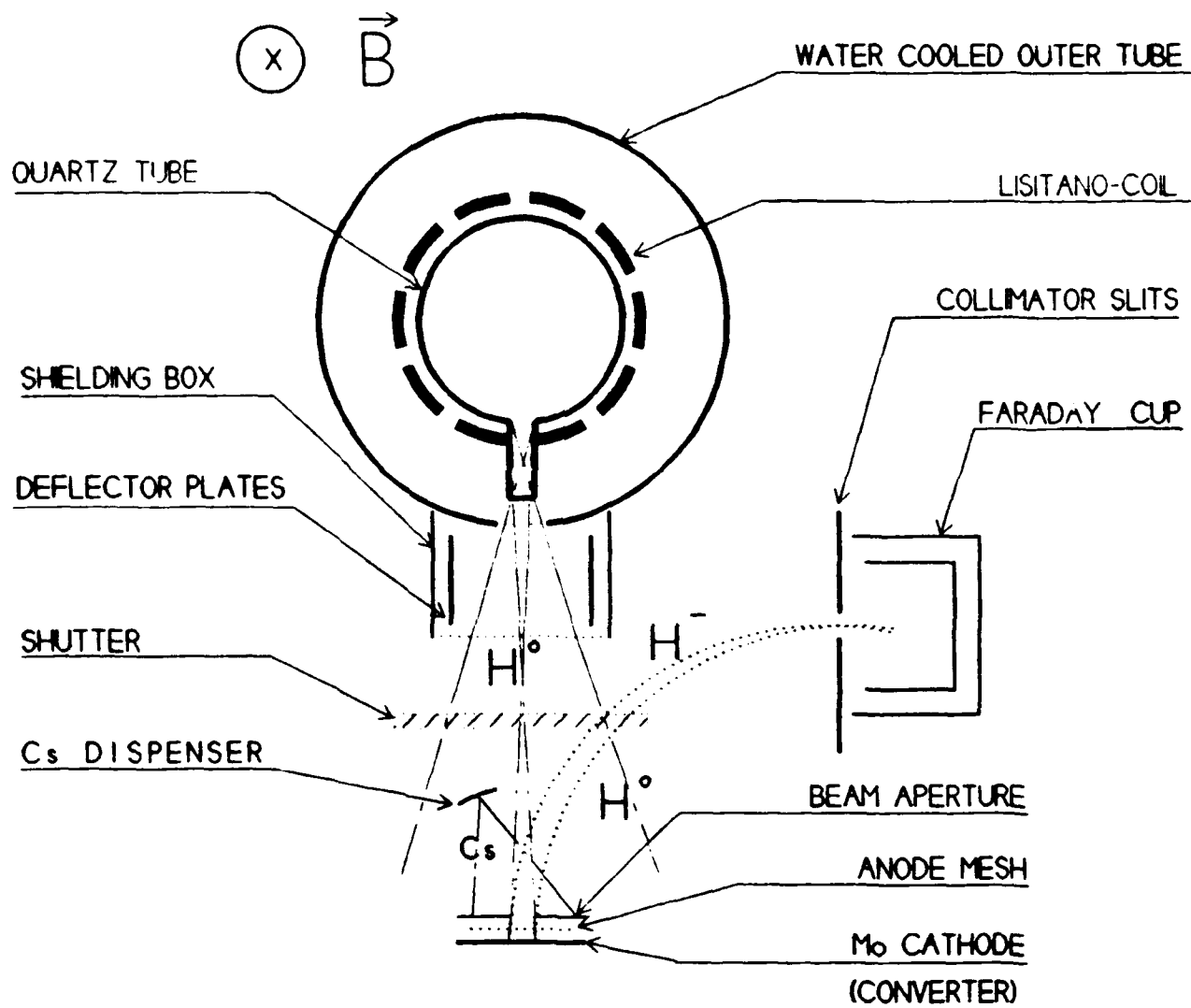
Fig 1

$\theta = 10°$
$\theta = 0°$
$\theta = -10°$

B = 875 Gauss
E = 240 Volts

H⁻

W

⊗ $\vec{B}$

APERTURE

ANODE

CATHODE

10 mm
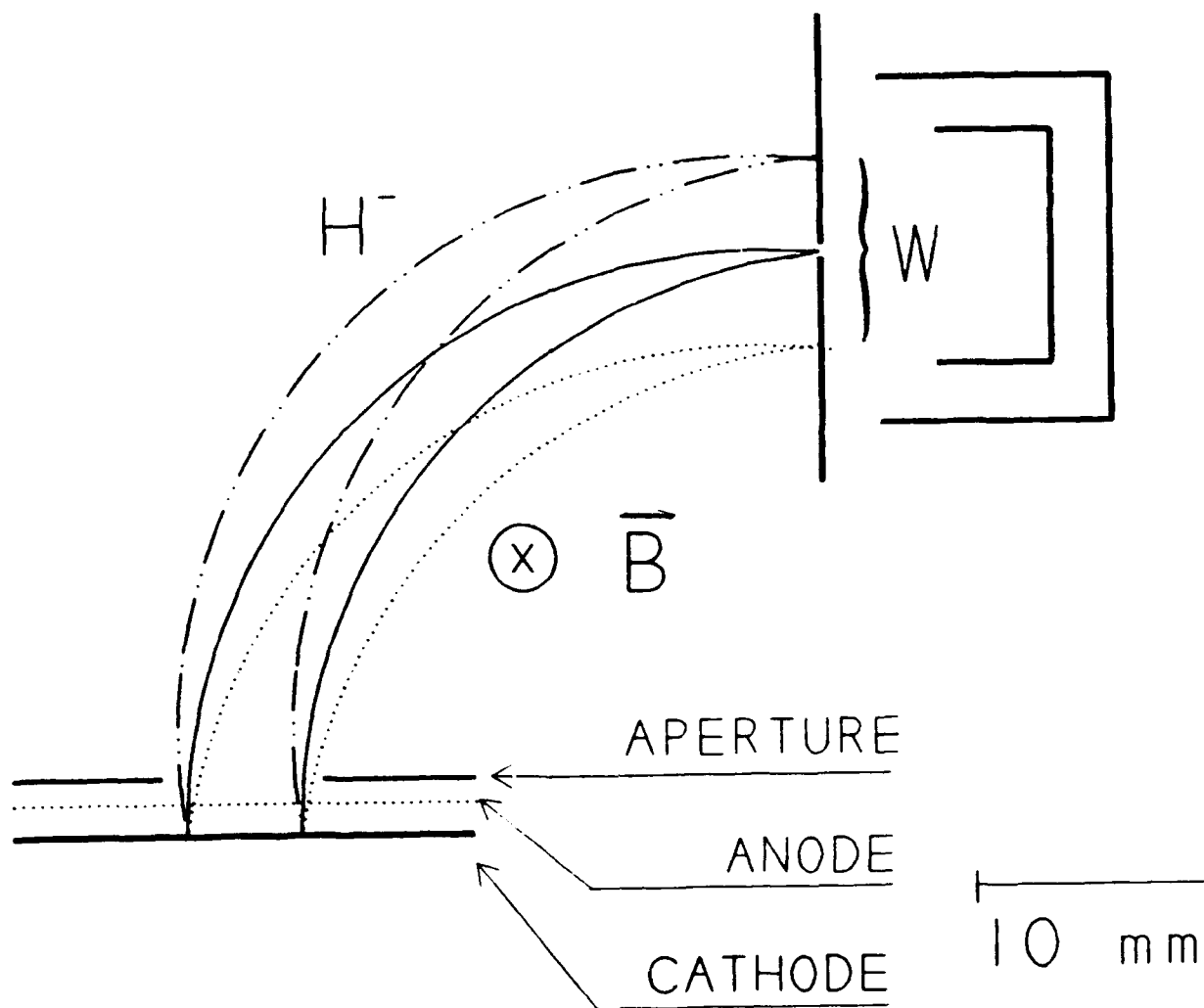
Fig. 2

$$\text{Tan } \theta = \frac{V_p}{V_n} = \sqrt{E_p / U}$$

$$\theta = \theta_s - |\theta_d|$$

$$E_p = \frac{1}{2} m V_p^2$$
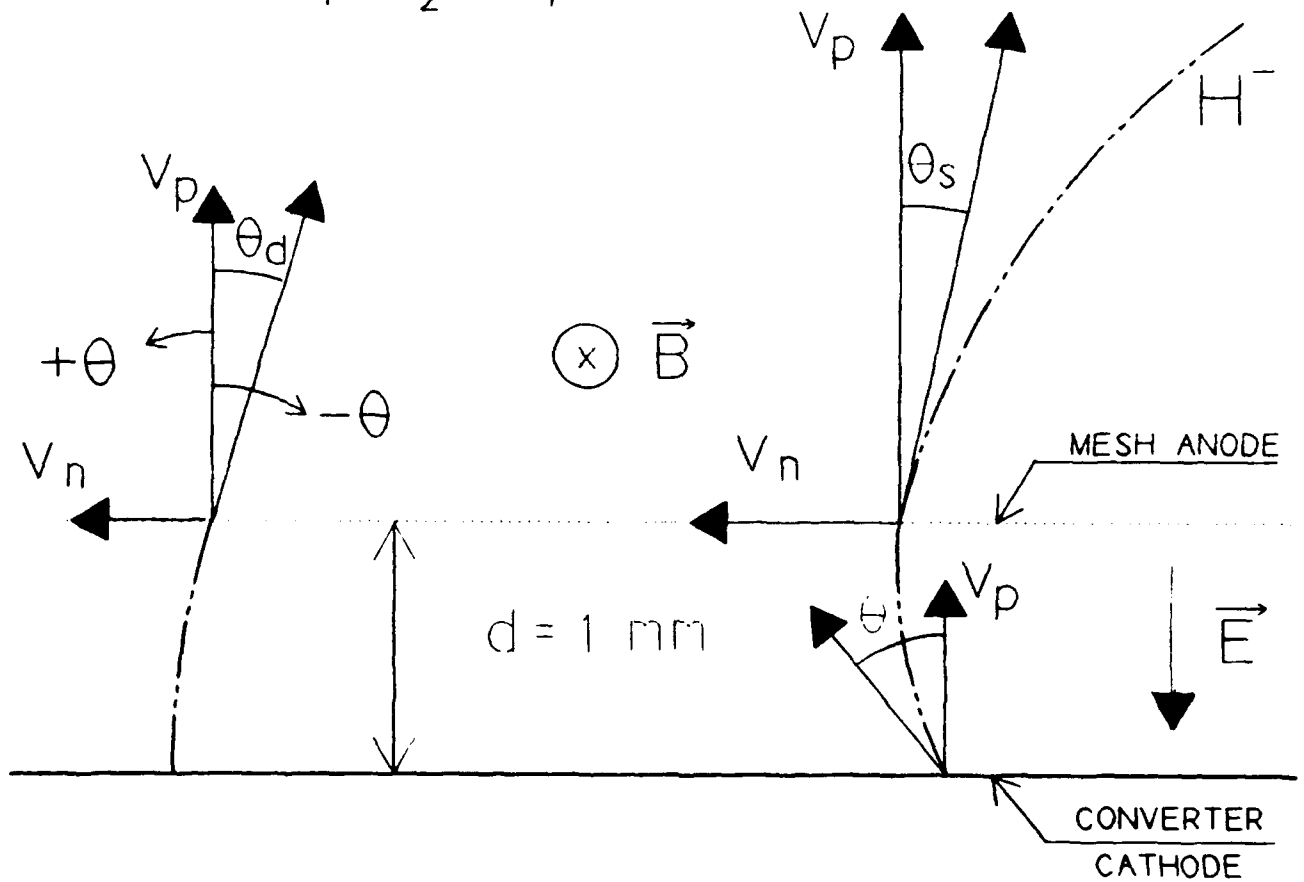
Fig. 3
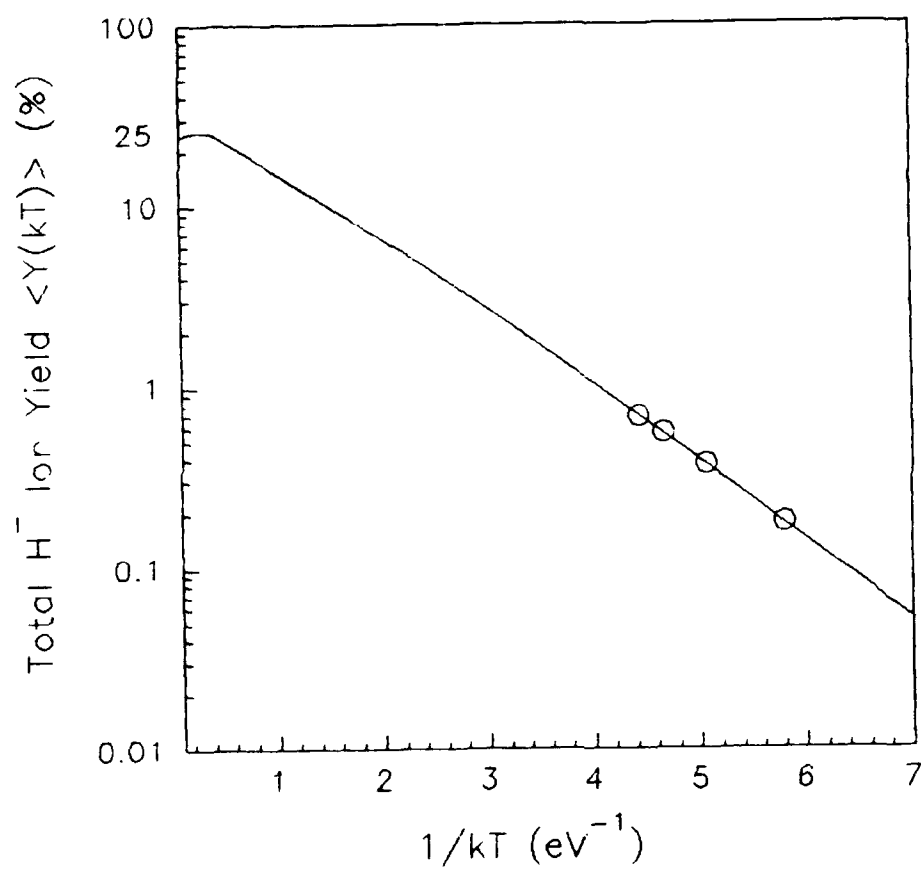
Fig. 4
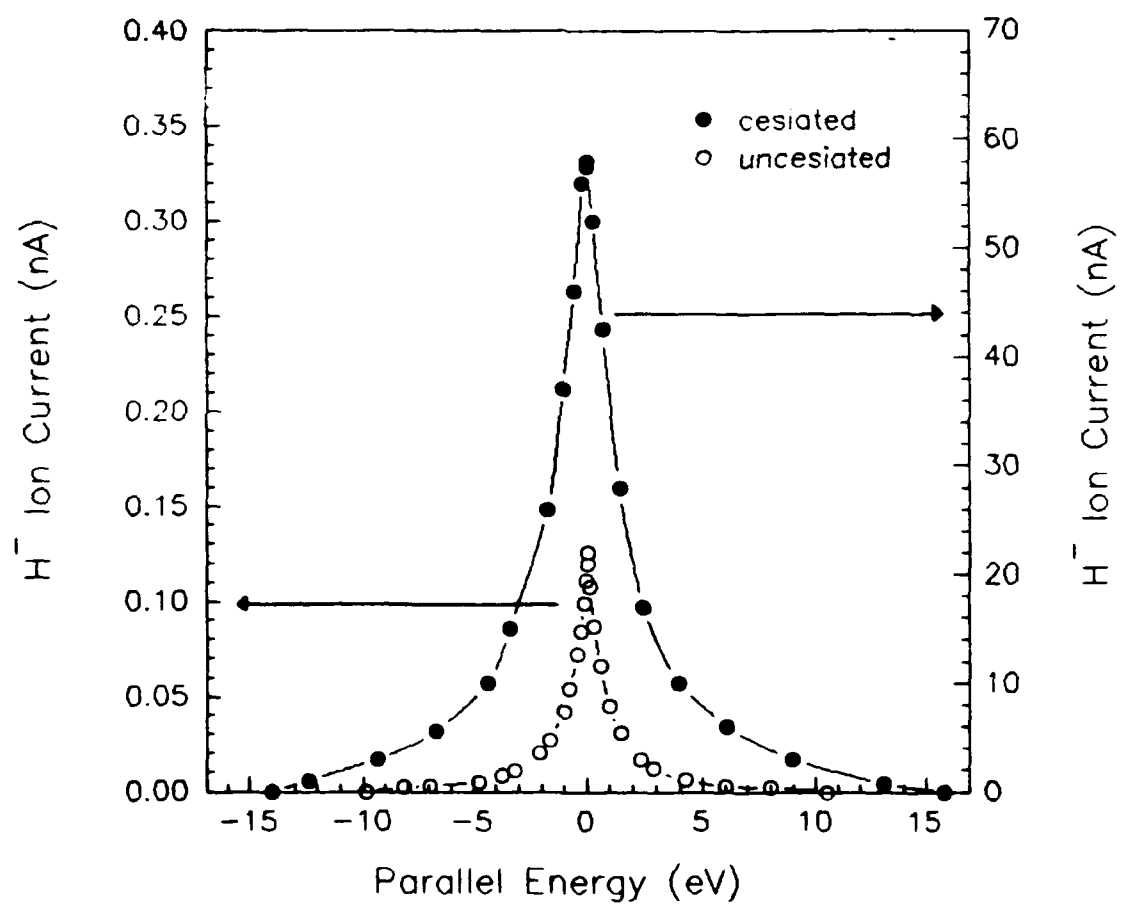
Fig. 5.

Source of Low Energy Hydrogen Ions for Measuring Electron Transfer in Surface Scattering Experiments

J. D. Isenberg, H. J. Kwon, M. Seidl

Department of Physics and Engineering Physics

Stevens Institute of Technology, Hoboken, New Jersey 07030

Abstract

We present the design and performance of a beamline which is the source of 5 - 50 eV protons for surface scattering experiments. The beamline also incorporates a collector for measuring total secondary ion and electron yields. The beam forming optics are built around a commercially available gas discharge ion gun and produce a mass selected, energy filtered beam. Results of computer ray tracing are included to illustrate the operation of the beam optics. Tests have produced 50 pA proton beams 3.5 mm wide at 5 eV with an energy spread of about 1 eV.

1. INTRODUCTION

An ion source has been developed as part of an apparatus for measuring electron transfer in low energy (5-50 eV) hydrogen ion scattering from low work function surfaces at normal incidence. The current design incorporates both the primary beam optics and the secondary ion collector.

Previous electron transfer experiments have used either thermal energy atomic beam sources[1,2] or high energy ion beams striking the target at grazing angles of incidence[3]. Ions striking the target undergo Auger neutralization and scattering. A fraction of the back scattered neutral atoms are negatively ionized through resonant charge exchange.[4]

In the atomic beam type of experiment, the incident particles are neutral hydrogen atoms produced by thermal dissociation in an oven type source and have a Maxwellian energy distribution with a temperature of about 0.2 eV. Since the primary particles are neutral the secondaries can be extracted by applying an electric field. The incident flux cannot be measured directly but must be deduced from gas flow or thermal flux measurements.

In the grazing incidence type experiment, a known flux of protons $\Phi(H+)$ with kinetic energy of order 1 keV strike the target at an oblique angle such that the normal component of the kinetic energy is small. Theory indicates that only the normal component of the incident proton energy is important for electron transfer[5]. The H^- flux $\Phi(H^-)$ and the atomic flux $\Phi(H^\circ)$ scattered at a given angle are measured independently to determine the charged fraction in the scattered beam. The total yield $\Phi(H^-)/\Phi(H+)$ has been measured for cesiated tungsten (110) by van Wunnik et al, but

for 100 - 2000 proton energies and incident angles greater than 70° with respect to the target normal.[6]

To date no experiment has directly measured the total yield, $\Phi(H^-)/\Phi(H+)$, for protons which strike the converter surface at normal incidence and low energy. In such an experiment all backscattered secondary ions must be collected. The ideal proton bean for this experiment would have an energy less than 50 eV and a spread in energy of 1 eV or less.

2. DESCRIPTION OF THE EXPERIMENT

The experiment is installed in a spherical UHV chamber pumped by turbo-molecular and ion pumps. The base pressure is 10^{-10} torr. In the low energy ion source (figure 1) the ion beam produced by an ion gun is mass separated by a Wien filter. The mass selected beam is collimated by an einzel lens (electrodes 1,2,3 in figure 1),decelerated and focused by a four cylinder lens (electrodes 3,4,5,6) into a Bessel box energy filter (electrodes 6,7,8). The energy selected beam is focused onto the target by an einzel lens (electrodes 8,9,10) through an aperture in the collector (electrode 11) and strike the target near normal incidence.

Secondary ions and electrons are backscattered into the collector. A variable magnetic field in the region of the target perpendicular to the beam axis deflects the electrons back to the target. The current measured at the target (I_{tar}) is equal to the sum of the currents due to protons striking it and negative ions and electrons leaving it. Since the collector current (I_{coll}) is the total secondary current, the proton current is just ($I_{tar} - I_{coll}$) and the H$^-$ and electron yields can be determined directly from I_{tar} and I_{coll} measurements taken with the magnetic field on and off.

Two ion ray tracing programs, SIMION[7] and EGUN[8], were used to evaluate the design of the ion optics. Both calculate the electric field for a given array of electrodes by iteratively solving the Laplace equation with the electrode potentials as boundary conditions. The ion trajectories are then calculated from the fields and initial conditions. EGUN simulates space charge forces by solving Poisson's equation for the charge in the beam. This solution is added to the solution due to the electrodes and the trajectories recalculated. Both programs were used to model the Beamline from the middle of the field free region following the Wien filter. For initial conditions it was assumed that the beam from the Wien filter is monoenergetic, collimated, and has a diameter of 3mm defined by the exit aperture of the Wien filter.

Ion trajectories were first plotted with SIMION (figure 2). The electrode voltages were adjusted to optimize the beam to the target. The optimized voltages were then used in EGUN to compare the results and check the effects of space charge. For the typical beam currents used (<10nA) space charge effects were negligible. The ray tracing results are used as a guide to setting the electrode voltages when the beamline is in operation.
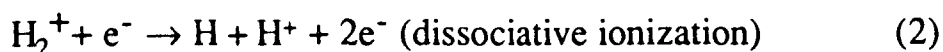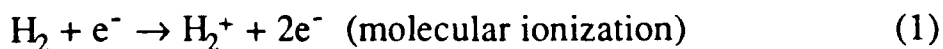
3. SOURCE AND SYSTEM OPTICS DESIGN
Ion Gun

Hydrogen gas is ionized by a hot cathode electron bombardment source in a commercially available ion gun[9]. The source is differentially pumped by a turbo molecular pump to reduce the gas load to the chamber. The source pressure is roughly 100 times greater than the chamber pressure. The cathode is a circular tungsten filament which is ohmically heated. The filament surrounds a cylindrical

grid anode. The grid is mounted to a disk with small aperture in it. Ions are extracted through the aperture by the voltage between it and the extractor. Two einzel lenses collimate the ions into the entrance aperture to the mass filter. For low energy operation, negative bias voltage V_{beam} is applied to the gun power supply such that anode potential E_0 is a few volts positive with respect to ground and the gun optics about 500 volts negative. The final beam energy is determined by the potential difference between the plasma potential in the ionization region within the grid and the grounded target. The energy of ions at the entrance to the beamline optics is determined by $E_0 - V_{beam}$.

The production of H+ ions by electron bombardment is a complicated process involving many different types of reactions. Reaction cross section data reveal that the production rate is dominated by a two stage process involving the reactions:

$$H_2 + e^- \rightarrow H_2^+ + 2e^- \quad \text{(molecular ionization)} \qquad (1)$$

$$H_2^+ + e^- \rightarrow H + H^+ + 2e^- \quad \text{(dissociative ionization)} \qquad (2)$$

The cross section for the first reaction peaks between 50 and 60 eV[10] and the second at about 3 eV.[11] To enhance the production of H^+ ions a cusped magnetic field was produced in the vicinity of the extraction aperture on the ion gun by the opposed fields of two coils. The axial component of the field is approximately 50 gauss near the center of either coil and zero between them. The cusped magnetic field confines the slow electrons to the region of the extraction cathode. Below 10^{-6} torr of chamber pressure the effect is dramatic, almost an order of magnitude increase in H^+ current with the confinement coils on. For chamber pressures above 2×10^{-6} torr the confinement field has little effect.

Mass Filter

The theory of the Wien filter is well known and has been described in detail elsewhere.[12] Our Wien filter consists of two parallel, isolated, rectangular electric field plates made of stainless steel mounted perpendicular to two magnetic pole pieces made of soft iron machined to fit inside a 3.8 cm diameter tube. The magnetic flux is confined by a soft iron yoke with pole pieces machined to fit the outside of the tube. The magnetic field is provided by two coils of about 800 turns each. The field plates are surrounded by a shield held at V_{beam}. Voltages are applied between the field plates such that the potential halfway between them is V_{beam}.

Deceleration

Ions which transit the Wien filter are collimated by a three tube einzel lens (electrodes 1,2,3) which corrects the weak focusing effect of the Wien filter. The collimated beam is then decelerated by an asymmetric 4 cylinder lens. Charge density method calculations of the potential distribution, focal properties, and aberration coefficients of both types of lens have been done in the past.[13,14]

The 4 electrode decelerating lens consists of a drift tube (electrode 3) held at the ion beam potential, two short focus tubes (electrodes 4 and 5) at adjustable potentials and a grounded cup with a small aperture (electrode 6). The aperture in this element serves as the entrance aperture for the Bessel Box. Two adjustable potentials are required so that both the image position and the angular magnification can be kept constant as the ratio of final to initial ion energy is varied.[15] This is necessary because the Bessel Box requires a fixed object distance and angular divergence at all

ion energies for optimum transmission. Calculations done for the four element lens, operating in the retarding mode, have shown that the spherical aberration coefficient increases as the ratio between the initial and final energies increases.

Energy Filter

The Bessel box type energy filter has a large angle of acceptance and high resolution.[16] The one used in our beamline consisted of a tube shaped electrode with a central stop (electrode 7) and two disk shaped endplates with apertures (electrodes 6 and 8). Both endplates are held at the same fixed potential and a retarding potential V_{bb} is applied to the tube and stop. The equipotentials for this electrode geometry are Bessel functions, hence the name. The central stop blocks energetic ions traveling along the axis and fast neutral particles created in the discharge.

Ions entering the Bessel box through the aperture in the first endplate are slowed down by axial component of the retarding field and deflected away from the axis by the radial component. Ions with kinetic energy less than the voltage between the endplates and tube are reflected by the retarding field. Ions with sufficient kinetic energy to overcome the retarding potential are accelerated towards the second endplate. If the kinetic energy of these ions is too great, the radial fields are not sufficient to focus them towards the aperture.

Only ions in a narrow range of energies will be transmitted through the second aperture. The energy range, or bandwidth, of the Bessel Box depends on the ratio of tube length to tube diameter[17] and the diameter of the stop and apertures. Naturally, the smaller the energy bandwidth, the lower the transmission.

SIMION ray tracing plots showed that the focusing properties of the Bessel box are

quite strong. Typically, the Bessel box focuses the ions a few millimeters from the exit aperture. To image the beam onto the target a few centimeters away, the ions selected by the Bessel box have to be focused by an einzel lens of relatively short focal length and low chromatic and spherical aberration coefficients. The final lens (electrodes 6, 7, and 8) is a modification of one designed by Orloff and Swanson[18].

Collector

The collector is surrounded by a grounded shield fixed to the exit aperture mount. The collector extends to within 2 mm of the target to insure the maximum collecting angle with the target plane set normal to the beam axis. The incident protons pass through an aperture in the bottom of the cup. This aperture is smaller than the exit aperture in electrode 10 so that no protons strike the collector. A shielded coaxial cable carries the secondary signal from the collector to a Keithly 614 electrometer.

Secondary electrons, produced by Auger neutralization of the protons, also strike the collector. A magnetic field of about 25 gauss, produced by a pair of Helmholtz coils, is sufficient to deflect these electrons without affecting the H^- ions. The diameter of the collector (1.9cm) was chosen to be larger than the Larmor radius for 10 eV electrons in a 25 gauss field (about 0.7 cm). The beamline itself is magnetically shielded by a shroud of μ-metal to prevent the field from perturbing the incident beam in regions of the beamline where the ion velocity is low.

A molybdenum plate with a large circular aperture was mounted 1.3 mm in front of the target. This plate was used to align the beam on the center of the target. In addition, biasing the plate positive or the target negative produced an electric field between the target and the plate which extracted negative ions and electrons through

the hole in the plate. By biasing the target and plate to a sufficiently large positive voltage the incident protons could be reflected back into the collector to verify the incident current.

4. BEAMLINE PERFORMANCE

Initial measurements of the ion current from the ion gun were done by applying a 300 gauss magnetic field to the Wien filter and no voltage on the the field plates. Ions from the gun were deflected by the magnetic field onto one of the field plates. Measurements done at E_0=550V with V_{beam}= 0 and chamber pressure of 5×10^{-6} torr obtained total ion currents of $6\mu A$.

The mass composition of the beam was analyzed with the Wien filter for several chamber pressures (see figure 3). The magnetic field was 300 gauss and the electric field varied from 0 to 150 volts/cm. The beam current was measured at electrode 7. As the chamber pressure was raised the H^+ current increased while the H_2^+ current decreased. No attempt was made to optimize the H^+ production by changing the electron temperature close to the extraction aperture.

The beam was analyzed with a special Faraday cup equipped with a retarding grid energy analyzer. Beam profiles (figure 4) were taken in the Y and Z planes perpendicular to the beam with the exit aperture of the front lens 9.7 cm from the entrance to the Faraday cup. For these measurements the chamber pressure was 2.0×10^{-6} torr and E_0 ranged from 9.5 eV to 35.7 eV. The focus was optimized for each different setting of E_0 by adjusting the V_{bb} to maximize the current and final focus voltage to minimize the beam width. At the optimum setting, V_{bb} was always about 5

volts lower than E_0. This was attributed to the plasma potential in the ionization region of the source being slightly negative with respect to the grid (anode) due to high secondary electron emission at the grid[19].

At E_0=35.7 eV a 140 pA beam diameter at the target was about 3.0 mm in in the Y and Z directions. This implies a circular beam cross section and a current density of about 2 nA/cm^2. Using the exit aperture diameter of 2.3 mm and the exit aperture - target distance of 3.8 cm we calculate a beam divergence half angle of about 0.5°. The current of the focused beam decreased to 50 pA as the E_0 was reduced to 9.5 eV.

Energy distributions (figure 5) were obtained by differentiating plots of cup current versus retarding grid voltage. For all distributions, the voltage at which the peak in the distribution occurred corresponded closely to V_{bb}. All the distributions showed an energy spread of about 1.0 volt, independent of the final ion energy.

5. H$^-$ REFLECTION

Collector and target currents were measured as functions of the magnetic field for cesiated and uncesiated silicon (100) targets. The behavior of the target current was very dependent on focusing. When the beam was properly focused and V_{bb} was slightly higher than E_0, the target current was essentially independent of magnetic field.

At zero magnetic field and -2 volts target bias, the collector current was mostly due to secondary electrons. These were suppressed as the magnetic field was

increased (see Figure 6). As the magnetic field was raised above 25 gauss, the collector current leveled off.

As a test of the experimental apparatus, H^- yield data were taken for a silicon (100) target without sputter cleaning or heating to remove the oxide coating the surface. The incident proton energies E_p were 50, 20 and 15 eV. The H^- yield was just $\{I_{coll}/(I_{tar}-I_{coll})\}$, for B=30 gauss. Figure 7 shows a plot of H^- yield as a function of collector bias for E_p=50 eV. A positive collector balances the effect of the contact potential between the target and collector. The yield increased as the collector bias was made more positive until about 1 volt where it leveled off at about 1%. The target was grounded and collector biased +2 V for these yield measurements. The yield decreased to 0.27% for E_p =20 eV and was too small to be distinguished from the noise level at E_p =15 eV. The results are of the same order as yield calculations for hydrogen atoms on tungsten.[20] Van Toledo's measurements of H^- yields for protons scattered from a clean tungsten (110) surface of gave 0.3% at 25 eV and 1% at 50 eV.[21]

As expected, H^- yields were higher for the cesiated silicon target. For these measurements the collector was grounded and the target biased -2 volts. The silicon target was bombarded with 500 eV cesium ions at a flux of about 5 $\mu A/cm^2$ to sputter clean it and lower the work function Φ before each series of yield measurements. The dose of cesium ions to the target was approximately $10^{16}/cm^2$ for each set of measurements. Again, the target was not annealed after each set of measurements so the condition of the surface is not well defined. H^- yields were measured for different values of the work function Φ with E_p fixed. Work function values were

obtained by measurement of photo emission onset. The results, plotted in figure 8, were obtained for $\Phi \approx 1.50$ eV with E_p ranging from 4 to to 25 eV. The yield curve peaks at about 10 eV and tails off as the incident energy is increased. These results are not definitive and should be viewed only as test of the performance of the apparatus.

6. SUMMARY

We have produced an experimental probe for measuring the total H^- yield produced by surface ionization of 5-50 eV protons. The proton beam is normally incident, collimated, and nearly monoenergetic. Measurements of the H^- and secondary electron yields have been performed for bare and cesiated Si(100). Future experiments will be done on clean, well defined surfaces. In addition the energy distribution of the H^- ions will be measured.

ACKNOWLEDGMENTS

References

[1] A. Pargellis and M. Seidl, Phys. Rev. B **25** (7), 4356 (1982)

[2] S. T. Melnychuk and M. Seidl, J. Vac. Sci. Technol. A **9** (3), 1650 (1991)

[3] P. J. M. van Bommel, J. H. M. Bonnie, E. H. A. Grannemen, P. Massmann and H. J. Hopman, Journal of Applied Physics **58** (7), 2492 (1985)

[4] J.P. Guyacq, J. J. C. Geerlings, P. W. van Amersfoort, L. F. Tz Kwakman, E. H. A. Granneman and J. Los, Surface Science **157** 151 (1985)

[5] J. N. M. van Wunnik, J. J. C. Geerlings and J. Los, Surf. Sci. **131** 1 (1983)

[6] J. N. M. van Wunnik, J. J. C. Geerlings and J. Los, Surf. Sci. **131** 17 (1983)

[7] D.A. Dahl, J. E. Delmore, computer code, Idaho National Engineering Laboratory, 1988, EG&G Idaho Inc. Idaho Falls, Idaho 83415

[8] W. B. Hermannsfeldt, E-GUN- An Electron Optics and Gun Design Program,1988, Stanford Linear Accelerator Center, Stanford University, Stanford, California 94309

[9] Kratos MiniBeam I ion gun system, Kratos Analytical Instruments, 170 Williams Drive Ramsey, New Jersey 07446

[10] D. Rapp, P. Englander-Golden, J. Chem. Phys. **43**, 1464 (1965)

[11] B. Peart, K. T. Dolder, J. Phys. B **4**,1496 (1971); **5**,1554 (1972)

[12] H. Leibl, Scanning Electron Microscopy **2** 519 (1984)

[13] A. Adams and F. H. Read , J. Phys. E: Sci. Instrum., **5**, 150 (1972)

[14] G. Martinez and M. Sancho, J. Phys. E: Sci. Instrum. **16**, 625 (1983)

[15] G. Martinez, M. Sancho, and F. H. Read, J. Phys. E: Sci. Instrum. **16**, 631 (1983)

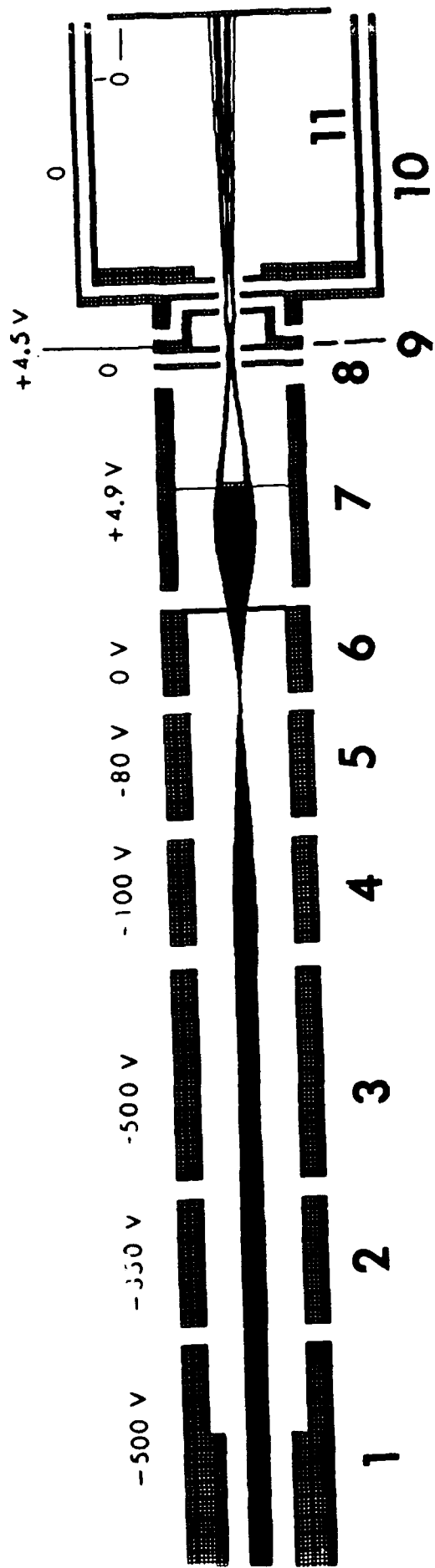[16] I. LIndau, J. C. Helmer, and J Uebbing, Rev. Sci. Inst. **44** (3), 265 (1973)
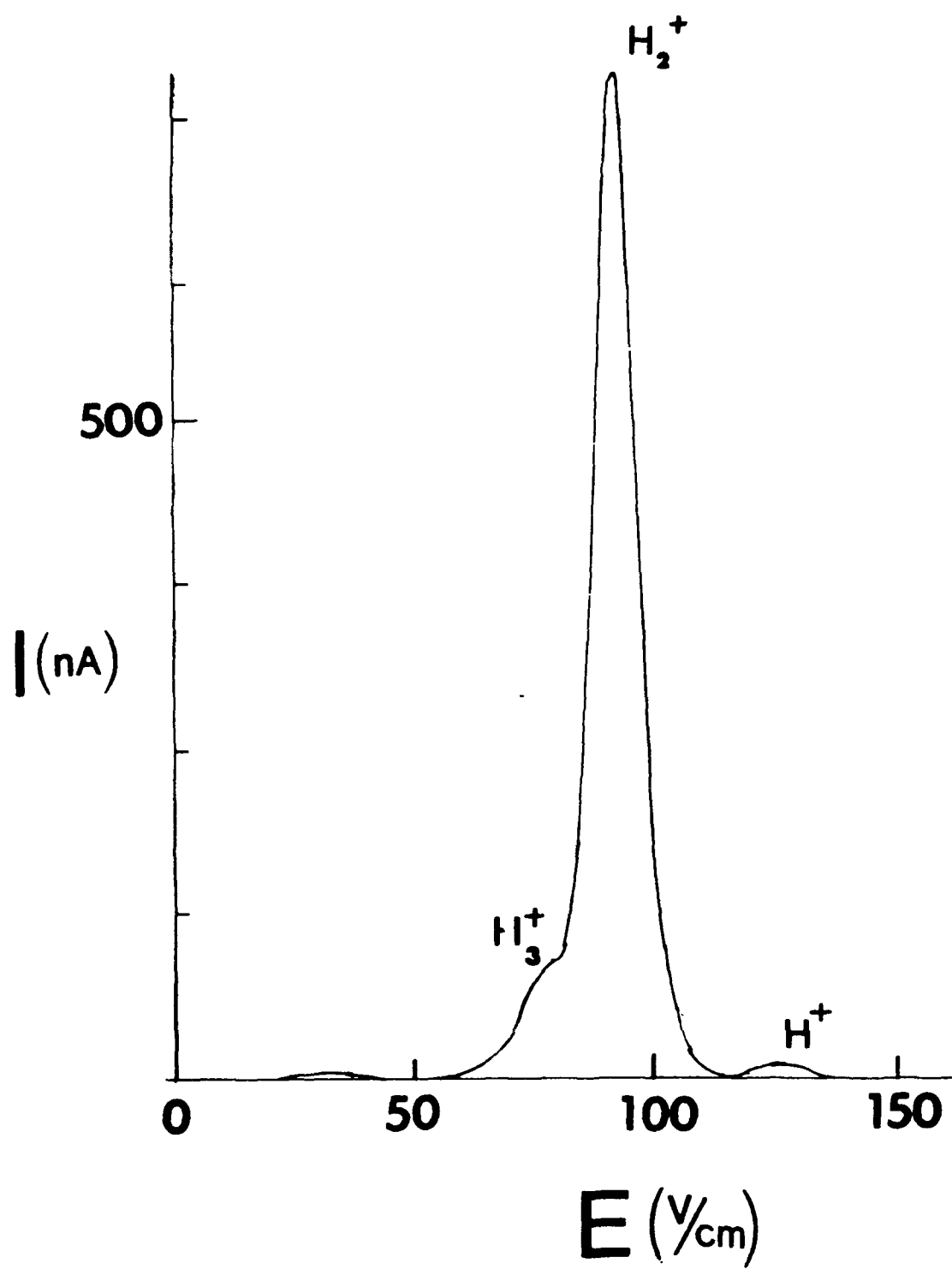
References

[17] P. C. de Jagner, H. J. Hopman, and J. B. Vrijdaghs, J. of Phys. E: Sci. Instrum. **7**, 486 (1974)

[18] J. Orloff and L. W. Swanson, J. Appl. Phys. **50** (4), April 1979

[19] B Chapman <u>Glow Discharge Processes</u> John Wiley and Sons New York, 1980 pp 114-115.

[20] H. L. Cui, J. Vac. Sci. Tech. A **9** (3), 1823 (1991)

[21] W. van Toledo, A. R. de Bree, R. van Buuren, H. de Kluiver, A. J. H. Donne, Rev. Sci. Inst., **61** (1), 622 (1990)
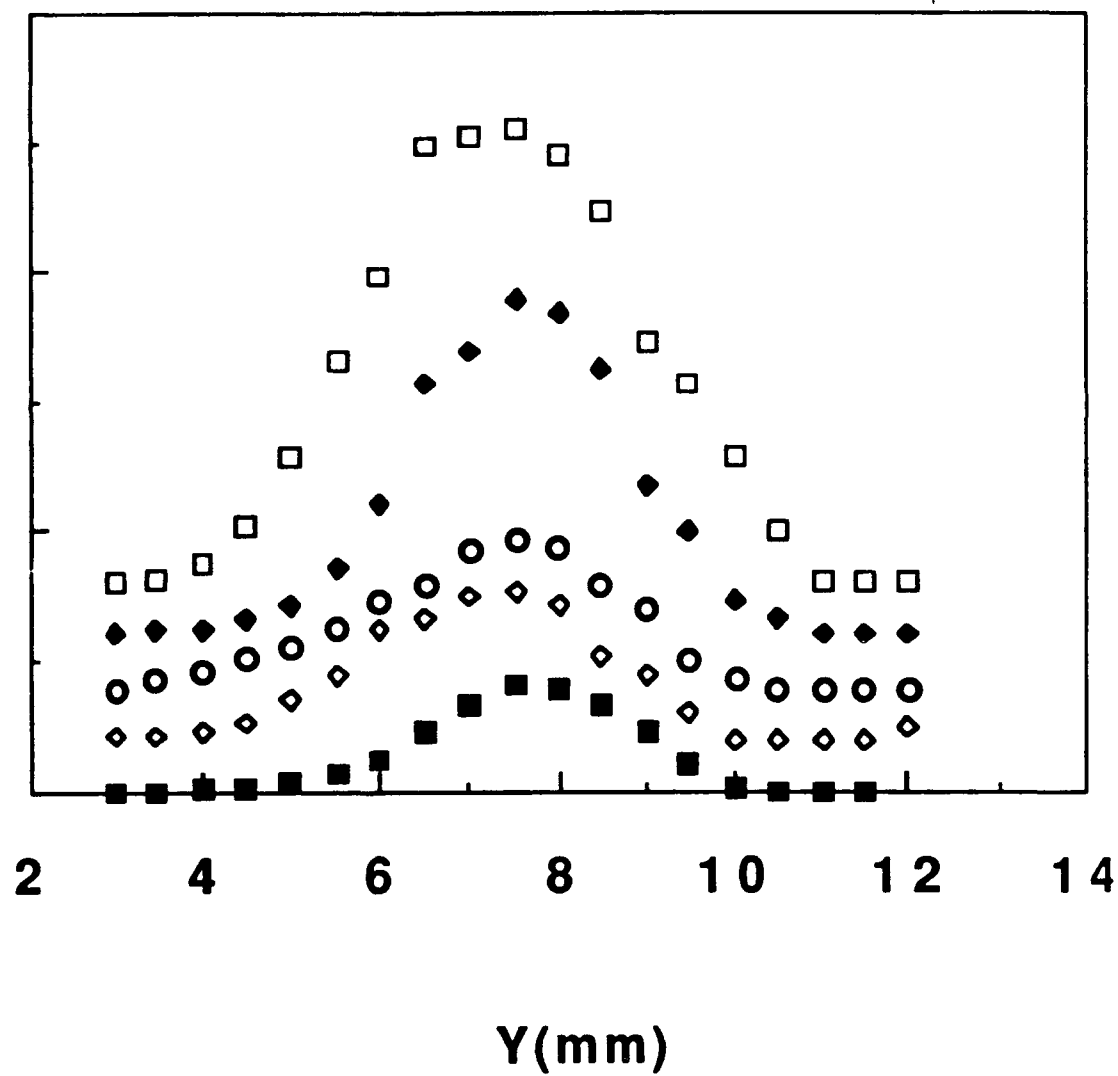
FIGURE LIST

1. Beamline scale drawing

2. SIMION trajectory plot through beamline. Initial energy is 505 eV.

3. Current vs. Electric field in Wien filter for chamber pressure of 1.0×10^{-5} torr ($B \approx 300$ gauss)

4. Beam profiles for different beam energies:

   open squares: $E_0 = 35.7$ V, $V_{bb} = 30.6$ V; filled diamonds: $E_0 = 25.1$ V, $V_{bb} = 20.1$ V; open circles : $E_0 = 18.7$ V, $V_{bb} = 13.3$ V; open diamonds: $E_0 = 13.8$ V, $V_{bb} = 8.5$ V; filled squares: $E_0 = 9.5$ V, $V_0 = 4.8$ V

5. Beam energy distributions for different beam energies:

   open squares: $E_0 = 35.7$ V, $V_{bb} = 30.6$ V; filled diamonds: $E_0 = 25.1$ V, $V_{bb} = 20.1$ V; open circles : $E_0 = 18.7$ V, $V_{bb} = 13.3$ V; open diamonds: $E_0 = 13.8$ V, $V_{bb} = 8.5$ V; filled squares: $E_0 = 9.5$ V, $V_0 = 4.8$V

6. Collector current vs. Coil current for 50 eV protons in bare Silicon (100) at different values of plate bias.

7. Yield vs. Collector bias for 50 eV protons on Silicon (100)

8. Yield vs. Incident energy for protons on Cesiated Silicon (100) for 1.5 eV work function.
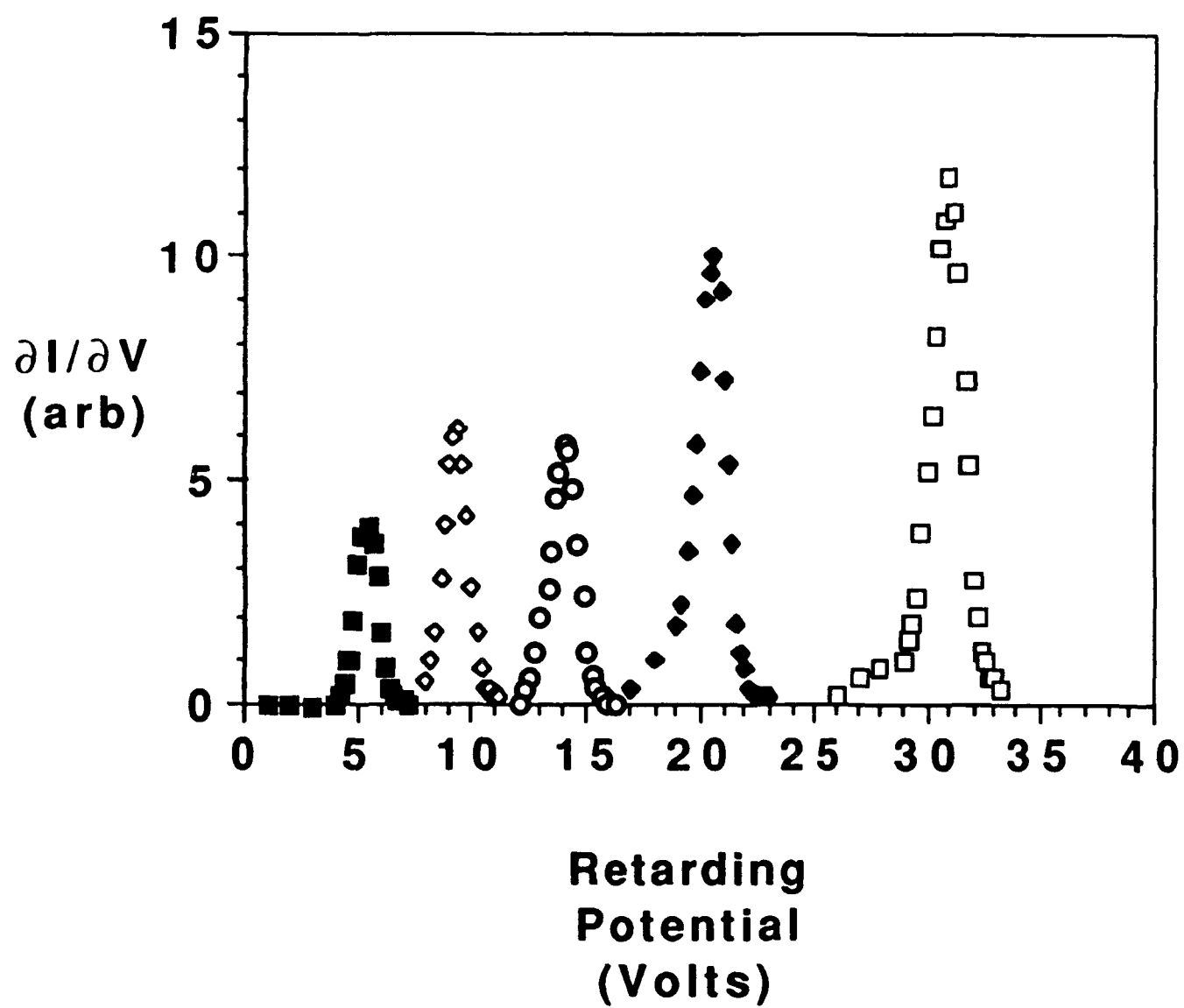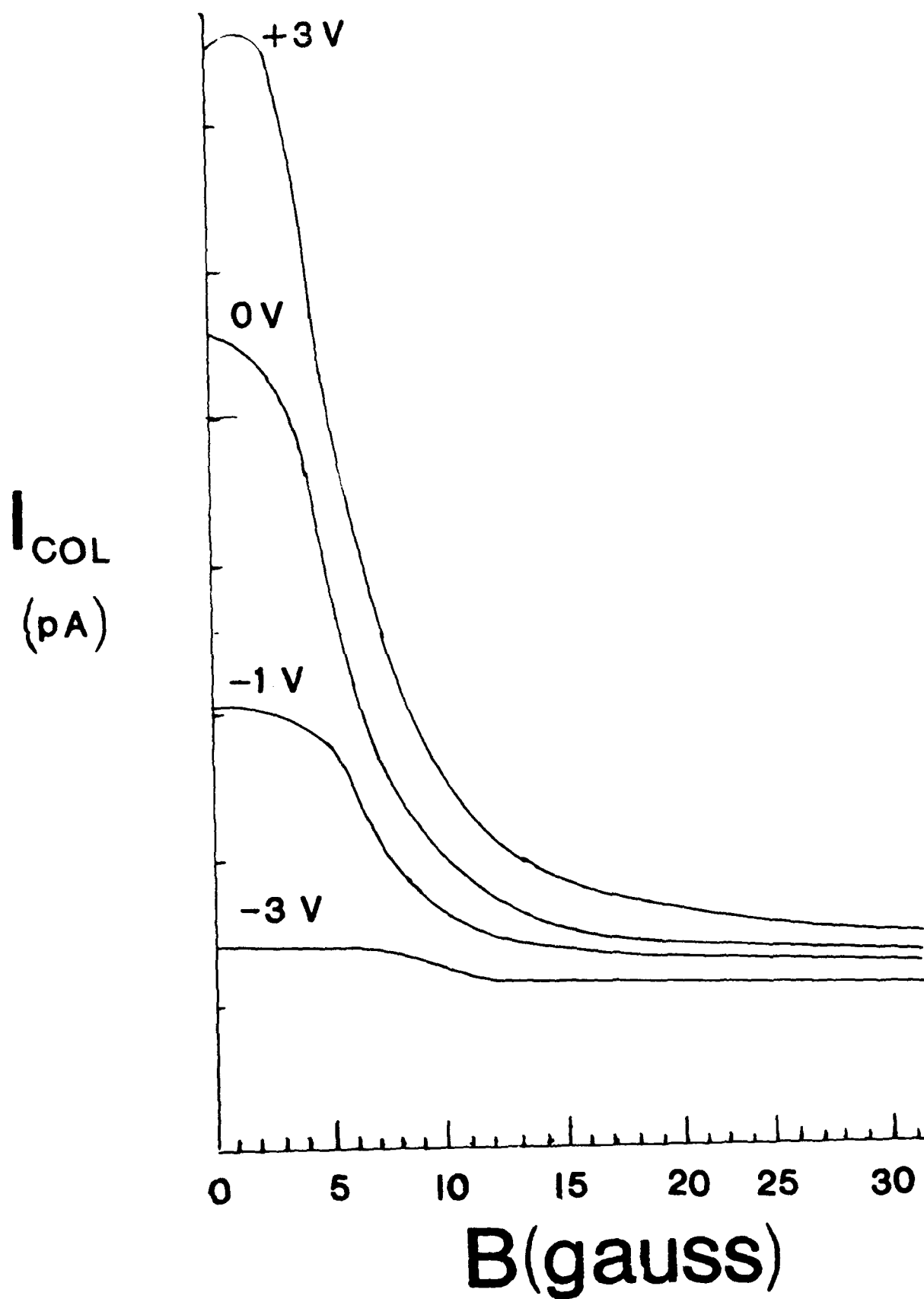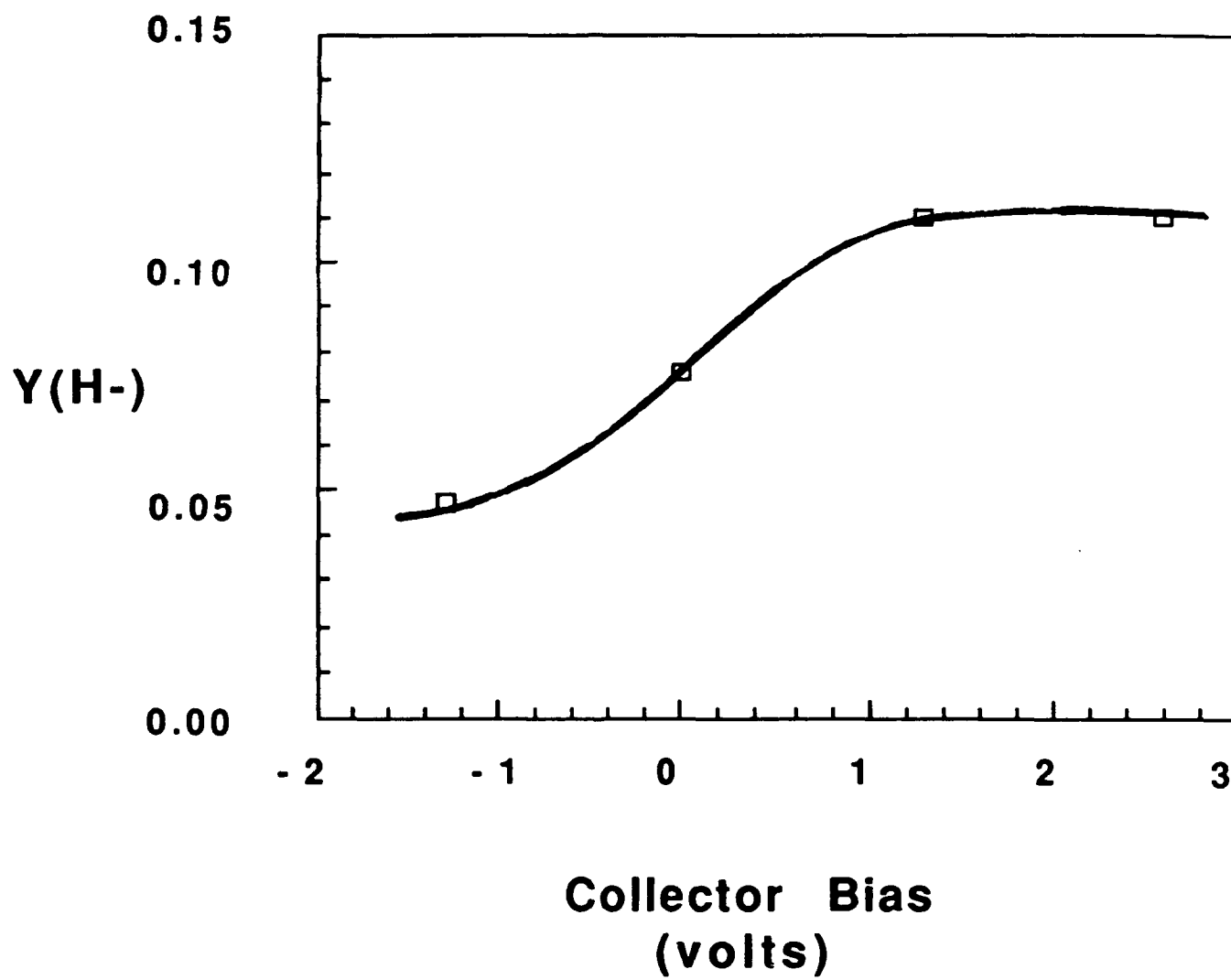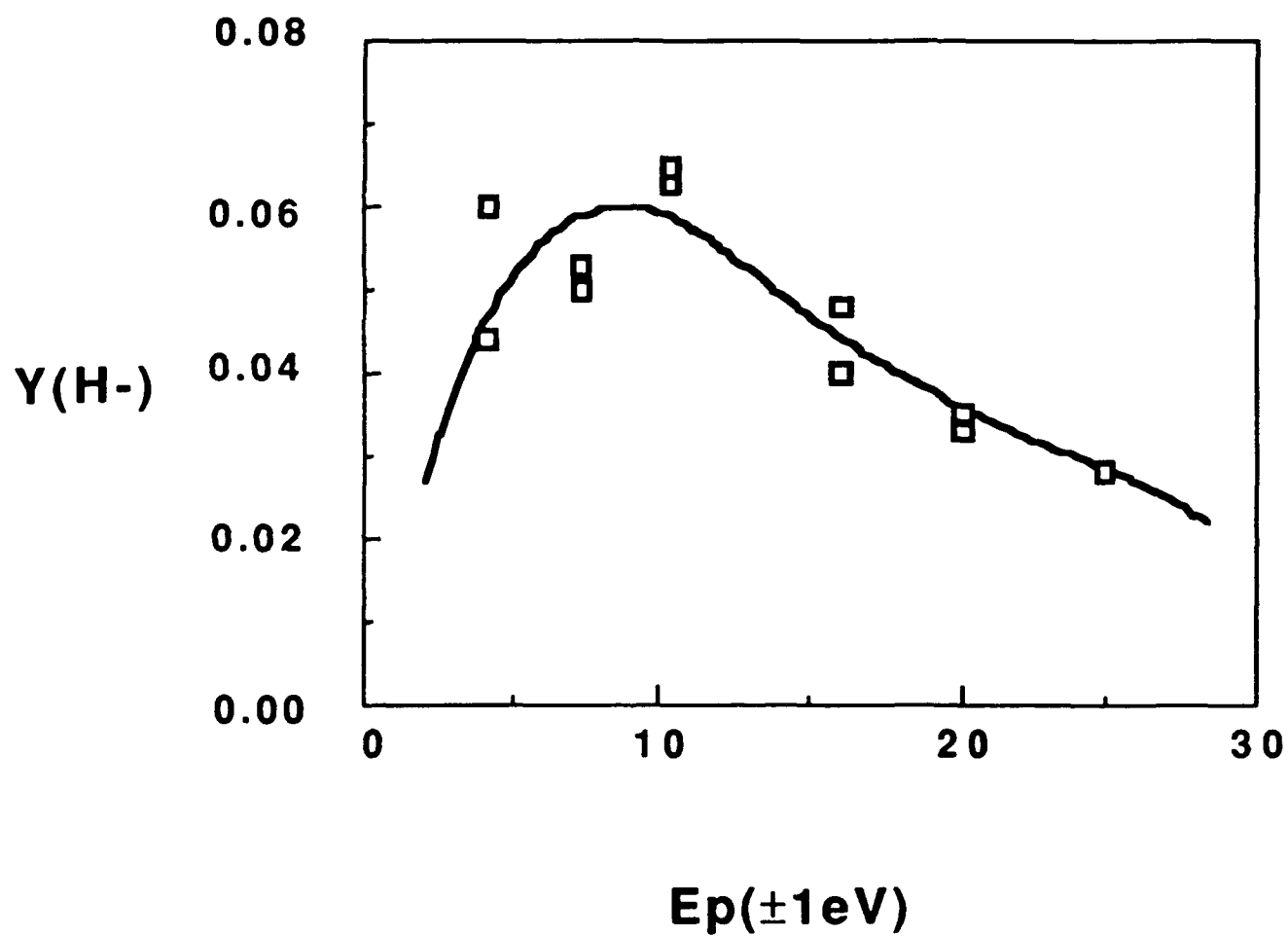
Ionizer

Extractor

Beam Forming
Optics

Scale

0

1"

Wien Filter

B→

E
⊗

Decelerating
Lens

Bessel
Box

Collector

Target

1

2

3

4

5

6

7

8

9

10

11

Plate

-500 V   -550 V   -500 V   -100 V   -80 V   0 V   +4.9 V   +4.5 V   0

1   2   3   4   5   6   7   8   9   10   11

∂I/∂V (arb)

Retarding
Potential
(Volts)

Y(H-)

Collector Bias
(volts)
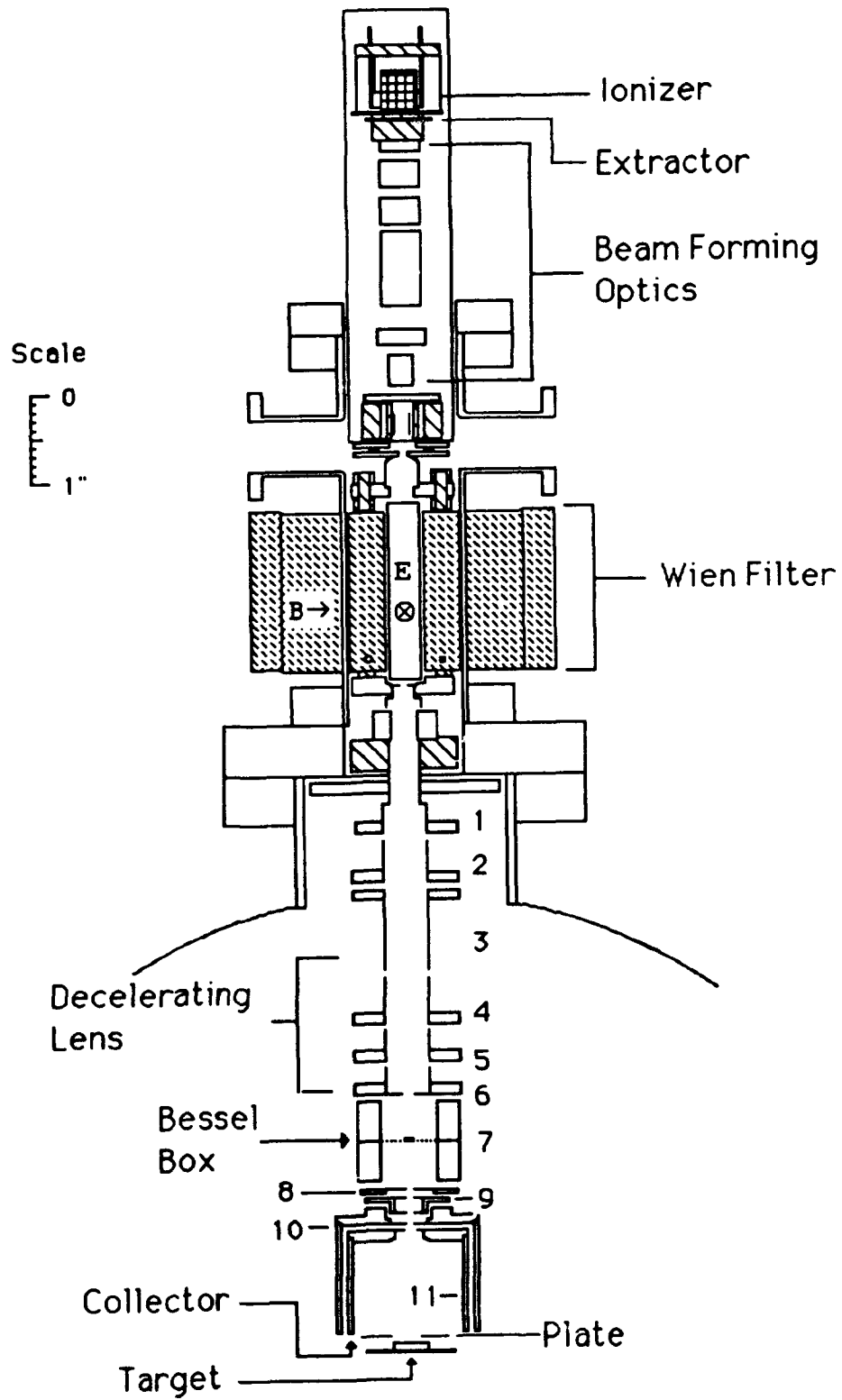
Solid State Cesium Ion Gun For Ion Beam Sputter Deposition,

S.I. Kim, Y.O. Ahn, and M. Seidl,

Dept. of Physics & Eng. Physics,

Stevens Institute of Technology, Hoboken, NJ 07030

A compact cesium ion gun, suitable for ion beam sputter deposition in high vacuum environment, has been developed. The gun uses a solid state cesium ion source described previously. This gun is compact, stable, and easy to use. It requires none of the differential pumping or associated hardware necessary in designs using cesium vapor and porous tungsten ionizers. The gun produces a cesium ion beam of 0.2 mA at 5 keV. A beam diameter of 0.2 cm is measured at a target which is 3 cm apart from the exit aperture of the accelerator electrode. The sputter deposition rate is of the order of 100 Å/min, for several metal targets such as Au, Cu, Mo, W, and Ta, measured at 4 keV primary Cs^+ ion beam energy and in a distance of 1.5 cm from the target. The life time of this gun is more than 20 coulombs of cesium which corresponds to 60 hours of operation with an extraction current of 0.1 mA.

INTRODUCTION

We have developed a cesium ion gun suitable for ion beam deposition in high vacuum environment. The gun uses a solid state cesium ion source described previously [1]. Cesium ions are chemically stored in a cylindrical pellet made of cesium-mordenite solid electrolyte. The emitting circular surface of the pellet is coated with a thin film of porous tungsten. At the operating temperature of about $1000^\circ C$, cesium-mordenite is a good conductor of Cs^+ ions. This makes it possible to control the cesium supply to the emitting surface by a voltage applied across the pellet. Cesium ion emission occurs on the surface of the porous tungsten emitter by surface ionization. This cesium ion source has been used in three types of low-current ion guns developed for surface studies [2]. In this paper we present the design and performance of a high current ion gun utilizing the solid state cesium ion source.

The ion gun, illustrated in Fig.1, consists of the cylindrical cesium ion source heated by a tungsten filament and of a Pierce-type electrode system. It produces a cesium ion beam of 0.2 mA at 5 kV extraction voltage. More than 20 coulombs of cesium ions can be extracted from the small ion source (0.6 cm in diameter and 1 cm in length) which can be reloaded. In order to prevent contamination of the ion emitter by sputtering atoms, the ion beam is electrostatically deflected onto an off-axis target.

The deposition is made on the substrate which is located 1.5 cm from the target.

This sputter ion gun has several unique features setting it apart from the more common gas source ion guns. Since it requires no gas supply, it can operate in high vacuum using a moderate speed pumping system without differential pumping and associated hardware. The compact and stable design is significant in applications with weight and size restrictions, such as for space probes. In high vacuum operation, the sputtered atoms are not losing their energy in gas collisions. They arrive on the substrate with their full energy which ranges from 10 to 100 eV [3,4]. This make it possible to deposit high quality thin films at low substrate temperature. It is known that the density, uniformity, and structure of the thin film primarily depends on the energy of the incident atoms [5,6]. High-resolution SEM studies have shown that ion beam sputtering produces films with a better fine structure than the other techniques, such as plasma diode sputtering or evaporation [7]. The sputter gun described in this paper is particularly suitable for deposition of very thin films on insulating specimens to be used in scanning electron microscopy or scanning tunneling microscopy.

DESIGN OF THE ION GUN

Following the method of Pierce [8], we have designed the gun to produce an initially convergent space-charge limited cesium ion beam of circular cross-section with a perveance $P=7 \times 10^{-10}$ $A/V^{3/2}$. The basic geometry of the beam is shown in Fig.2, where R_e is the radius of the emitting electrode, and R_x is the radius of the extracting electrode. The beam emerges from the emitter with a convergence angle θ which is reduced at the extraction electrode by lens action of the aperture. Neglecting for the moment thermal effects, the beam reaches a minimum cross-section in a distance X, from where on it diverges because of space-charge effects. It has been shown [8] that X reaches the maximum value X=1.06 Re for $R_e/R_x=2.25$. We wish to operate close to this value since the beam has to be transported as far as possible with minimum divergence. The actual chosen design value is $R_e/R_x=2.0$ which gives $X/R_e=0.96$. The convergence angle θ follows from the equation

$$P = 14.67 \times 10^{-6} \, (m_e/m_i)^{1/2} \, (1-\cos\theta)/(-\alpha)^2$$

where P is the perveance, m_e/m_i is the ratio of electron to cesium ion mass, and $(-\alpha)^2$ is 0.75. The solution is $\theta=11$ degrees. Finally, to obtain the scale of Fig.2, we choose the diameter of the emitter, $d_e=0.635$ cm.

The actual shape of the Pierce electrodes has been determined with the aid of the "E-GUN" ray-tracing program [9] which includes space-charge effects. Fig. 3a shows the computed ion trajectories which closely match the design geometry. The computed perveance is $P=5.2 \times 10^{-10}$ $A/V^{3/2}$. Fig. 3b shows how the temperature of the emitted ions affects the trajectories, as determined by the E-GUN program.

The deflecting plates are mounted on the extracting electrode, as shown in Fig.1. Fig.4 shows the ion trajectories as computed with the SIMION program [10]. From the output file of the EGUN ray tracing code, the ray information such as energy, angle, and current of each ray at a certain distance could be obtained. The ray data at a distance 80 on Fig.3b is used for the starting conditions on Fig.4.

EVALUATION OF THE GUN

The I-V characteristics of ion emission is shown in Fig.5. The emission current follows the Child-Langmuir law, indicating space-charge limited flow. The experimental perveance of 5.0×10^{-10} $A/V^{3/2}$ is closely matched with the computed value of 5.2×10^{-10} $A/V^{3/2}$. The cesium ions are supplied to the porous emitting electrode either by the thermal leakage flux or by the biasing current which is due to a voltage applied across the pellet. The details of the transport mechanism of cesium ions were described elsewhere. [11] When there is no biasing across the pellet

(dotted line with symbol o on Fig.5), the emission is supply-limited at a high extraction voltage. At this stage, the emission current can be controlled by the biasing current across the pellet. A steady ion emission current could be obtained and controlled using a constant current supply for the various biasing currents shown in Fig.5.

The beam size has been measured against a knife edge with a Faraday cup. The beam profile without deflection of the beam has not been measured since the sputtered particles from the Faraday cup quickly deteriorate the emitter surface. The cross section of the deflected beam has been measured by moving the Faraday cup in the target plane. The beam width of half maximum is found to be 0.2 cm in the parallel direction and 0.4 cm in the perpendicular direction to the emitter plane. The distortion of the beam is due to the deflection as shown on Fig.4.

The deposition rate has been measured by a crystal monitor located 1.3 cm from the target. For Au target, the deposition rate of 360 Å/min has been measured at 3.5 keV and 0.16 mA of beam current. The deposition rates for several metal targets are shown on Fig.6. The high deposition rate is due to the small target-substrate distance. Deposition area depends on the distance between target and substrate. Uniformity of the film has been measured with a profilometer. The thickness varies less than 25% over a region about 1.5 cm in diameter. Larger area deposition, up to 5 cm, could be done by sacrificing deposition

rate   A compact ion beam sputter deposition system is now under development.

REFERENCES

1. S.I. Kim and M. Seidl, J. Appl. Phys., 67(6), 1990, p.2704

2. A. Souzis, W.E. Carr, S.I. Kim, and M. Seidl, Rev. Sci. Instrm., 61, 1990, p.788

3. W. Eckstein, Nucl. Instrm. & Meth. in Phys. Res., B18, 1987, p.344

4. Z. Jurrela, Int. J. Mass Spec. & Ion Phys., 18 1975, p.101

5. C. Fountzoulas and W.B. Nowak, J. Vac. Sci. Technol., A9(4), 1991, p.2128

6. Y. Taga and Y. Gotoh, Thin Solid Films, 193/194, 1990, p.164

7. C. Beaton and B. Filshie, JEOL News, 20E, 1982, p.23

8. J.R. Pierce, Theory and Design of Electron Beams, D. Van Nostrand Company, Inc., Princeton, NJ, 1954, Chap.10

9. W. Herrmannsfeldt, R. Becker, and I. Brodie, SLAC-PUB-5217, 1990

10. D.A. Dahl and S.E. Delmore, Simion Version 4.0, Idaho Natl. Eng. Lab., EG&G Idaho INC.

11. S.I. Kim and M. Seidl, J. Vac. Sci. & Tech., A7, 1989, p.720

FIGURE CAPTIONS

Fig.1.   Schematic diagram of the solid state cesium ion gun for

         sputter deposition.

Fig.2.   Schematic diagram of the emitter electrode design

Fig.3.   Computer calculation of ion trajectories (EGUN code)

         (a) with no thermal effect,

         (b) with thermal effect (Temp. of the beam = $1100^\circ C$)

Fig.4.   Computer calculation of the beam deflection (SIMION code)

         (for 3 keV beam energy and 1.5 kV deflection voltage)

Fig.5.   Cesium ion emission current vs. extraction voltage

Fig.6.   Deposition rate measured at the substrate, located 1.3 cm
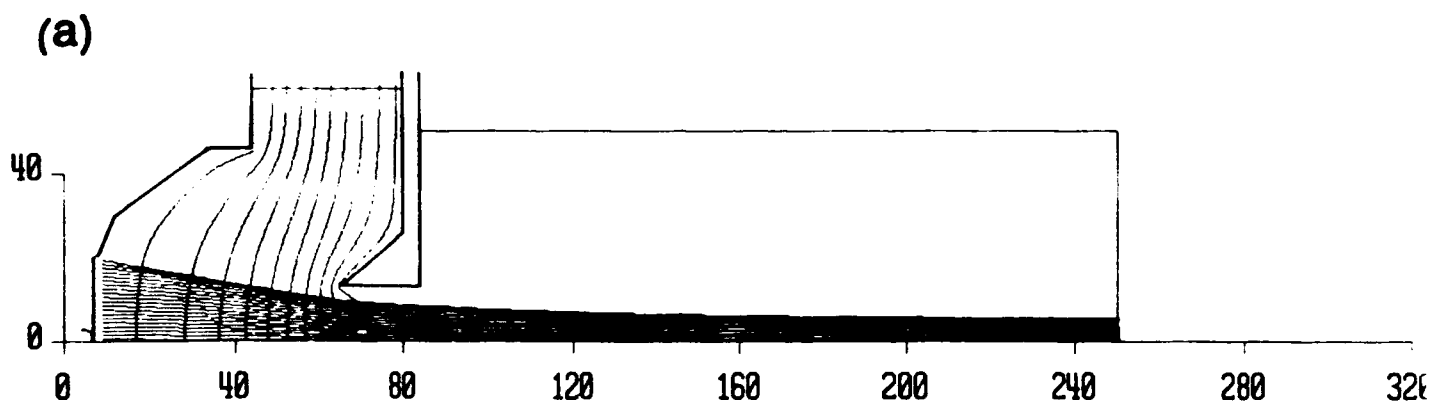
         from the target.

Fig.1.

Fig.2.

(a)

(b)

Fig.3.

Fig.4.

substrate

target

deflecting
plate

Fig.5.

Fig.6.